Kinetic study of the wave coupling dynamics with spatially smoothed laser beams

Albertine Oudin

université
PARIS-SACLAY

Kinetic study of the wave coupling dynamics with spatially smoothed laser beams

Etude cinétique de la dynamique du couplage d'onde en présence de faisceaux laser lissés spatialement

Thèse de doctorat de l'université Paris-Saclay

École doctorale n°572 : Ondes et Matière (EDOM)
Spécialité de doctorat: Physique
Graduate School : Physique. Référent : Faculté des sciences d'Orsay

Thèse préparée au Laboratoire Matière sous Conditions Extrêmes (Université Paris-Saclay, CEA), sous la direction de Didier BENISTI (Directeur de recherche CEA, LMCE) le co-encadrement de Arnaud DEBAYLE (Chercheur CEA, LMCE) et Charles RUYER (Chercheur CEA, LMCE)

Thèse soutenue à Paris-Saclay, le 20 janvier 2023, par

Albertine OUDIN

Composition du jury

Membres du jury avec voix délibérative

Catherine KRAFFT Professeure de Université Paris-Saclay, LPP	Présidente
Stefan HÜLLER Directeur de Recherche CNRS, CPHT	Rapporteur & Examinateur
Emmanuel D'HUMIERES Professeur de l'Université de Bordeaux, CELIA	Rapporteur & Examinateur
Pierre MICHEL Chef de groupe, Lawrence Livermore National Laboratory	Examinateur
Vladimir TIKHONCHUK Professeur émérite de l'Université de Bordeaux, CELIA	Examinateur

THESE DE DOCTORAT
NNT : 2023UPASP009

université PARIS-SACLAY

ÉCOLE DOCTORALE
Ondes et matière
(EDOM)

Title: Kinetic study of the wave coupling dynamics with spatially smoothed laser beams

Keywords: Laser-plasma interaction, CBET, optical smoothing, inertial confinement fusion

Abstract:

Inertial confinement fusion experiments on large laser facilities such as the LMJ in Bordeaux or the NIF in the United States, involve the propagation of lasers through large plasmas (several millimeters). A large number of instabilities called wave coupling are likely to appear, and scatter the light in a different direction from the incident electromagnetic wave. In particular, Raman and Brillouin backscattering, as well as energy exchange between laser beams result from these wave couplings. Techniques called optical smoothing are used in large facilities to try to reduce these phenomena. The beams, once smoothed, are composed of many micrometric hot spots called speckles. During these experiments, the beams, focused around a target, are going to cross each other. The coupling of two coherent electromagnetic waves in a non-linear medium (the plasma), can induce an energy exchange between the two beams. The crossing of the lasers creates an interference grating, where the ponderomotive force expels the electrons. The ions follow the electrons due to the electrostatic spring force, generating a density modulation, or acoustic wave, which diffracts the electromagnetic waves from one beam to the other. This exchange, called Cross-beam Energy Transfer (CBET) takes place if the lasers have slightly different frequencies, or if the latter are equal but the plasma is moving in the direction of the acoustic wave. We have shown that, although these two situations are often considered equivalent in hydrodynamic models, they are in fact different. This is due to the fact that the exchange is commonly calculated by considering the laser beams as plane waves, i.e. neglecting the laser smoothing. In order to demonstrate this non-equivalence, we first studied an academic situation, considering the crossing of two laser beams each constituted of 4 Gaussian speckles. Different simulations have been performed with a particle-in-cell kinetic code, solving the Vlasov and Maxwell equations. The simulations showed that when the interaction is induced by a moving plasma, plane wave models are able to predict the exchange between the Gaussian beams. By contrast, when the exchange is induced by different laser frequencies, plane wave models overestimate the energy transfer. Moreover, we were able to distinguish two different configurations for the case where the laser frequencies are different. In the first case, the acoustic waves from different speckle crossings are in phase, and a constructive interference results from their interaction. In the other case, the waves are out of phase resulting in a destructive interference. It has been shown that although the exchange is greater in the in-phase case, the exchange remains lower than in the plasma flow case. The phase shift is therefore not the only source of difference between the two situations in which CBET appears. These results were obtained by considering a weakly Landau-damped plasma, i.e. a situation where the acoustic wave propagates and may encounter several speckle crossings before being damped. In a second step, a more realistic modeling of the smoothed beams has been adopted. For this purpose, the fields of a smoothed laser beam have been computed in an exact way, allowing to perform more accurate simulations and to build a model taking into account the real structure of the speckles. The previous results concerning the non-equivalence between the plasma flow and wavelength shift cases have been confirmed, even in the case of a strongly Landau-damped plasma. We were then able to show that the resonance conditions allowing the energy transfer to take place are also affected by the laser smoothing. In particular, the resonance width is broadened by the spatial smoothing.

Titre: Etude cinétique de la dynamique du couplage d'onde en présence de faisceaux laser lissés spatialement

Mots clés: Interaction laser-plasma, échange d'énergie par croisement de faisceaux, lissage optique, fusion par confinement inertiel

Résumé:

Les expériences de fusion par confinement inertiel sur les grandes installations laser, telles que le LMJ à Bordeaux ou le NIF aux États-Unis, nécessitent la propagation des lasers à travers des plasmas de grandes tailles (plusieurs millimètres). Un grand nombre d'instabilités dites de couplages d'ondes peuvent apparaître, et diffusent la lumière dans une direction différente de l'onde électromagnétique incidente. En particulier, les diffusions arrières Raman et Brillouin, ainsi que l'échange d'énergie entre faisceaux laser en résultent. Des techniques dites de lissage optique sont utilisées pour tenter de réduire ces phénomènes. Les faisceaux, une fois lissés, sont constitués de nombreux points chauds micrométriques nommés speckles. Lors de ces expériences, les faisceaux, focalisés autour d'une cible, vont être amenés à se croiser. Le couplage de deux ondes électromagnétiques cohérentes dans un milieu non-linéaire (le plasma), peut induire un échange d'énergie entre les faisceaux. Le croisement des lasers crée un réseau d'interférences, où la force pondéromotrice expulse les électrons. Les ions suivent les électrons à cause de la force de rappel électrostatique. Cela crée une modulation de densité, ou onde acoustique, qui diffracte les ondes électromagnétiques d'un faisceau vers l'autre. Cet échange, nommé Crossbeam Energy Transfer (CBET) a lieu si les lasers ont des fréquences différentes, ou si ces dernières sont égales mais que le plasma est en mouvement dans la direction de l'onde acoustique. Nous avons montré que, bien que ces deux situations soient souvent considérées comme équivalentes dans les modèles hydrodynamiques, elles sont en réalité différentes. Ceci est dû au fait que l'échange est communément calculé en considérant les faisceaux laser comme des ondes planes, c'est-à-dire en négligeant le lissage laser. Afin de démontrer cette non-équivalence, nous avons, dans un premier temps, étudié une situation académique, en considérant le croisement de deux faisceaux lasers constitués chacun de 4 speckles Gaussiens. Différentes simulations ont été effectuées grâce à un code cinétique "particle-in-cell", résolvant les équations de Vlasov et de Maxwell. Les simulations ont montré que lorsque l'interaction est induite par un plasma en mouvement, les modèles du type onde plane sont en mesure de prédire l'échange entre les faisceaux Gaussiens. Au contraire, lorsque l'échange est induit par des fréquences laser différentes, ces modèles surestiment le transfert d'énergie. Nous avons aussi mis en évidence deux configurations distinctes dans le cas où les fréquences laser sont différentes. Dans la première situation, les ondes acoustiques issues de différents croisements de speckles sont en phase, et une interférence constructive résulte de leur interaction. Dans l'autre situation, les ondes sont déphasées ce qui donne une interférence destructive. Nous avons montré que, bien que l'échange soit plus important dans la situation en phase, il demeure inférieur au cas flot de plasma. Le déphasage n'est donc pas la seule cause de la différence entre une interaction avec ou sans flot. Nos résultats ont été obtenus en considérant un plasma faiblement amorti, où l'onde acoustique se propage et peut rencontrer plusieurs croisements de speckles avant que son amplitude n'ait significativement décru. Dans un second temps, nous avons considéré une situation plus proche de celle d'un croisement de faisceaux lissés. Nous avons calculé exactement le champ d'un faisceau laser lissé, ce qui a permis d'effectuer des simulations plus précises et de construire un modèle tenant compte de la structure réelle des speckles. Les résultats précédents ont été confirmés, même dans le cas d'un plasma fortement amorti. Nous avons également pu montrer que les conditions de résonance permettant au transfert d'énergie d'avoir lieu sont elles aussi affectées par le lissage laser. En particulier, le lissage spatial augmente la largeur de résonance.

Acknowledgements

Je tiens dans un premier temps à remercier les membres de mon jury. Merci à Emmanuel d'Humières et Stefan Hüller pour leur implication dans leur travail de rapporteur. En particulier, merci à Stefan pour ses nombreux commentaires m'ayant permis de proposer une version nettement améliorée du manuscrit. Merci également à Pierre Michel et Vladimir Tikhonchuk, pour leurs remarques et questions constructives. Enfin, j'adresse un remerciement particulier à Catherine Krafft. Pour avoir présidé le jury, mais surtout pour la qualité de son cours de dynamique non linéaire en Master 1, m'ayant convaincu de poursuivre dans le Master 2 plasma, ainsi que pour ses encouragements et sa bienveillance au long de ces années. De manière générale, j'ai été honorée de soutenir devant un jury constitué de tant de rockstars internationales de la physique des plasmas.

Je remercie ensuite Didier, pour avoir accepté de diriger cette thèse. Bien que nos interactions n'aient pas été si fréquentes, elles furent toutes déterminantes. Comme je l'ai dit lors de ma soutenance, lorsque nous venions te voir avec un problème, nous repartions parfois avec une solution, mais le plus souvent avec de nouveaux problèmes. Merci d'avoir soulevé tant de questions pertinentes, de n'avoir rien laissé passer, ce qui m'a permis de gagner la rigueur dont j'étais totalement dépourvue.

Merci à Arnaud et Charles, pour m'avoir encadrée depuis mon stage de M2, donc quasiment quatre ans, et pour la confiance que vous m'avez accordée. Vous m'avez toujours poussée à faire mieux sans jamais me mettre la pression. Merci en particulier à Arnaud pour ta patience légendaire, je ne compte pas les fois où j'ai perdu un temps non négligeable pour ne pas avoir suivi tes conseils, et où tu es resté parfaitement calme. Malgré ce manque de docilité, je pense avoir finalement compris un grand nombre de leçons qui me seront utiles par la suite. Je mesure parfaitement la chance que j'ai eu d'avoir été si bien encadrée par vous trois, et je vous en serai

toujours reconnaissante.

La plus importante contribution au maintien de mon humeur et de mon moral vient de mes collègues doctorants. Je pense avec déjà beaucoup de nostalgie à la faible probabilité de rencontrer de nouveau une ambiance pareille dans un environnement de travail. Pour ces remerciements, j'ai hésité à abandonner ma façon agressive de démontrer mon affection. Mais comment résister à la tentation de vous persécuter une dernière fois ?
Tout d'abord merci aux vieux, Mathieu, Marie, Grégoire, Cécile, (devrais-je inclure Ronan dedans ? Difficile de savoir lorsque la thèse dure plus longtemps que le règne d'Elisabeth II) de nous avoir si bien accueillis dans le fameux couloir. En particulier Djiss, même si tu n'es pas venu à ma soutenance et que j'ai par conséquent déjà maudis chaque parcelle de ta pathétique personne, ton soutien lors de moments difficiles de ma première année a beaucoup compté. Je finis par Éric, entre deux générations, mais intemporellement Maître du Mal.
Je tiens ensuite à remercier ma génération : Mathilde (fidèle partenaire de complainte) qui me suit depuis la L3, Olivier (heeeein ?) depuis le M1, Victor (Vicky Minaj dans le milieu) depuis le M2 et Baptiste (célèbre pour sa culture générale complètement aléatoire) depuis le stage. Ce n'est pourtant pas faute d'avoir tenté de me débarrasser d'eux... Je suis la dernière de la portée 2019 à soutenir, et ce fut un plaisir de partager ces années avec vous. Je n'oublie pas Mika, extérieur au couloir mais partenaire d'escalade et taxi de qualité.
Je remercie ensuite Bastien, enfant unique supplément orphelin, pour toutes ces conversations trépidantes, de nos débats passionnés sur des sujet profonds tels que « Becky G vs Karol G » à nos joutes philosophiques sur les lentilles. Mes gestes poétiques à chaque apparition devant ton bureau me manquent déjà.
(Et merci quand même à Louise, petit oiseau parti trop tôt, pour cette année en ta présence).
Viennent enfin les petits, qui ont transformé le couloir en garderie pour mon plus grand plaisir. Tout d'abord Coco, mon petit frère de thèse, représentation matérielle du mot beauf, pour tous ces moments d'humour teintés de subtilité. Puis Kéké, arrivé innocent, transformé en monstre en l'espace de quelques mois par nos soins. Bien que j'aie peu passé de temps dans le bureau après votre arrivée, c'était toujours un plaisir de venir semer le désordre en votre compagnie. Merci ensuite à mon bibou JG, pour m'avoir fait tant rire (malgré toi) pour avoir été mon taxi (pas le meilleur) et pour tous ces massages pendant ma rédaction. Merci à Seb, dont la susceptibilité a fortement décru en notre compagnie, pour l'organisation des cafés-science et pour avoir été un digne héritier de la tyrannie alimentaire de Mathilde. Merci à Mec d'avoir illuminé mes journées avec ses vêtements fluo, à Jojo pour toutes ces séances d'escalades dont

le nombre n'égale pas celui des blagues non comprises, à Paul pour m'avoir écouté rager sur la circulation du rond-point d'Alésia à chaque sortie du bus. La plupart des doctorants voient leur dernière année comme la pire. Grâce à vous, elle a été la meilleure pour moi. Et c'est la dernière fois que je dis quelque chose d'aussi niais.
Enfin, les très-petits. Qu'aurais-je fait sans Marin pour la reliure de tous ces exemplaires de mon manuscrit ? Comment Léa va-t-elle survivre en tant que dernière fille des doctorants ? Merci à vous deux pour la super ambiance au sous-sol. Finalement, merci à Ulrich qui m'a laissé le martyriser sans broncher. Ne t'avise pas d'aller à l'escalade sans moi.
Je remercie également les post-docs, Adrien, notre Usain Bolt à nous, pour m'avoir transmis sa science en matière de cookie, et Cousin pour son humour aussi décapant que les grillades du 13e.

Merci en général à toutes les personnes qui ont rendu agréables mes trois années au CEA. En particulier à ma mère adoptive du self, pour l'affection (et les doubles rations) qu'elle m'a donné.

Merci également à Delphine et Virginie pour leur confiance en me donnant l'opportunité d'enseigner en histoire des sciences et pour tout ce que cela m'a apporté.

Le mental, ce n'est pas gratuit, alors une pensée particulière va à mes différents profs de sport. Merci à Sandra pour ces après-midi HIIT et cross-training. Tous ces dimanches à manger le sol et ravaler mon vomi sous tes ordres m'ont rendue invincible. Dans une autre catégorie, merci à Max pour m'avoir fait découvrir le yoga (le vrai hein, pas celui d'Instagram) en troisième année, dont l'un des nombreux bienfaits fut de m'affranchir des douleurs dorsales provoquées par la rédaction.

Je ne vais pas remercier personnellement chaque personne dont l'influence positive sur ma vie dépasse très largement le cadre de la thèse. Alors un merci général à ma famille et à mes amis pour leur soutien. Je me dois tout de même de faire une exception pour mes deux meilleurs amis. Sophie, cela fait désormais la moitié de ma vie que tu es à mes côtés, merci pour ton amitié inconditionnelle depuis le début. Hugo, merci d'avoir été la première personne avec qui j'ai pu être réellement moi-même, et pour la confiance que tu m'as permis de t'accorder. Votre présence et votre réconfort ont été, et me sont toujours essentiels.

Cette fois ci, je cesse réellement les niaiseries et laisse la place aux choses sérieuses.

Contents

Nomenclature

ϵ_0 Vacuum permittivity

$\omega_{pe} = \sqrt{\frac{e^2 n_e}{\epsilon_0 m_e}}$ Plasma pulsation

$\omega_{pi} = \sqrt{\frac{Z^2 e^2 n_i}{\epsilon_0 m_i}}$ Plasma ionic pulsation

c_s Acoustic velocity

e Elementary charge

f Focal distance

$f_\#$ f number

k_B Boltzmann constant

m_e Electronic mass

m_i Ionic mass

n_e Electronic density

n_i Ion density

T_e Electronic temperature

T_i Ionic temperature

v_d Plasma drift velocity

$v_{T_e} = \sqrt{\frac{k_B T_e}{m_e}}$ Electronic thermal velocity

$v_{T_i} = \sqrt{\frac{k_B T_i}{m_i}}$ Ionic thermal velocity

ϕ Phase of an Ion Acoustic Wave

φ Phase of a Phase Plate element

$S(\boldsymbol{r}, t)$ Varying phase of a field

$\langle Q \rangle_x$ Mean value over x of the quantity Q

$\overline{Q}$ Fourier transform of the quantity Q

$\widetilde{Q}$ Envelope of the quantity Q

Q^{driven} Asymptotic value of the quantity Q

Acronyms

CBET Cross-Beam Energy Transfer

CPP Continuous Phase Plate

DT Deuterium-Tritium

EMW Electromagnetic Wave

EPW Electron Plasma Wave

FT Fourier Transform

IAW Ion Acoustic Wave

ICF Inertial Confinement Fusion

KPP Kinoform Phase Plate

LMJ Laser Méga Joule

LPI Laser Plasma Interaction

NIF National Ignition Fusion

PIC Particle In Cell

PS Polarization Smoothing

RPP Random Phase Plate

SBS Stimulated Brillouin Scattering

SC Speckle Crossing

SRS Stimulated Raman Scattering

SSD Smoothing by Spectral Dispersion

List of Figures

Chapter 1

Introduction

Contents

1.1 Context: The ubiquity of Cross-Beam Energy Transfer in Inertial Confinement Fusion

The fusion reaction between Deuterium-Tritium (DT) nuclei has the highest cross-section at low energies, with a peak around $60-70$ keV. It releases an important amount of energy by emitting a helium nucleus and a neutron by the following reaction: $D + T \longrightarrow {}^4H_e + n + 17,59\,\mathrm{MeV}$, illustrated in Fig. 1.1. In the center of mass reference frame, the neutron gets 80% of the

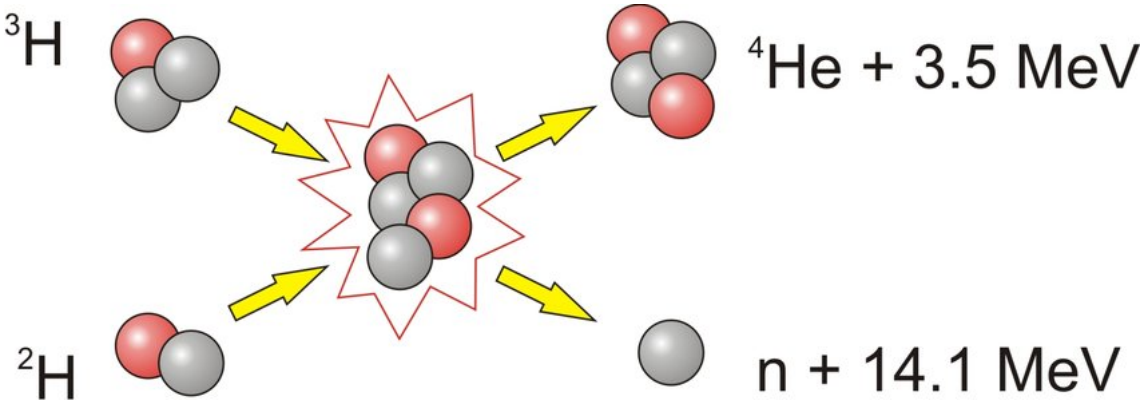

Figure 1.1: Deuterium-Tritium fusion reaction. From [60].

energy and the ${}^4H_e$ leaves the reaction with 20% because of its higher mass.

Inertial Confinement Fusion (ICF) [80, 59] aims at initiating a thermonuclear fusion wave by compressing a deuterium-tritium hollow sphere with many laser beams. A dense millimeter-size shell is filled with DT fuel, in its solid phase on the inner walls and in its gaseous phase inside as shown in Fig. 1.2. Obtaining a high compression of the shell allows to initiate a thermonuclear combustion. To this purpose, two schemes have been proposed, known as direct and indirect drive.

In the direct drive approach, beams directly irradiate the target. The illumination must be uniform in order to obtain a homogeneous and thus efficient compression of the target. Achieving a great uniformity requires both a large number of beams and a great control of the beams propagation. Figure 1.3 is a schematic representation of direct drive. In a realistic facility as National Ignition Fusion (NIF) or Laser Méga Joule (LMJ), a hundred of laser beams will be focused on the target. Here, only a few are represented by colored or dashed rectangles, to illustrate the effort of symmetry of the irradiation.

In the indirect drive approach, the shell is placed in a centimeter-size cylindrical gold cavity

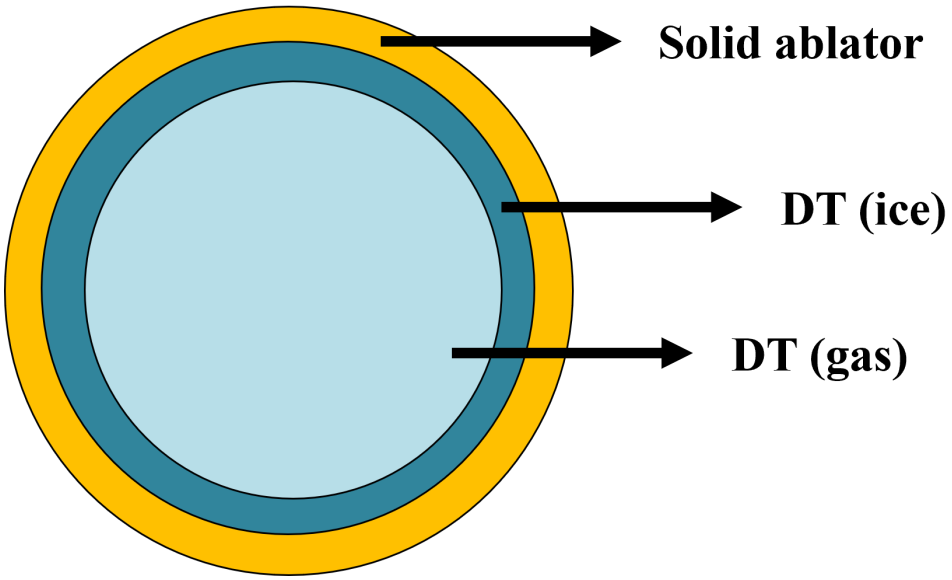

Figure 1.2: Cross section of an ICF target.

called hohlraum, filled with a gas in order to reduce the gold plasma expansion towards the target. Figure 1.4 illustrates the target geometry with some of the hundred of beams focused inside the hohlraum. The laser beams enter the cavity and irradiate the inner wall of the hohlraum. The gold plasma absorbs the UV light and homogeneously re-emits an important energy fraction through X-emissions which compress the DT shell. The homogeneous illumination is obtained at the cost of a reduced efficiency due to the laser-to-X conversion.

In both configurations, the interaction between the lasers and the plasma leads to a plethora of phenomena. Among them, Brillouin/Raman scatterings and two plasmon decay are well-known wave mixing processes, resulting in undesired energy losses and hot electrons production whose mitigation is of prime importance for achieving ignition. Cross-Beam Energy Transfer (CBET) is another class of wave coupling leading to an energy exchange between the laser pulses. This 0 order phenomenon occurs at each crossing. In a direct-drive configuration, illustrated in Fig. 1.3, an incoming beam, represented in red, can lose energy to a refracted beam, represented in blue. This particular two-beam configuration applies to all the crossings around the target leading to potentially high energy losses. In the indirect-drive scheme Fig. 1.4, the CBET between beams entering the cavity (example of Beam0 and Beam1), can lead to a power drive imbalance. Furthermore, an incident beam can also cross a reflected beam (Beam0 and Beam1'), hence leading to energy losses. This energy exchange is ubiquitous in both direct and indirect drive schemes and leads to an energy exchange from a few percent to the total laser depletion [45, 77]. The homogeneity of compression is therefore strongly

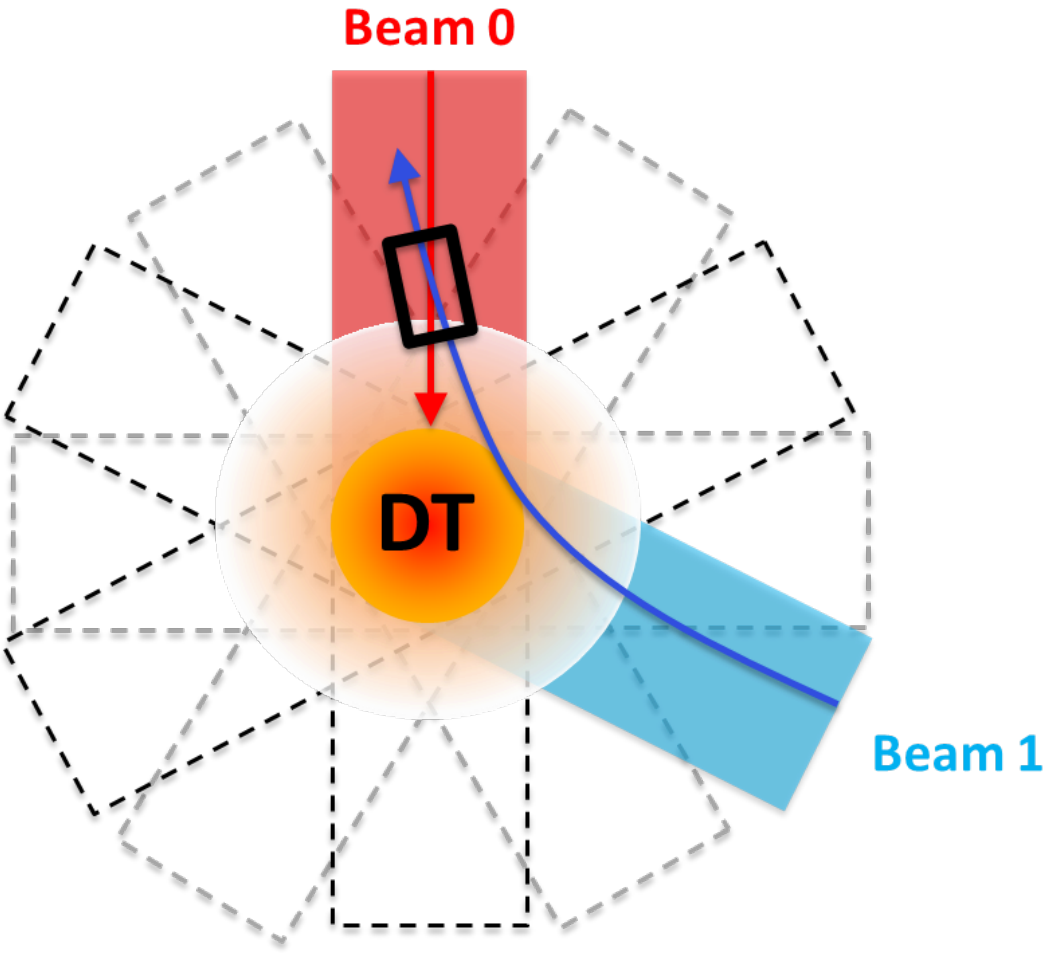

Figure 1.3: Direct Drive scheme of ICF

affected which may prevent ignition if not accounted for. Given the different gases and plasma velocities around the target, getting out of resonance to suppress CBET is very challenging. Furthermore, direct measurements of CBET are not yet known to exist in ICF experiments. The only measurable related data is the implosion symmetry [71, 47, 33]. In the indirect drive configuration, the symmetry is deduced from the x-ray self-emission measured through a diagnostic window in the hohlraum side [82]. In direct drive, the symmetry is deduced from the transmitted light through a large-aperture window on the target chamber [42].

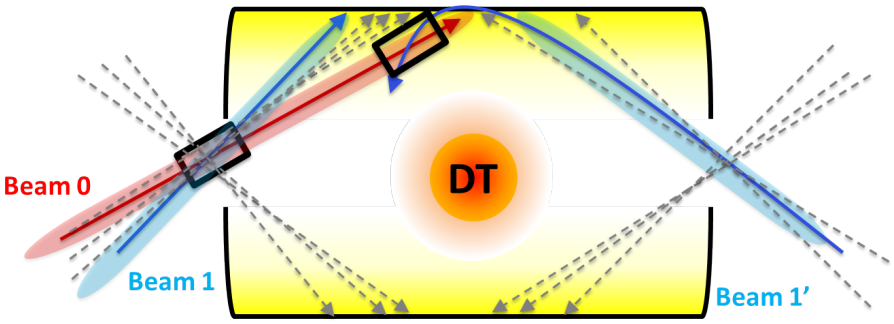

Figure 1.4: Indirect Drive scheme of ICF

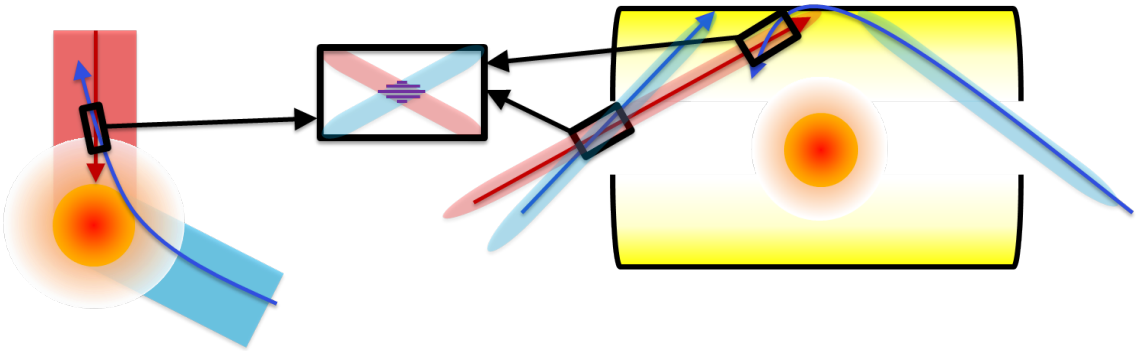

Figure 1.5: Examples of crossing zones in both direct and indirect drive schemes

1.2 Cross-Beam Energy Transfer description

The CBET phenomenon is now described. The red and blue crossing beams in Fig. 1.6 are the same as represented in Fig. 1.5 to show the link with ICF but it can actually represent any CBET configuration of two crossing beams. Moreover, the laser beam structure is actually not a plane wave as represented in the figure above. The beam is constituted of numerous hot spots called speckles. A way to exert a control on the speckles structure, locus of numerous instabilities, is described in Section 2.3. The crossing of two laser beams thus results in the crossing of numerous speckles. Consequently, the energy exchange occurs at each of these crossings. The interdependence between these exchanges is the purpose of Chapter 5. For now, only the energy exchange between two speckles is described. The green rectangle of Fig. 1.6 shows a "zoom" of the crossing zone to exhibit the speckles structure. The coherence of the laser beams induces an interference pattern in the crossing region, shown as a scheme in Fig. 1.5 and in the case of a simulation in Fig. 1.6 (lower left). The bright interference fringes of

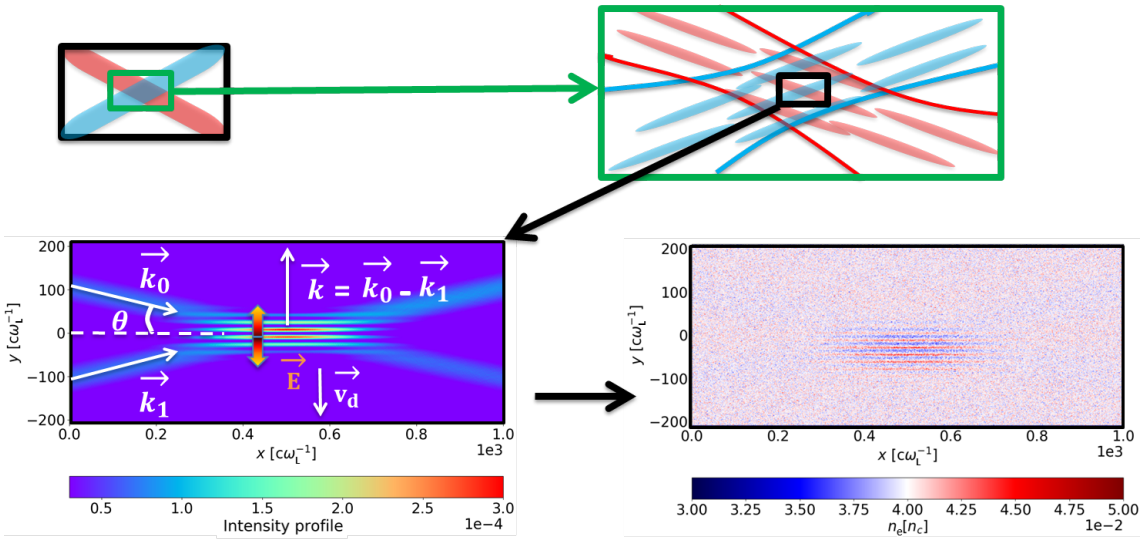

Figure 1.6: Scheme of the CBET happening between two speckles issued from two crossing beams (left) intensity (right) density. Coordinates x and y are expressed in $c\,\omega_L^{-1}$ where ω_L is the frequency of a laser beam.

the simulation (lower left in Fig. 1.6) correspond to the strong field areas. The ponderomotive force, which for electrons writes

$$\boldsymbol{F_p} = -\frac{e^2}{4m_e\omega^2}\boldsymbol{\nabla} \boldsymbol{E}^2\,, \tag{1.1}$$

expels the electrons off the strong field regions corresponding to the bright fringes. The ponderomotive force can also be written for ions, but as $m_e \ll m_i$, its effect is much smaller. Electrons are then followed by ions due to the electrostatic spring force, and a density modulation appears as represented in the simulation (lower right in Fig. 1.6). CBET occurs in two situations. When the frequencies of the beams (and therefore the speckles) are slightly different, the interference pattern moves at the velocity $(\omega_0 - \omega_1)/|\mathbf{k}_0 - \mathbf{k}_1|$ in the stationary plasma reference frame, where $k_{0,1}$ is the wave vector of the beam 0, 1 and $\omega_{0,1}$ the frequency of the beam 0,1. The other situation is when the plasma drifts at the velocity v_d. When the resonance condition,

$$\omega_0 - \omega_1 - (\mathbf{k}_0 - \mathbf{k}_1)\cdot \mathbf{v}_d = |\mathbf{k}_0 - \mathbf{k}_1| c_s\,, \tag{1.2}$$

is reached, an Ion Acoustic Wave (IAW) is formed most effectively, diffracting one beam on

the other. The exchange is carried from high to low frequencies in the plasma reference frame. In the wavelength shift case, the interference grating is moving but the crossing envelope remains motionless in the stationary plasma referential. In the plasma flow case, both the crossing envelope and the interference grating are moving at v_d in the drifting plasma referential. Investigating the intrinsic difference between these two cases is discussed in Chapter 6.

1.3 Cross-Beam Energy Transfer applications

Although uncontrolled CBET can be an obstacle to ignition achievement, it can have very positive effects in ICF when the wavelength shift is tunable. It can further be used as a tool with applications to optical devices.

1.3.1 Relation to Inertial Confinement Fusion

In both ICF schemes, the laser reaching the target / gas-filled hohlraum creates a plasma. The latter inexorably expands, with sub to supersonic plasma flows. The CBET occurring when the drift velocity matches the sound speed, $v_d = c_s$, therefore generates an inhomogeneous compression. While it is not possible to avoid the plasma flow, the laser wavelength can be shifted so as to get away from the resonance, that is to say, $\omega_0 - \omega_1 - (\mathbf{k}_0 - \mathbf{k}_1)\cdot\mathbf{v}_d \neq |\mathbf{k}_0 - \mathbf{k}_1| c_s$. Thus, it is possible to diminish or suppress the CBET by applying a wavelength shift. A wavelength separation option of several $\mathring{A}$ has been implemented on the NIF between the inner and the outer cones (called "two-color") [71] that respectively reach the equator and the pole. Insufficient to suppress the CBET everywhere, this option is used to balance the available energy between the inner and outer cones. The wavelength shift between the beams has been increased until observing a symmetric compression as shown in Fig. 1.7.

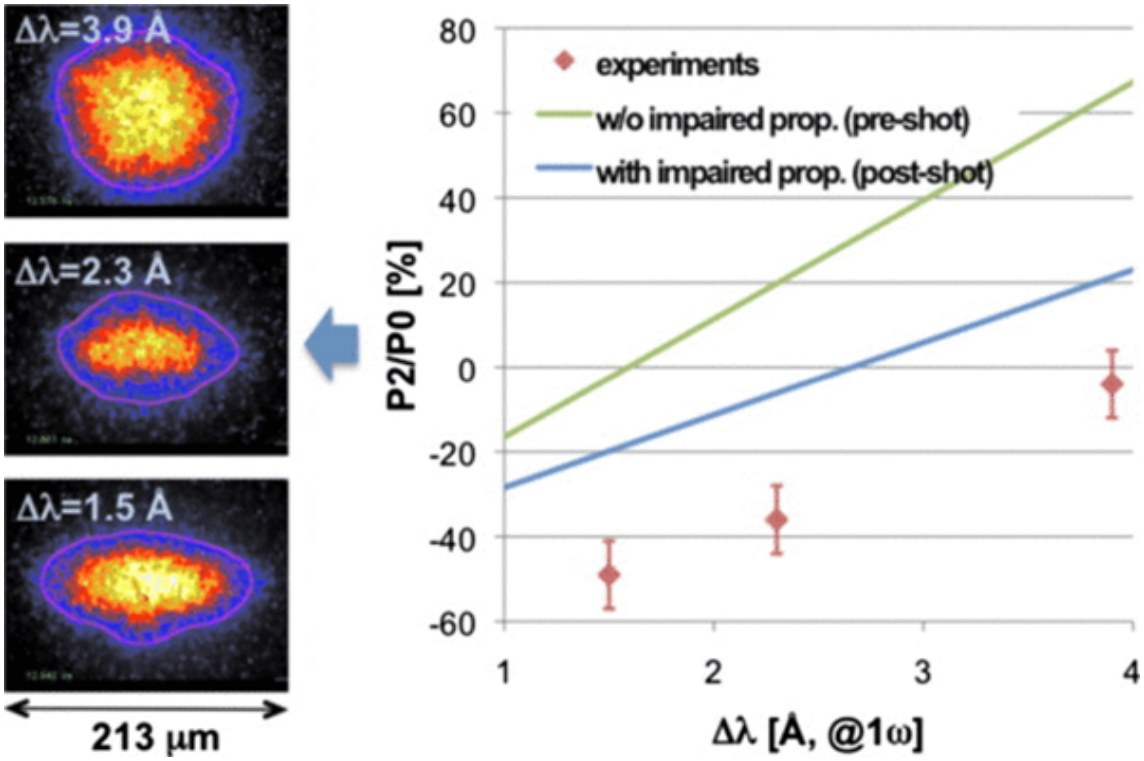

Figure 1.7: From [71] (Left) Image of the capsule for three wavelength separations between the inner and outer beams: 1.5, 2.3, and 3.9 $\mathring{A}$ (Right): Pole-waist asymmetry for the corresponding three shots as measured in the experiments (diamonds), and as calculated in pre-shot (upper line) and post-shot (lower line) simulations.

The recent achievement of a burning plasma state at NIF [120] has been made by using wavelength detuning. Previous simulations and experiments were made to calibrate the $\Delta\lambda$, and showed a symmetrical implosion when a significant fraction of the outer beam power was transferred to the inner cones [48].
Even though most CBET studies are related to ICF, it is also interesting to point out the other applications.

1.3.2 Relation to optics

In any application that requires a high laser power, the energy exchange between two laser beams can be used to increase the maximum power. Indeed, if the source is not powerfull enough, it is possible to cross beams in a way that satisfies the resonance condition to increase the maximum power of one of the beam. Numerous studies [53, 57, 92] focused on the so-called Brillouin amplification of laser pulses to develop high-intensity laser beams. This amplification

is also possible *via* Raman scattering, by a similar process.

Moreover, solid optics currently used in many laser experiments suffer from a small damage threshold. Laser-induced damage has been an issue since the beginning of laser applications, and has become an important research subject. The high fluence exposure ($> 1\,\mathrm{J/cm^2}$) may trigger a plethora of damages such as craters, digs, bulk bubbles, bulk filamentation, melting, or change in surface coloration [4]. Some solutions exist to increase the damage threshold of solid optics as for example the silica film [109] that can increase the maximum fluence on mirrors to $\simeq 70\,\mathrm{J/cm^2}$. However, fundamental limits such as ionization of the material will always prevent the damage threshold to be raised significantly beyond these numbers.

To avoid this limit, plasma photonics has been identified as a promising candidate to replace solid-state optical elements. Indeed, plasma photonics allows to shape the refractive index sustained by the free electrons. Recent studies at Lawrence Livermore National Laboratory have given encouraging results. Two fundamental types of optics have been proposed: i) ponderomotive structures, where the ponderomotive force of overlapping lasers imprints a refractive index modulation in the pre-formed plasma; and ii) localized ionization structures, where beams overlap in gas and ionize only the regions of constructive interference (i.e., the "bright" fringes) while the dark fringes remain in a state of neutral gas. For example, a new concept of plasma transmission grating [22] may divide by more than 500 times the size of the final chirped pulse amplification optics, and a plasma wave plate can change a laser's polarization state [68, 112].

The framework of the manuscript being set, we will now introduce in the following chapter the basic notions required for a smoother reading of the thesis work.

Chapter 2

Background

Contents

The term "plasma" was introduced by Irving Langmuir in 1928 [54]. If it can be defined in first approximation as an ionized gas, its properties are fundamentally different. In particular, interactions in gases are mainly binary (three-body interactions being singular), in contrast, they are collective in a plasma. There, collisional effects are essentially governed by small impact factor (or small deflection angle) collisions between the particles in a Debye sphere. Ideally described by classical molecular dynamics, such a large particle system can be approximated by the electron-ion Vlasov-Landau equations coupled with the Maxwell equations. The Particle In Cell (PIC) code is a Monte-Carlo method to solve this system and commonly used to describe all the laser/plasma instabilities. In a first section, the kinetic description of a plasma and the link with PIC codes is shown. Then, some laser-plasma common phenomena and instabilities are presented. In a third section, the smoothing techniques, useful to control the aforementioned instabilities are described. Finally, a state of the art is presented, from the first wave-mixing experiment to the current research.

2.1 Plasma descriptions

A full description of the kinetic hierarchy is out of the scope of the present thesis and can be found in Refs [46, 78]. We will briefly present the kinetic plasma description and the relation with the particle-in-cell codes as used in this study.

2.1.1 Vlasov-Landau equation

When, in a plasma, the collisional effects are negligible, particles may interact only collectively. Such system may be described by the Vlasov equation, also called collisionless Boltzmann equation:

$$\partial_t f_\alpha(\boldsymbol{r},\boldsymbol{v},t) + \boldsymbol{v}\cdot\boldsymbol{\nabla}_{\boldsymbol{r}} f_\alpha + \frac{q_\alpha}{m_\alpha}\big(\boldsymbol{E}+\boldsymbol{v}\wedge\boldsymbol{B}\big)\cdot\boldsymbol{\nabla}_{\boldsymbol{v}} f_\alpha = 0\,. \tag{2.1}$$

Here, f_α is the α-species continuous distribution that depends on position $\boldsymbol{r}$, velocity $\boldsymbol{v}$ and time t. Vlasov equation allows to study the collective motions of a plasma, i.e. the action on each charged particle of the average electric and magnetic fields ($\boldsymbol{E}$ and $\boldsymbol{B}$) created by the others, neglecting the inter-particle correlations. This equation, non-linear due to the term $\boldsymbol{\nabla}_{\boldsymbol{v}} f_\alpha\big(\boldsymbol{E}+\boldsymbol{v}\wedge\boldsymbol{B}\big)$, describes the particle density conservation in phase space.

A correction due to the collisions has been introduced by Landau, and writes:

$$\partial_t f_\alpha(\boldsymbol{r},\boldsymbol{v},t) + \boldsymbol{v}\cdot\boldsymbol{\nabla}_{\boldsymbol{r}} f_\alpha + \frac{q_\alpha}{m_\alpha}\big(\boldsymbol{E}+\boldsymbol{v}\wedge\boldsymbol{B}\big)\cdot\boldsymbol{\nabla}_{\boldsymbol{v}} f_\alpha = C[f_\alpha, f_{\alpha'}]\,, \tag{2.2}$$

where $C[f_\alpha, f_{\alpha'}]$ is a complicated integral operator [46]. This integral describes small-angle scattering. Indeed, large-angle deflections are not due to binary scattering but rather by a succession of these small-angle scattering. These collisions are calculated inside the Debye sphere, the Coulomb potential being exponentially decreasing beyond.

Plasma modeling with a Particle-In-Cell code

Contrary to what PIC suggests, such a code is not to be mistaken with classical molecular dynamics. The PIC code is a method to solve the Vlasov-Landau equation (2.2). To that end, the exact one-particle distribution function or measure, f_α, is approximated by the Dirac measure in momentum space, $f_{\alpha,D}$:

$$f_{\alpha,D}(t,\boldsymbol{r},\boldsymbol{p}) = \sum_{p=1}^{N} w_p\, S(\boldsymbol{r}-\boldsymbol{r}_p(t))\delta(\boldsymbol{p}-\boldsymbol{p}_p(t))\,, \tag{2.3}$$

where the sum runs over N macroparticles. w_p, $\boldsymbol{r}_p$, $\boldsymbol{p}_p$ and S are the weight, the position and the momentum and the shape-function of a macroparticle. Convergence is reached in the limit $\lim_{N\to\infty} f_{\alpha,D} = f_\alpha$ [55]. The PIC code also resolves the Maxwell equations from the macroparticles current and density. The steps for the dynamics of macroparticles in a PIC code, illustrated in Fig. 2.1, are the following:

- Density and current are calculated by projection of the macroparticles on the nodes
- It allows to calculate the $\boldsymbol{E}$ and $\boldsymbol{B}$ fields with the Maxwell equations, using finite difference method
- The fields on the nodes are interpolated at the macroparticle positions so as to apply the Lorentz force
- The macroparticles are "pushed" and the process starts again with the new macroparticles' position.

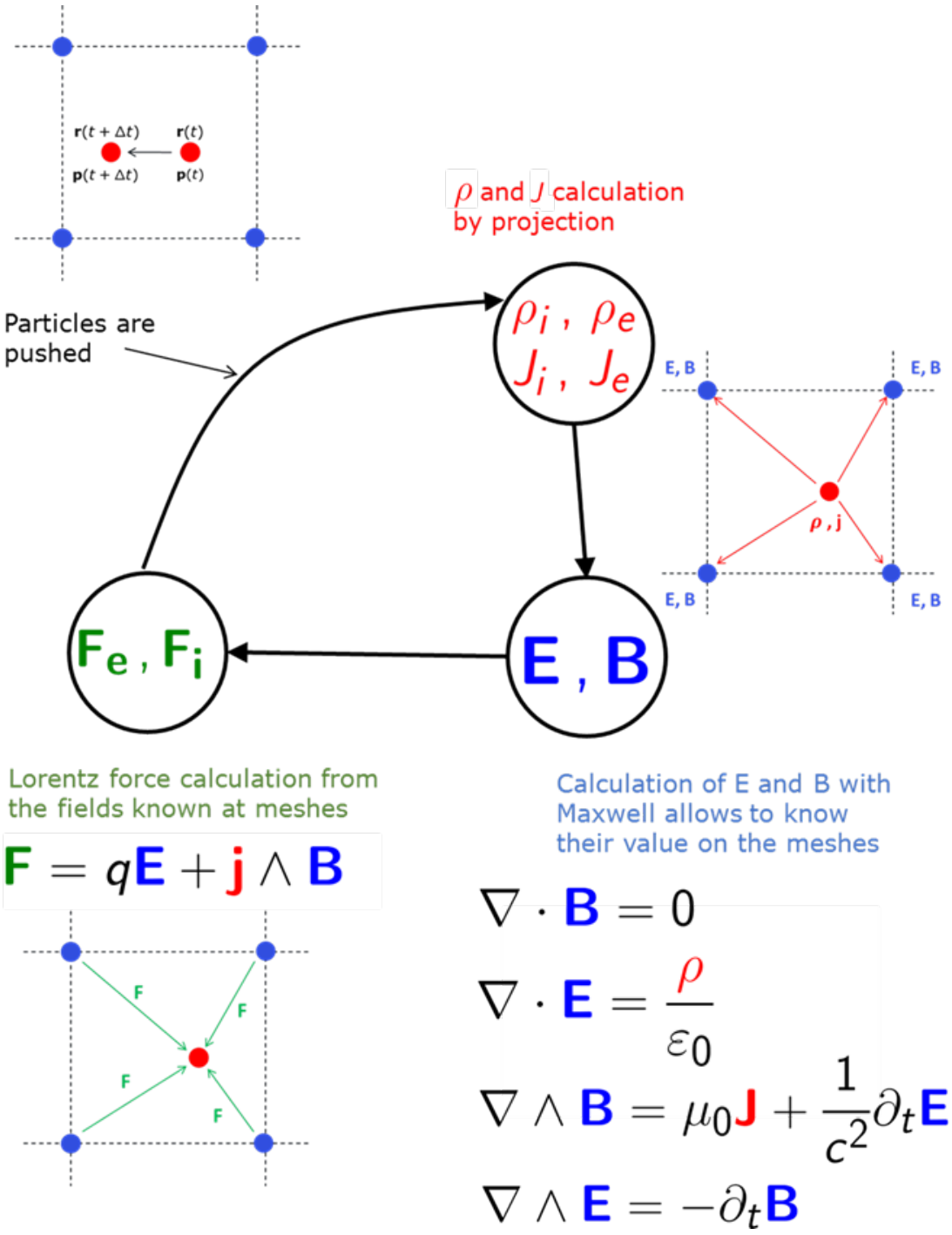

Figure 2.1: Schematic representation of the PIC loop steps

2.1.2 Plasma fluid description

The plasma fluid theory consists in integrating the distribution function over velocity space in order to obtain macroscopic quantities as the density, averaged fluid velocity or averaged kinetic energy of the particles. Various approaches exist among which, the multi-fluid and the single-fluid theories. Multi-fluid models are either used when the charge separation has an important contribution in the plasma dynamics, or when the collisionality becomes weak. Yet, a single-fluid approach proves sufficient for a large range of applications, including most of ICF plasmas.

The fluid equations are found by calculating the so-called Vlasov's moments. The zero-order moment is obtained by integrating the Vlasov equation, the first moment by integrating the Vlasov equation multiplied by the momentum $m\boldsymbol{v}$, the second-order moment by integrating the Vlasov equation multiplied by the energy $m\boldsymbol{v}^2/2$ and so on.
Let us first define the fluid quantities: the density,

$$n(\boldsymbol{r},t) = \int_{\mathbb{R}^3} f(\boldsymbol{r},\boldsymbol{v},t) d^3v \,, \tag{2.4}$$

the mean velocity,

$$\boldsymbol{u}(\boldsymbol{r},t) = \frac{1}{n(\boldsymbol{r},t)} \int_{\mathbb{R}^3} \boldsymbol{v} f(\boldsymbol{r},\boldsymbol{v},t) d^3v \,, \tag{2.5}$$

and the pressure tensor,

$$\overline{\overline{P}} = m \int_{\mathbb{R}^3} (\boldsymbol{v}-\boldsymbol{u}) \otimes (\boldsymbol{v}-\boldsymbol{u}) f(\boldsymbol{r},\boldsymbol{v},t) d^3v \,, \tag{2.6}$$

where $\otimes$ is the tensorial product. As $\boldsymbol{r}$ and $\boldsymbol{v}$ are independent and the Lorentz force is a divergence-free vector field ($\nabla_{\mathbf{v}} \cdot (\boldsymbol{E} + \boldsymbol{v} \wedge \boldsymbol{B}) = 0$), the Vlasov equation (2.1) can be written

$$\partial_t f(\boldsymbol{r},\boldsymbol{v},t) + \boldsymbol{\nabla}_{\boldsymbol{r}} \cdot (\boldsymbol{v} f) + \boldsymbol{\nabla}_{\boldsymbol{v}} \cdot \big[\frac{q}{m}(\boldsymbol{E} + \boldsymbol{v} \wedge \boldsymbol{B}) f\big] = 0 \,. \tag{2.7}$$

The first moment of Vlasov equation consists in integrating Eq. (2.7) along $\boldsymbol{v}$. With the definitions of Eq. (2.4) and (2.5) the integration leads to the particles conservation equation:

$$\partial_t n + \boldsymbol{\nabla} \cdot n\boldsymbol{u} = 0 \,, \tag{2.8}$$

known as the continuity equation. The first-order moment is found by multiplying Eq. (2.7) by $m\boldsymbol{v}$ and then integrating along $\boldsymbol{v}$, leading to

$$m\partial_t n\boldsymbol{u} + m\boldsymbol{\nabla}\cdot n(\boldsymbol{u})^2 = -\nabla_{\boldsymbol{r}}\cdot\boldsymbol{p} + qn\big[\boldsymbol{E} + \boldsymbol{u}\wedge\boldsymbol{B}\big]\,, \tag{2.9}$$

Using Eq. (2.8), the equation becomes the momentum conservation equation

$$mn\partial_t\boldsymbol{u} + mn(\boldsymbol{u}\cdot\boldsymbol{\nabla}\boldsymbol{u}) = -\nabla_{\boldsymbol{r}}\cdot\boldsymbol{p} + qn\big[\boldsymbol{E} + \boldsymbol{u}\wedge\boldsymbol{B}\big]\,. \tag{2.10}$$

Each moment of the Vlasov equation is coupled to the higher order moment. A closure can be obtained using equation of states and slightly out-of-equilibrium models. For instance, a fluid dynamics restricted to the density and momentum conservation equations will require a closure on the pressure tensor, as done for the IAW in the first part of Section 4.2.

2.2 Laser-Plasma Interactions

This short description of some fundamental Laser Plasma Interaction (LPI) phenomena is intended to provide the background in which CBET takes place as well as to explain the need for laser smoothing. Figure 2.5 summarizes all the mentioned instabilities and locates the regions in the holrhaum where they are expected to appear.

2.2.1 Bragg scattering

Bragg scattering occurs when light interacts with a density grating. If the reflected lights from each density modulation are in phase with each other, their interaction results in an intense reflection of the incident beam.

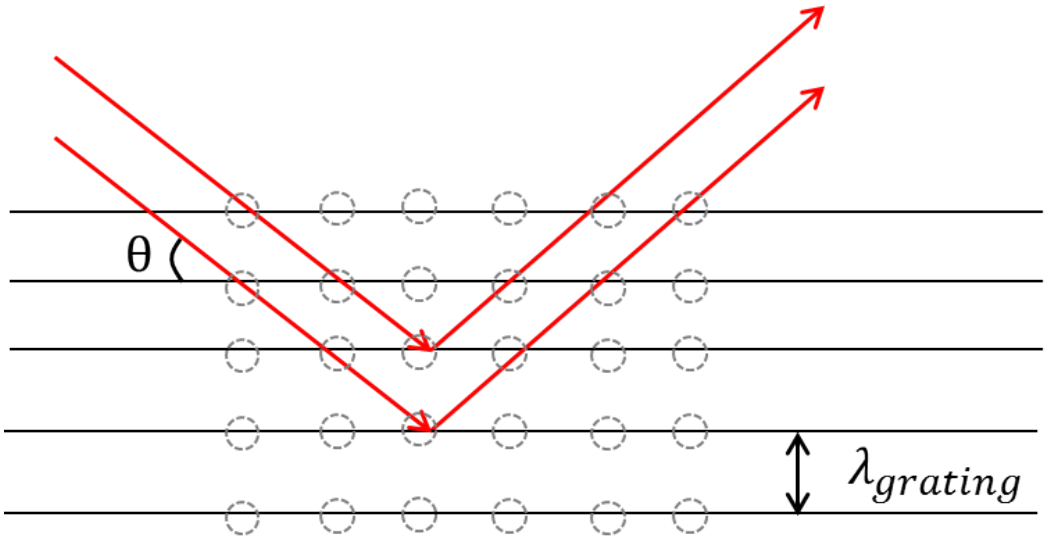

Figure 2.2: Illustration of the Bragg condition

The resonance relation (known as Bragg condition) writes

$$\lambda_{beam} = 2\lambda_{grating} \sin\theta \,. \tag{2.11}$$

In this thesis framework, this situation is found when the IAW is formed in the Speckle Crossing (SC) area and leads to a density modulation with the wavelength $\lambda_{grating}$. Bragg scattering involves the partial or total reflection of a beam on a pre-existent density modulation which can therefore be seen as a particular case of Brillouin scattering, implying the same resonance conditions. CBET is in turn a particular case of Bragg scattering as the grating is formed by two incident beams including the diffracted beam itself. The Bragg scattering scheme represented in Fig. 2.2 can also represent the density modulation showed in Fig. 1.6 (lower right). Likewise, the Bragg condition can be expressed with the CBET geometry of Fig. 1.6 (lower left): $k = k_0 - k_1 \simeq 2k_0 \sin\theta$. Then, writing $k_0 = 2\pi/\lambda_{beam}$ and $k = 2\pi/\lambda_{grating}$ allows to find Eq. (2.11). At a microscopic scale, the incident wave is scattered by electrons. For this reason, the wave equations will be written with N_e in the following chapters.

2.2.2 Self-focusing

Light self-focusing results from the action of a laser beam on the plasma. The beam ponderomotive force pushes the electrons away, thus modifying the refractive index which in turn

modifies the beam propagation, whence the name of "self"-focusing. The modification of the refractive index by the laser beam depends on the beam intensity and is non-uniform. When the density is larger at the center than at the periphery, a convergent lens is formed. Conversely, when the density is larger at the periphery, it creates a divergent lens. Self-focusing occurs when the beam power P exceeds a critical power P_{cr} where [70]

$$P_{cr} \simeq \frac{1.86}{\pi} \frac{n_c^2}{n_e} c k_B T_e \lambda_L^2 \sqrt{1 - n_e/n_c}\,, \tag{2.12}$$

where λ_L is the laser wavelength, n_e the electronic density, n_c the critical density, T_e the electronic temperature. This critical power corresponds to the equilibrium between diffraction and self-focusing: when the two effects compensate, the beam propagates with a constant diameter, which is called self-trapping [11]. However, the relevance of the latter situation, not observed experimentally, is questionable in a non-ideal plasma.

$$P < P_{cr} : \text{diffraction}\,,$$

$$P = P_{cr} : \text{self-trapping}\,,$$

$$P > P_{cr} : \text{self-focusing}\,.$$

2.2.3 Filamentation

Modulational instabilities together with self-focusing lead to a splitting of the beam into filaments. Filamentation [87, 3, 6] is an instability where an incident Electromagnetic Wave (EMW) wave $(\omega_0, \boldsymbol{k_0})$ breaks into Stokes and anti-Stokes scattered EMWs and a nearly stationary ion density modulation $(\omega, \boldsymbol{k})$. The beam usually breaks because of wavefront perturbations in N filaments when P > N P_{cr} where P_{cr} is defined in Eq. (2.12). As ω is small in front of all the other pulsations, it is often considered that $\omega = 0$.

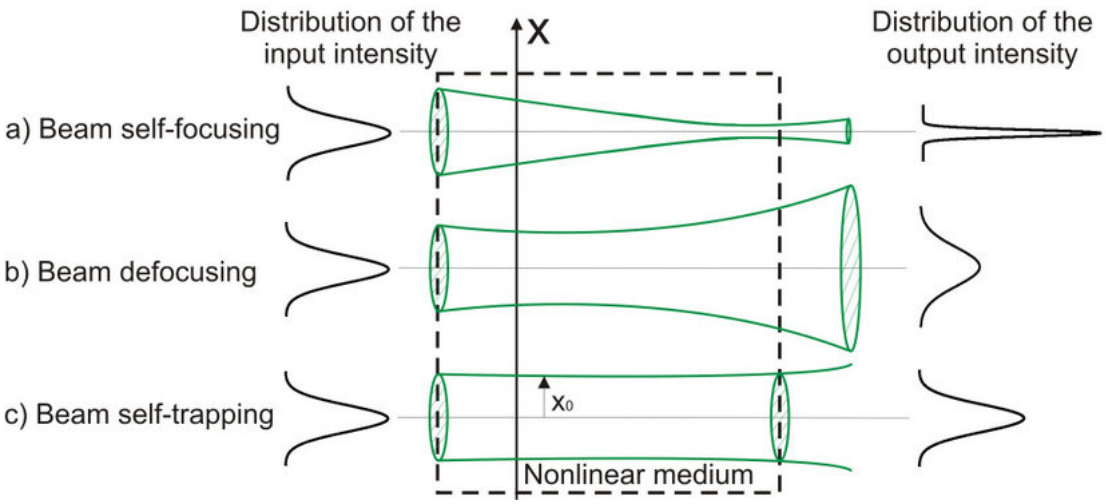

Figure 2.3: Propagation of a laser beam in a non-linear medium (here: the plasma) a) with a focusing non-linearity and b) with a de-focusing non-linearity of the refractive index; c) with the mechanism of nonlinear self-focusing compensated by the divergence caused by diffraction, generating self-trapping. From [110]

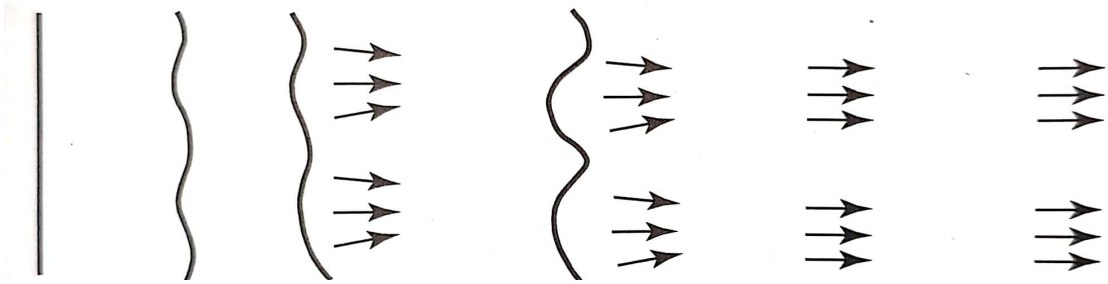

Figure 2.4: Perturbed wavefront scattering into two filaments. From [5]

In theory, filamentation should not occur for an unperturbed wavefront. In ICF experiments, the beam passes through a certain number of optics producing aberrations in the laser wavefront. Filamentation then appears systematically and strongly harms the experiments. Figure 2.5 (down, left) shows one example of filamentation geometry and a location where it can appear in ICF.

2.2.4 Raman and Brillouin scattering

Although not involving the same waves, there are similarities between these two phenomena. When a laser beam illuminates a non-linear medium, a scattered light with a different frequency

can be observed. Components shifted to lower/higher frequencies are called Stokes/anti-Stokes components.

Raman scattering

Stimulated Raman Scattering (SRS) is a decay instability where an incident EMW wave $(\omega_0, \boldsymbol{k_0})$ breaks into a scattered EMW $(\omega_1, \boldsymbol{k_1})$ wave and an Electron Plasma Wave (EPW) $(\omega_p, \boldsymbol{k_p})$ wave. The resonance conditions write

$$\omega_0 = \omega_1 + \omega_p \,, \tag{2.13}$$

$$\boldsymbol{k_0} = \boldsymbol{k_1} + \boldsymbol{k_p} \,. \tag{2.14}$$

The dispersion equation of the EMW

$$\omega_1^2 = \omega_{pe}^2 + k_1^2 c^2 \,, \tag{2.15}$$

and of the EPW

$$\omega_p^2 = \omega_{pe}^2 + 3k_p^2 v_{T_e}^2 \,, \tag{2.16}$$

implies that $\omega_0 \geq 2\omega_{pe}$ and therefore $n_{e,0}/n_c \leq 1/4$. Figure 2.5 (down, right) shows one example of backward Raman scattering geometry and a location where it can appear in ICF.

Brillouin scattering

Stimulated Brillouin Scattering (SBS) is a decay instability where an incident EMW wave $(\omega_0, \boldsymbol{k_0})$ breaks into a scattered EMW $(\omega_1, \boldsymbol{k_1})$ wave and an IAW $(\omega, \boldsymbol{k})$ wave. The resonance conditions write

$$\omega_0 = \omega_1 + \omega \,, \tag{2.17}$$

$$\boldsymbol{k_0} = \boldsymbol{k_1} + \boldsymbol{k} \,, \tag{2.18}$$

with ω and k verifying the IAW dispersion equation in the limit $k^2\lambda_D^2 \ll 1$

$$\omega = k c_s \,. \tag{2.19}$$

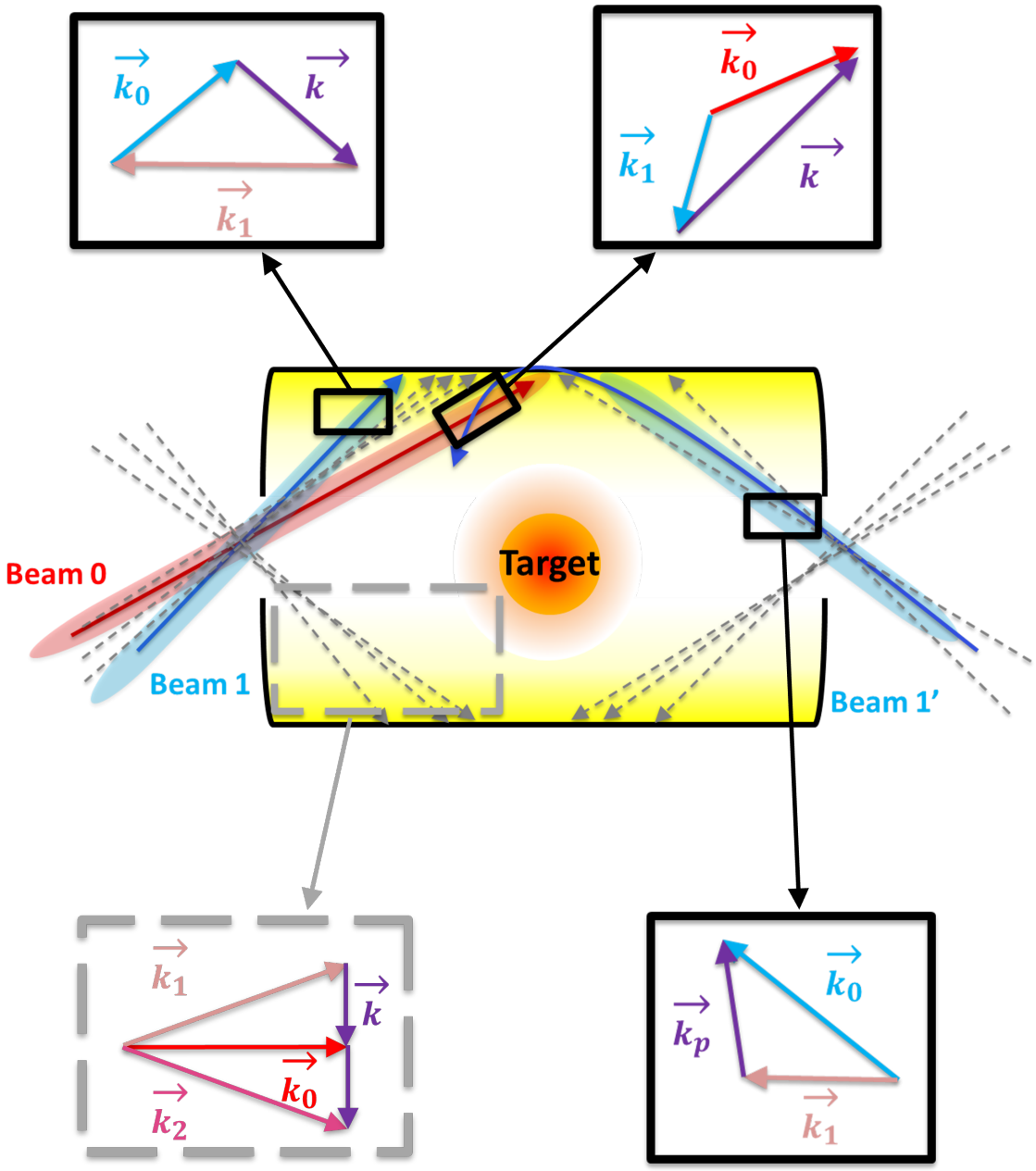

Figure 2.5: Illustration of the instabilities that take place in the Holrhaum. Dark rectangles exhibit the ubiquitous instabilities: (up left) Stimulated Brillouin Back-Scattering (up right) Cross Beam Energy Transfer (down right) Stimulated Raman Back-Scattering and dashed gray rectangle shows filamentation, which can appear, or not at different locations.

Figure 2.5 (up, left) shows one example of backward Brillouin scattering geometry and a location where it can appear in ICF. Forward scattering ($\boldsymbol{k_0}$ and $\boldsymbol{k_1}$ collinear and in the

same direction) and side scattering (different orientations of the vectors) also exist. However, backward geometry is more easily characterized experimentally. Moreover, CBET can be seen as a particular case of SBS. In this regard, Figure 2.5 (up, right) represents CBET but also Brillouin side scattering.

2.3 Laser smoothing techniques

In ICF experiments, a laser beam goes through a large number of optics. The laser beam phase is highly modified during the propagation in the amplifying chain, leading to the presence of strong inhomogeneities. The aforementioned instabilities develop in these inhomogeneities, severely damaging the implosion. Optical smoothing is meant to reduce these inhomogeneities by breaking the spatial and temporal coherence of the laser. Reducing the characteristic laser lengths and times allows to stay under the critical point of instabilities development. To this end, the beam is fragmented into many hot spots called speckles. Optical smoothing was developed to avoid self-focusing and the subsequent filamentation as described in Section 2.2.3, nevertheless the threshold of other instabilities, such as SBS or SRS described in Section 2.2.4, are often reached.

2.3.1 Random Phase Plate

Random Phase Mask was first used for improving the recording of Fourier transform holograms [7]. In parallel, different techniques [100, 63, 58] were developed to improve the homogeneity of the compression in ICF. The combination between the random phase technique and the search for homogeneity resulted in the so-called Random Phase Shifter [40, 41], precursor of RPP. The spatial coherence break is obtained by inserting a RPP on the beams path, as illustrated in Fig. 2.6. The simplest phase plate configuration is the following: half of the elements induces a phase shift of $\varphi = \pi$ whereas the other half keeps the phase unchanged. This configuration is schematized in Fig. 2.7. Note that a similar class of RPP can be used but with the phase φ randomly distributed between 0 and 2π.

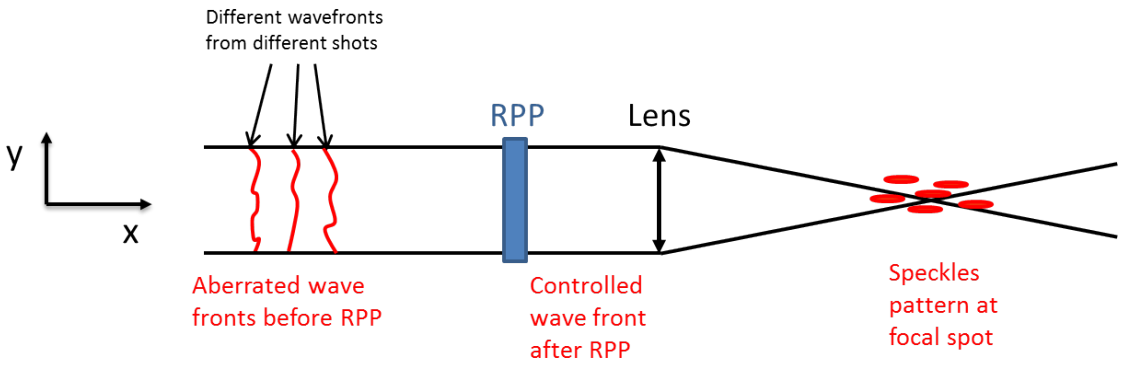

Figure 2.6: Laser beam path through RPP and lens until the focal spot.

The field at focal spot after the lens and this phase plate can be considered as a sum of random phase wavelets. The intensity pattern is thus constituted of the interferences between the wavelets, resulting in the hot spot (speckle) structure. The field writes

$$E(x_+, \boldsymbol{r}_\perp, t) = \frac{E(x_-, \boldsymbol{r}_\perp, t)}{(N+1)^2} \sum_{\mathbf{k}=(0,k_y^\perp,k_z^\perp)} e^{i\mathbf{k}\cdot\mathbf{r}_\perp + i\varphi(\mathbf{k})}\,, \tag{2.20}$$

where $x_{+/-}$ designates the x position just after/before the phase plate, $k_{y/z}^\perp = 2k_{max}n_{y/z}/(N+1)$ with $k_{max} = k_0 D/2f$, $n_{y/z} \in [\![-N/2, N/2]\!]$ and $\boldsymbol{r}_\perp$ is the position vector in the plane orthogonal to the field propagation direction, also corresponding to the phase plate plane.

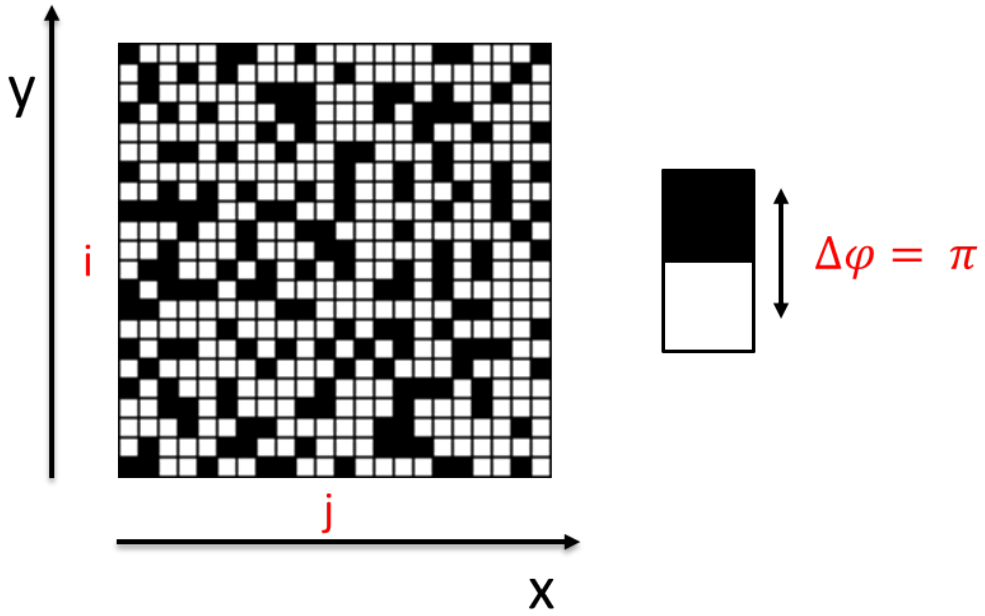

Figure 2.7: 2D RPP scheme

Figure 2.8 shows the shape of a transversal and a longitudinal cross section of a RPP smoothed laser beam, plotted with the calculation in Chapter 3, made with the RPP presented above.

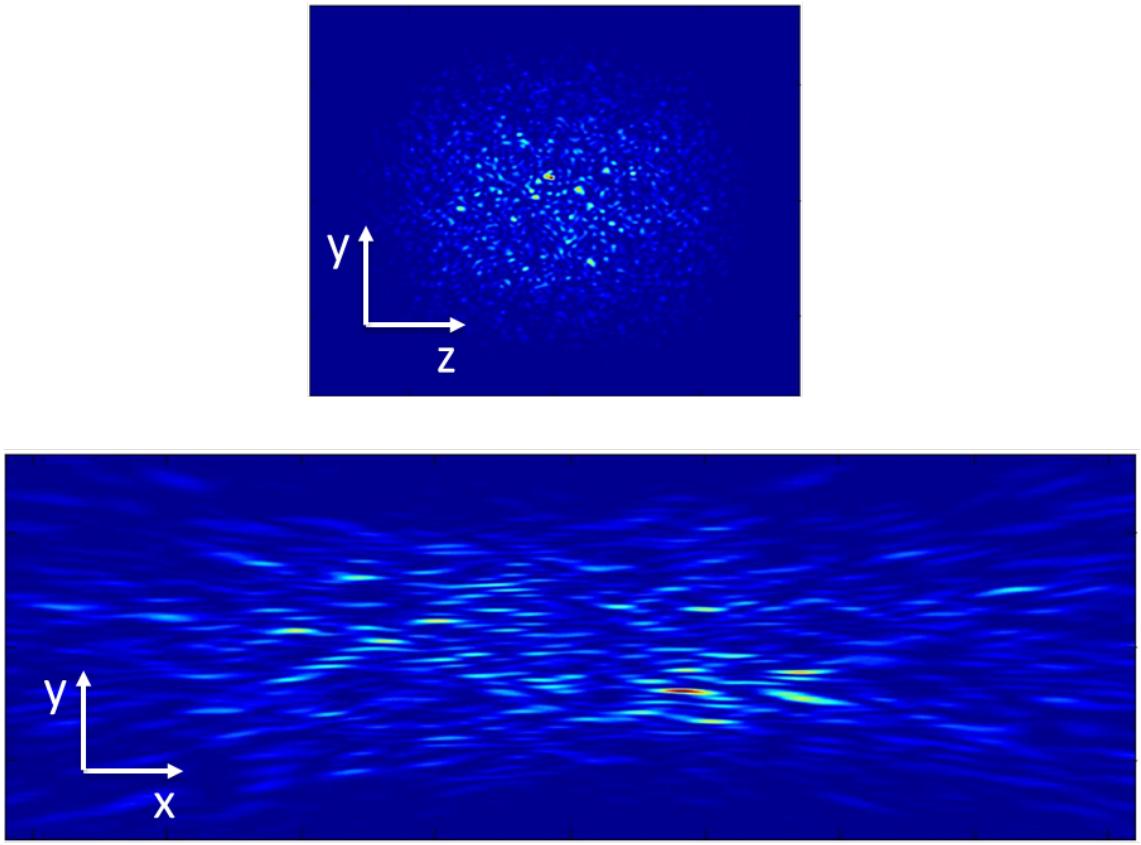

Figure 2.8: Transverse (up) and longitudinal (down) cross section of a smoothed laser beam

In the LMJ experimental conditions, speckles are a few microns wide and about a hundred microns long. However, RPP is actually not the spatial smoothing technique used in ICF facilities. A first improvement was made with the so-called Kinoform Phase Plate (KPP) [21], consisting in a multilevel phase plate. At LMJ, OMEGA and NIF, Continuous Phase Plate (CPP) is used [75, 62]. The principle is similar to RPP, but the phase modulation is continuous instead of being composed of regular geometrical phase plates. A typical CPP is shown in Fig. 2.9. However, RPP will still be the phase plate studied in this manuscript since it is the most convenient to model.

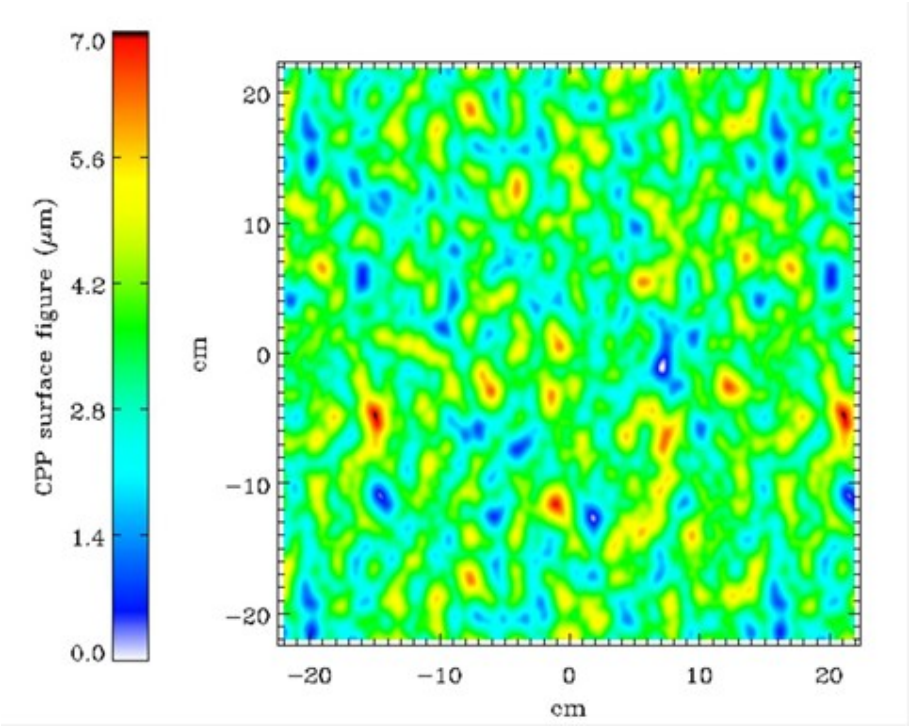

Figure 2.9: Example of the surface profile of a typical continuous phase plate, from the NIF user guide [43]. The colormap indicates the thickness variation of the phase plate inducing the phase shift.

Spatial smoothing also absorbs shot-to-shot aberrations (see Fig. 2.6), since the phase differences due to these aberrations are lost by the random phase of the plate. The formed speckles remain, however, stationary, potentially allowing the instabilities to develop after their characteristic time. Thus, the spatial smoothing sometimes needs to be completed by a temporal smoothing.

2.3.2 Smoothing by Spectral Dispersion

To break the temporal coherence, a sinusoidal phase modulator is inserted on the beam path to add a phase $\beta_m \sin(\omega_m t)$ to the incident laser wave, with a modulation frequency ω_m and a modulation depth β_m. The resulting laser spectrum is thus broadened. Then the laser light in the near field is slightly dispersed so that each spectral component creates its own independent speckle pattern. This process is called Smoothing by Spectral Dispersion (SSD), and together

with the RPP, the electric field at focal spot is modified as follows [102]:

$$E(x,\boldsymbol{r}_\perp,t)=\frac{E_0}{(N+1)^2}e^{ik_0x-i\omega_0t}\sum_{\mathbf{k}=(0,k_y^\perp,k_z^\perp)}e^{i\beta_m\sin\left\{\omega_m[t+T_rf_{T/L}(\mathbf{k})]\right\}+i\mathbf{k}\cdot\mathbf{r}_\perp+i\varphi(\mathbf{k})}. \quad (2.21)$$

Here $T_rf_{T/L}(\mathbf{k})$ is the SSD phase shift which may vary depending on the techniques used. On NIF, the phase shift imposed is along one transverse direction ($f_T(\mathbf{k})=k_y/k_m$, 1D transverse SSD). On the LMJ the phase shift is radial ($f_L(\mathbf{k})=\mathbf{k}^2/k_m^2$, longitudinal SSD). On Omega, two successive 1D transverse SSD are imposed along y and z: 2D SSD. Each spectral component creates its own independent speckles pattern that will lower the contrast by adding to the others. The coherence time of the speckles will be of the order of the inverse of the spectral width $\Delta\omega=2\beta_m\omega_m$.

The SSD is presented above to set the context but will not be studied in this manuscript. In contrast, the RPP formulation will be used.

2.4 State of the art

The numerous phenomena and the smoothing methods presented above are closely related to CBET. The foundations have now been laid, and allow a detailed overview of the state of the art, from the precursors of CBET studies to the current research areas.

2.4.1 Origin of Cross-Beam Energy Transfer

The aim of this section is not to make an exhaustive list of studies that have led to our current knowledge of CBET, nor to make a strict historical chronology, but to give an overview of how understanding of LPI has developed and made CBET become a proper subject of study. Note that the term CBET was only introduced in 2012 [30] but we will use it anachronistically.

Light scattering as a plasma probe

Interests in the study of the scattering of electromagnetic radiation in a plasma appeared because of the possibility it offers to study the internal structure and dynamics of the plasma. Indeed, light scattering is closely linked to the generation of electronic plasma waves. It was however difficult to observe this so-called Thomson scattering of light by electrons because the

cross section of the process is very small. Ruby optical masers [96, 38, 52] permit an increased beam power ($10^5\,W$) [36] allowing to observe the scattered light despite the small cross section. As a matter of fact, the scattered maser light is polarized whereas the self-luminosity of the plasma is not, or only slightly. Development of maser/laser and techniques such as light-off-light scattering [88] has improved the counting rate of the scattering but the cross section remains small. To overcome this obstacle, an approach called optical mixing has been found. A theoretical work [49] first predicted the possibility of making a density probe with three laser beams. This work suggests to excite longitudinal electron plasma oscillations with two crossing beams and to send a third laser on this wave as a probe. The tuning of the beams frequency allows to satisfy the EPW resonance condition and to enhance the cross section size. The first experiment [104] measured the increasing probe beam intensity when the crossing lasers are tuned in the plasma resonance. Knowing the frequency difference, it is possible to accurately estimate the plasma density. In the first instance, optical mixing was only used as a diagnostic tool. Afterwards, it received interest as a source of controlled EPW [74], opening the way to other applications such as electron acceleration [108, 12], plasma heating [95, 14], and also plasma-wave physics what we now call LPI.

Beginning of laser-fusion concerns: Ionic Acoustic Waves generation

In most studies about EPW generated by wave mixing, ions have been considered as an immobile background, but experiments have shown the excitation of IAW by a similar mechanism [105]. Calculations taking into account the ion dynamics showed that under specific conditions it is easier to stimulate IAW than EPW and that the growth rate of the IAW can exceed the collisional damping [101]. The production of IAW and the energy transfer from high to low frequency has been seen as an opportunity to produce efficient laser frequency converter [97]. The first experiment of IAW generated by laser optical mixing [86] confirmed the prediction of optical mixing theory. In particular, it has been shown that for power $< 25\,kW$ the density fluctuation only depends on the product of the beams field and not on their respective value. For bigger power, a non-linear saturation mechanism identified as ion heating was found. Although it can be used as a frequency converter tool, this energy transfer has also been identified as an obstacle for fusion experiments. The laser-produced plasma in laser fusion experiments may expand at the ion acoustic velocity. Because of the reflection of the pump beam on the target, a resonance condition between the resulting beat wave and an IAW appears, enhancing the scattered wave [2]. Later, a theory of an ion wave created directly by the beams crossing [90] emerged and showed that the rate of energy exchange is stronger in the case of this stimulated

IAW than in the case of preexisting ion acoustic fluctuation levels. Afterwards, CBET from frequency mismatched laser beams in a stationary plasma has been observed [44].

Beginning of laser-fusion concerns: mitigation of Cross-Beam Energy Transfer

Solutions were soon proposed [50] and studied [24, 31, 73] to diminish the growth rate of Brillouin scattering, such as using a finite bandwidth and a random phase modulation, forerunners of our actual temporal and spatial smoothing.

Analytical description of CBET evolved in conjunction with the development of smoothing techniques in order to best adapt them. A one-dimensional and steady-state calculation of the transferred power has thus emphasized the effects of the beams frequency mismatch as well as the inhomogeneity and modulation of the plasma [51]. Then, a two-dimensional analysis of the transient response of the power exchanged has been studied [66] and showed that the exchange oscillates in time and is usually smaller in the steady-state regime. All these studies were made by supposing monochromatic Gaussian beams, and the theory was only made for the asymptotic regime. It resulted in a monotonic transfer of power from one beam (high frequency) to another (low frequency). The first study with multi-chromatic beams [65] showed a periodic oscillatory exchange between the two beams: the higher frequency components of one beam giving to the lower components of the other beam, even in steady-state regime. The first experiment [115] and simulation [13] demonstrating the energy exchange in a flowing plasma confirmed the need for frequency tuning in the fusion experiments. In the late 20th century, the underlying physics and the conditions under which CBET appears are clear. The subsequent concerns are to improve its modeling and try to control it in order to perform the fusion experiments.

2.4.2 Current research

Motivations

Once CBET has been identified as a threat for ignition, two research paths have been explored simultaneously. How to reduce CBET, but also how inherent physical phenomena can saturate the exchange. It has been found that localized pump depletion and non-linear phenomena induce a saturation of the IAW [45]. In particular, ion trapping reduces the Landau-damping rate, increasing the IAW amplitude, but can also induce a saturation by shifting the IAW

frequency [116]. These saturation mechanisms however still allow a certain amount of energy exchange, making it necessary to find a way to mitigate CBET. While undesired CBET has been found to alter the implosion symmetry, it can also be used as a tool to improve it by imposing wavelength shift between beams. Wavelength detuning simulations including RPP, SSD and Polarization Smoothing (PS) have shown a great improvement in the implosion symmetry [67]. A proper understanding and modeling of CBET is therefore needed not only for its mitigation, but also for its use as a powerful tool.

Lacks in Cross-Beam Energy Transfer modeling

Models using the averaged field intensity have a tendency to overestimate the energy exchange measured in experimental campaigns, and a saturation mechanism must usually be invoked in order to match the experiments [59, 71, 47]. Ion trapping, stochastic heating [67, 118, 35], and velocity perturbations of the plasma flow [76, 64, 51] have been identified as potential saturation mechanisms of CBET. Moreover, dedicated theoretical studies on smoothed laser beams have demonstrated that the competition of CBET with processes such as self-focusing and beam bending [89, 37] is able to affect the overall energy exchange. Finally, recent theoretical and numerical studies have shown that CBET is effectively diminished by imposing a frequency laser bandwidth exceeding the IAW frequency [98, 99]. Even though CBET is not yet fully understood and well-modeled, the previous studies have allowed a great control of the implosion symmetry of the recent NIF experiment [121], as pointed out in Section 1.3.1.

Thesis prospects

Hydrodynamic simulations results tend to overestimate CBET compared to experimental results. The motivation is to understand this discrepancy. The following work aims at showing that even without invoking any nonlinear saturation mechanism, the predictions of linear models can be improved by accounting for the inter-dependencies of SCs, as recently argued in Refs. [85, 84].
In the following, we study CBET in the linear perturbation approach.

The novelty of this manuscript lies in:

- The field calculation with a RPP in Section 3.2.
- The improvement of the model of Section 4.3.2 with the addition of the time component.

- In the Chapters 5 and 6, a linear theory has been developed and extensive PIC simulations have been performed. The comparison between the analytical and numerical results shows a good agreement for a large range of parameters.

Chapter 3

Beam propagation without coupling and speckles modeling

Contents

This chapter first presents the basic laser beam propagation theory that will be the starting point of Chapter 4. Then, the expression of the laser beam field passing through a RPP is computed and will be used in the model and the simulations exposed in Chapter 6. Finally, the calculation of the transversal and longitudinal autocorrelation functions are made to reveal the speckles' geometric shape. From now, the following normalizations

$$t = \omega_L t' \,, \tag{3.1}$$

$$\omega = \omega'/\omega_L \,, \tag{3.2}$$

$$x = k_L x' \,, \tag{3.3}$$

$$k = k'/k_L \,, \tag{3.4}$$

$$n_e = \frac{n'_e}{n_c} \,, \tag{3.5}$$

$$v = \frac{v'}{c} \,, \tag{3.6}$$

$$m_i = \frac{m'_i}{m'_e} \,, \tag{3.7}$$

$$E = \frac{eE'}{m_e \omega_L c} \,, \tag{3.8}$$

$$B = \frac{eB'}{m_e \omega_L} \,, \tag{3.9}$$

$$A = \frac{eA'}{m_e c} \,, \tag{3.10}$$

$$V = \frac{eV'}{m_e c^2} \,, \tag{3.11}$$

$$a_0 = 0.855\sqrt{I_{10^{18}\,\mathrm{Wcm^{-2}}}\,\lambda^2_{\mu m}} \,, \tag{3.12}$$

are applied respectively for time, frequency, space, wave vector, density, velocity, mass and the fields. ω_L and k_L are the frequency and the wave number in vacuum for a $1\,\mu m$ laser wavelength. This normalisation allows to simplify the equations while keeping ω explicit for the readability. n'_e is the electronic density, $n_c = m_e \varepsilon_0 \omega_L^2 / e^2$ the critical density, $m'_{i,e}$ the ionic/electronic mass, E' the electric field, B' the magnetic field, A' the vector potential and V' the electrostatic potential. a_0 is the potential vector normalized to $m'_e c/e$, for a linearly polarized laser pulse, with $I_{10^{18}\,\mathrm{Wcm^{-2}}}$ the laser intensity in units of $10^{18}\,\mathrm{Wcm^{-2}}$ and $\lambda_{\mu m}$ the laser wavelength in μm.

3.1 Description of the beam propagation

3.1.1 General description

The light propagation in the classical limit is described by the electric and magnetic fields variations, related to each other by Maxwell equations. The choice has been made to derive the equations with the potential vector $\boldsymbol{A}$ in order to use the conservation of the canonical momentum. The potential vector $\boldsymbol{A}$ is related to the magnetic and electric field by $\boldsymbol{B} = \nabla \wedge \boldsymbol{A}$ and $E = -\boldsymbol{\nabla} V - \partial_t \boldsymbol{A}$. The normalized Maxwell-Ampere equation with the potential vector thus leads to

$$\boldsymbol{\nabla} \wedge \boldsymbol{B} = \boldsymbol{\nabla}(\boldsymbol{\nabla} \cdot \boldsymbol{A}) - \Delta \boldsymbol{A}\,, \tag{3.13}$$

$$= \boldsymbol{j} + \partial_t \boldsymbol{E}\,. \tag{3.14}$$

Considering that $\boldsymbol{v_e} \gg \boldsymbol{v_i}$, we can write $\boldsymbol{j} = -n_e \boldsymbol{v_e}$

$$\implies n_e \boldsymbol{v_e} + \partial_t^2 \boldsymbol{A} + \boldsymbol{\nabla}(\boldsymbol{\nabla} \cdot \boldsymbol{A} + \partial_t V) - \Delta \boldsymbol{A} = 0\,. \tag{3.15}$$

In Lorentz gauge: $\boldsymbol{\nabla} \cdot \boldsymbol{A} + \partial_t V = 0$ it remains

$$\Delta \boldsymbol{A} - \partial_t^2 \boldsymbol{A} = n_e \boldsymbol{v_e}\,. \tag{3.16}$$

The complete classical description of light propagation is achieved with the electron momentum conservation equation:

$$\partial_t \boldsymbol{v_e} + (\boldsymbol{v_e} \boldsymbol{\nabla}) \boldsymbol{v_e} = -\boldsymbol{E} - \boldsymbol{v_e} \wedge \boldsymbol{B}\,. \tag{3.17}$$

In the perturbation limit, this equation is linearized around $\boldsymbol{v_e} = 0 + \delta \boldsymbol{v_e}$, leading to:

$$\partial_t \delta \boldsymbol{v_e} = \partial_t \boldsymbol{A}\,. \tag{3.18}$$

Note that we assumed a purely transverse field ($\nabla V = 0$). Thus

$$\delta \boldsymbol{v_e}(\boldsymbol{r}(t), t) = \boldsymbol{A}(\boldsymbol{r}(t), t) + C\,, \tag{3.19}$$

which expresses the conservation of the transverse canonical momentum. As $v(t=0)=0$ (so C=0), Eq. (3.16) rewrites

$$\Delta \boldsymbol{A} - \partial_t^2 \boldsymbol{A} = n_e \boldsymbol{A}\,. \tag{3.20}$$

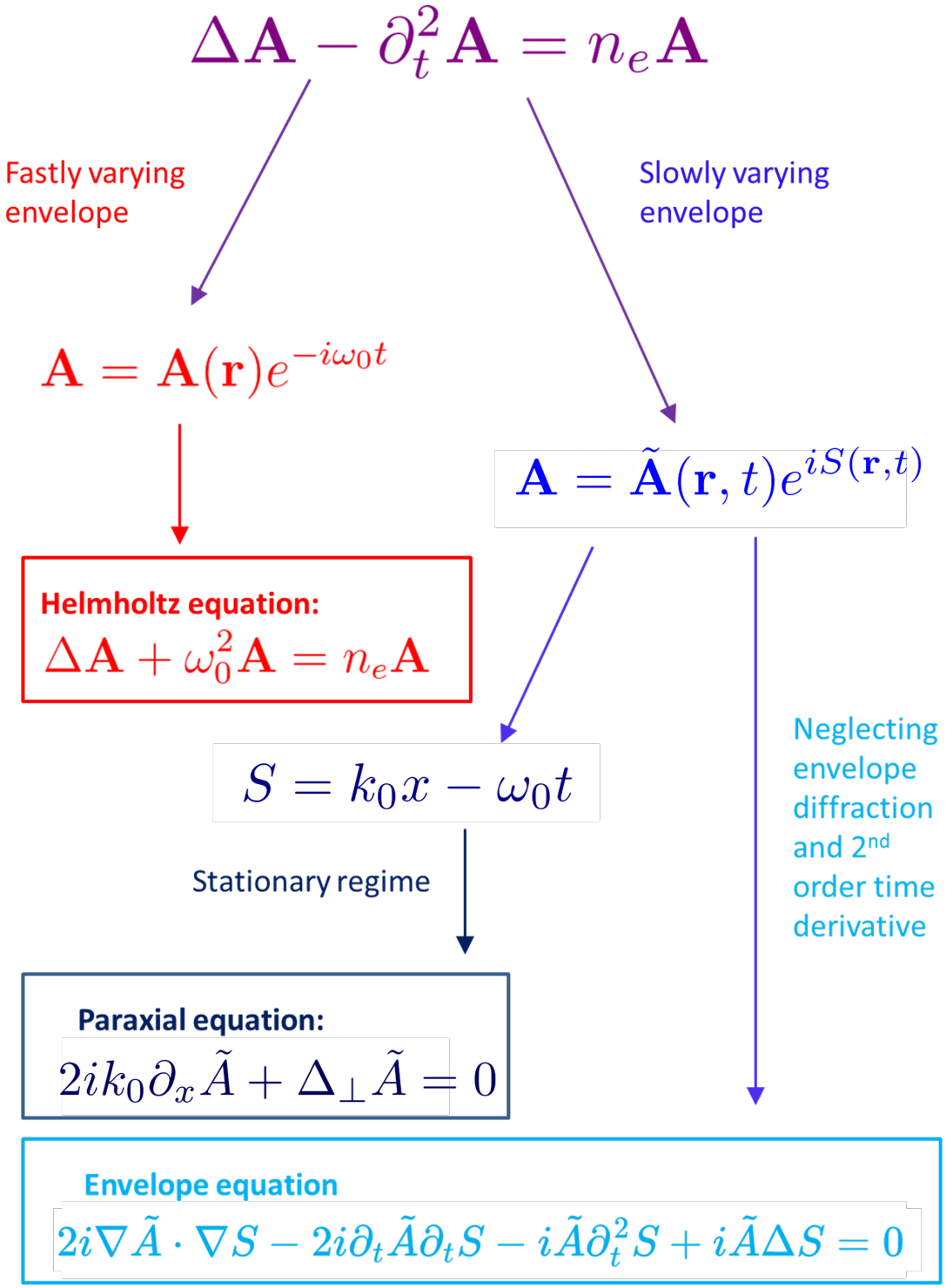

Figure 3.1: Scheme of the different approximations for A leading to the different propagation equations.

This equation allows to study the propagation of A including the field diffraction and refraction. Different approximations on the wave propagation, summarized in Fig. 3.1, can be made using ansatz on the form of the function $\boldsymbol{A}(\boldsymbol{r},t)$.

Helmholtz equation

The first one consists in considering $\boldsymbol{A}(\boldsymbol{r},t) = \boldsymbol{A}(\boldsymbol{r})e^{-i\omega_0 t}$ where $\boldsymbol{A}(\boldsymbol{r})$ can be fastly varying in space and ω_0 is the normalized (to ω_L) laser frequency. In this case, Eq (3.20) leads to the Helhmoltz equation,

$$\Delta\boldsymbol{A} + \omega_0^2\boldsymbol{A} = n_e\boldsymbol{A}\,. \tag{3.21}$$

This equation allows to study the rapidly varying field and is still adapted near the critical density, as it can describe the evanescent wave. Nevertheless, the numerical cost of such a description is high as the laser wavelength ($\sim \mu$m) must be resolved.

Envelope equation

Another case, known as the envelope approximation, assumes the field of the form $\boldsymbol{A}(\boldsymbol{r},t) = \widetilde{\boldsymbol{A}}(\boldsymbol{r},t)e^{iS(\boldsymbol{r},t)}$ where $\widetilde{A}(\boldsymbol{r},t)$ is the slowly varying envelope and $S(\boldsymbol{r},t)$ the rapidly varying phase ($\partial_{\boldsymbol{r},t}\widetilde{\boldsymbol{A}}/\widetilde{\boldsymbol{A}} \ll \partial_{\boldsymbol{r},t}S/S$). Using this closure in equation (3.20), and separating orders, leads to the following set of equation:

$$\text{Order 0:}\quad -(\boldsymbol{\nabla}S)^2 + (\delta_t S)^2 = n_e\,, \tag{3.22}$$

$$\text{Order 1 + 2:}\quad 2i\boldsymbol{\nabla}\widetilde{A}\cdot\boldsymbol{\nabla}S - 2i\partial_t\widetilde{A}\partial_t S + \Delta_\perp\widetilde{A} - i\widetilde{A}\partial_t^2 S + i\widetilde{A}\Delta S = 0\,. \tag{3.23}$$

Equation (3.22) describes the phase variation in relation to the refraction due to the density n_e. Equation (3.23) is the transport equation including the diffraction term $\Delta_\perp\widetilde{A}$. The notation $\Delta_\perp$ means that the Laplace operator is applied in the perpendicular plane to ∇S.

Envelope equation without diffraction

A method consists in neglecting the envelope diffraction and Eq. (3.23) becomes a simple transport equation

$$2i\boldsymbol{\nabla}\widetilde{A}\cdot\boldsymbol{\nabla}S - 2i\partial_t\widetilde{A}\partial_t S - i\widetilde{A}\partial_t^2 S + i\widetilde{A}\Delta S = 0\,. \tag{3.24}$$

This equation, here without the absorption, coupled with the Eikonal equation (3.22) are at the origin of the ray-tracing algorithms in most of hydrodynamic codes. This method neglects the beam diffraction but takes into account the phase variation when the light travels through density gradients.

Paraxial equation

Another class of equation can be obtained, assuming the light remains nearly parallel to an axis. Taking $S = \boldsymbol{k_0} \cdot \boldsymbol{x} - \omega_0 t$, Eq. (3.22) leads to the dispersion equation

$$k_0^2 - \omega_0^2 + n_e = 0\,. \tag{3.25}$$

Eq. (3.23) leads to the well-known paraxial equation:

$$2ik_0\partial_x\widetilde{A} + 2i\omega_0\partial_t\widetilde{A} + \Delta_\perp\widetilde{A} = 0\,. \tag{3.26}$$

In the stationary regime ($\partial_t\widetilde{A} = 0$), the latter becomes

$$2ik_0\partial_x\widetilde{A} + \Delta_\perp\widetilde{A} = 0\,, \tag{3.27}$$

which is the starting point of the usual Gaussian beam propagation calculation.

3.1.2 Gaussian beam propagation

We consider a beam propagating along the x direction. $\Delta_\perp$ is therefore $\partial_y^2 + \partial_z^2$ in 3D and ∂_y^2 in 2D. The Gaussian beam at focal spot writes

$$\widetilde{A} = A_0 e^{-\frac{z^2+y^2}{w_0^2}}\,, \tag{3.28}$$

where w_0 is the beam waist, $x_r = \frac{\pi w_0^2}{\lambda_0}$ is the Rayleigh length, and A_0 the amplitude at the beam center. The following notations are used $w(x) = w_0\sqrt{1 + \frac{x^2}{x_r^2}}$, $R(x) = x + \frac{x_r^2}{x}$.
Figure. 3.2 illustrates the Gaussian beam geometry with the characteristic lengths. The 2D calculation is presented for the sake of simplicity. Besides, the 3D expression can be deduced

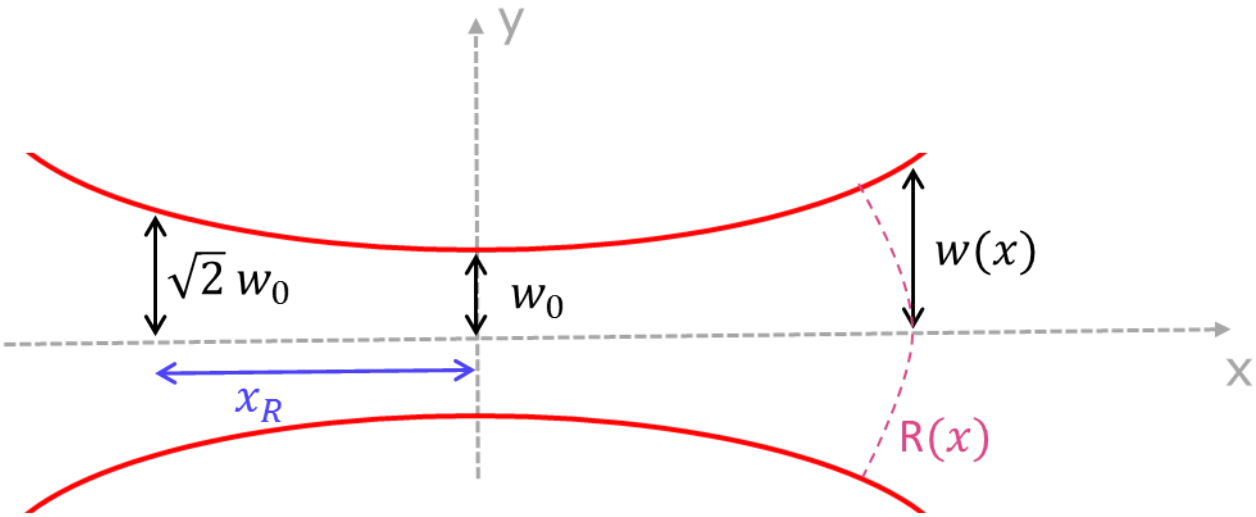

Figure 3.2: Gaussian beam characteristic lengths scheme

from the 2D expression of the field. Fourier Transform (FT) and FT^{-1} respectively design the y Fourier Transform and the inverse Fourier Transform. The FT of the paraxial equation leads to an ordinary differential equation

$$\mathrm{FT}(2ik_0\partial_x\widetilde{A} + \partial_y^2\widetilde{A}) = 2ik_0\partial_x\bar{A} - k_y^2\bar{A} = 0\,, \tag{3.29}$$

with the solution

$$\bar{A} = \bar{A}(x=0)e^{-\frac{ik_y^2 x}{2k_0}}\,, \tag{3.30}$$

where

$$\bar{A}(x=0) = \mathrm{FT}(A_0 e^{-\frac{y^2}{w_0^2}}) = A_0\sqrt{\pi}w_0 e^{-\frac{-w_0^2k_y^2}{4}}\,. \tag{3.31}$$

Then, the field at any position stems from the inverse FT of Eq. (3.30),

$$\begin{aligned}
\mathrm{FT}^{-1}(\bar{A}) = \widetilde{A} &= \frac{A_0 w_0}{\sqrt{w_0^2 + \frac{2ix}{k_0}}} e^{-y^2/(w_0^2+2ix/k_0)}\,, \\
&= \frac{A_0}{\sqrt{1+ix/x_r}} e^{-y^2(w_0^2-\frac{2ix}{k_0})/(w_0^4+4x^2/k_0^2)}\,, \\
&= A_0 \frac{w_0}{w(x)} \sqrt{1-ix/x_r}\, e^{-\frac{y^2}{w_0^2(1+\frac{4x^2}{k_0^2 w_0^4})} + \frac{2ixy^2}{w_0^2 k_0 (w_0^2+\frac{4x^2}{k_0^2 w_0^2})}}\,, \\
&= A_0 \frac{w_0}{w(x)} e^{-\frac{1}{2}\ln(1-ix/x_r)} e^{\frac{ik_0 y^2}{2R(x)}} e^{-\frac{y^2}{w(x)^2}}\,, \\
&= A_0 \frac{w_0}{w(x)} e^{-\frac{1}{2}\ln(\frac{w(x)}{w_0} e^{i\arctan x/x_r})} e^{\frac{ik_0 y^2}{2R(x)}} e^{-\frac{y^2}{w(x)^2}}\,, \\
&= A_0 \sqrt{\frac{w_0}{w(x)}} e^{-i\frac{1}{2}\arctan x/x_r} e^{\frac{ik_0 y^2}{2R(x)}} e^{-\frac{y^2}{w(x)^2}}\,. \qquad (3.32)
\end{aligned}$$

The deduced 3D expression writes

$$\widetilde{A} = A_0 \frac{w_0}{w(x)} e^{-i\arctan\frac{x}{x_r}} e^{\frac{ik_0(z^2+y^2)}{2R(x)}} e^{-\frac{(z^2+y^2)}{w(x)^2}}\,, \qquad (3.33)$$

where $\frac{ik_0(z^2+y^2)}{2R(x)}$ represents the focusing or defocusing phase depending on its sign and $\arctan\frac{x}{x_r}$ is the phase change around the focus called the Gouy phase.

3.2 Field calculation with a Random Phase Plate

As presented in Section 2.3, laser beams in ICF are spatially and temporally smoothed. In this thesis, temporal smoothing is not considered and the spatial smoothing technique used is RPP. To extend the study further than in the previous works, the exact field of a beam passing through a RPP needs to be calculated to make realistic simulations. The RPP field out of the focal spot is usually computed from the field at focal spot, with the Fresnel integral. However, this method only allows to know the field in a direction perpendicular to the optical axis. The field can be computed everywhere, but requires the 2D inverse FT calculation of the field at focal spot, involving a significant numerical cost. The calculation presented in this section allows to know the exact analytical expression of the field everywhere. Moreover, the field at focal spot of two crossing beams with an angle is also required to calculate the

theoretical wave propagation. The calculation of one single beam field passing through a RPP is presented following the same method as in the Gaussian beam case. We will consider a laser beam centered in y=0, propagating along the x direction, passing through a one dimensional RPP. As described in 2.3, the RPP is subdivided in N elements whose phase φ_n is randomly distributed between 0 and 2π. In the following, f designates the focal distance. The calculation is first made with the electric field instead of the potential vector. Indeed, E is more often found in the literature to describe the RPP field and it will be easier to compare our results to the well-known formulations.

3.2.1 General case out of the focal spot

For a laser propagating along the x-axis, the 2D electric field at the phase plate writes:

$$\widetilde{E}(x=0,y) = E_l e^{-\frac{ik_0 y^2}{2f}} H(y-D/2)H(D/2-y)\sum_n e^{i\varphi_n} H(y-a_n)H(a_{n+1}-y)\,, \quad (3.34)$$

$$= E_l e^{-\frac{ik_0 y^2}{2f}} \sum_n e^{i\varphi_n} H(y-a_n)H(a_{n+1}-y)\,. \quad (3.35)$$

We note $a_n = nd$ where d is the size of one phase plate element, $n \in [\![-N/2, N/2]\!]$, and where $(N+1)d = D$ is the size of the phase plate. The phase plate is located after the lens, whence the focusing phase $e^{-\frac{ik_0 y^2}{2f}}$. The amplitude of the field at the lens is E_l.
The propagation equation writes

$$2ik_0\partial_x\widetilde{E} + \partial_y^2\widetilde{E} = 0\,. \quad (3.36)$$

Following a similar procedure as for the Gaussian beam case, the field in the Fourier space writes:

$$\bar{E} = \mathsf{TF}(\widetilde{E}(x=0))e^{-\frac{ik_y^2 x}{2k_0}}\,. \quad (3.37)$$

The solution of $\widetilde{E}(x,y)$ is calculated in the real space by applying the inverse Fourier transform of $e^{-\frac{ik_y^2 x}{2k_0}}$, noting * the convolution product. The calculation is performed for a field

located at $x < f$:

$$\widetilde{E} = \widetilde{E}(x=0) * \left(e^{-i\pi/4}\sqrt{\frac{k_0}{2\pi x}}e^{\frac{ik_0y^2}{2x}}\right),$$

$$= E_l e^{-i\pi/4}\sqrt{\frac{k_0}{2\pi x}}\sum_n e^{i\varphi_n}\int_{-\infty}^{+\infty} H(h-a_n)H(a_{n+1}-h)e^{\frac{-ik_0h^2}{2f}}e^{\frac{ik_0}{2x}(y-h)^2}dh\,,$$

$$= E_l e^{-i\pi/4}\sqrt{\frac{k_0}{2\pi x}}\sum_n e^{i\varphi_n}\int_{a_n}^{a_{n+1}} e^{\frac{-ik_0h^2}{2f}}e^{\frac{ik_0}{2x}(y^2-2yh+h^2)}dh\,,$$

introducing $\boxed{K(x)^2 = \frac{k_0}{2x} - \frac{k_0}{2f}\,,}$

$$\widetilde{E} = E_l e^{-i\pi/4}\sqrt{\frac{k_0}{2\pi x}}\sum_n e^{i\varphi_n}e^{\frac{ik_0y^2}{2x}}\int_{a_n}^{a_{n+1}} e^{ih^2K(x)^2-\frac{ik_0yh}{x}}dh\,, \quad (3.38)$$

$$= E_l e^{-i\pi/4}\sqrt{\frac{k_0}{2\pi x}}\sum_n e^{i\varphi_n}e^{\frac{ik_0y^2}{2x}}\int_{a_n}^{a_{n+1}} e^{iK(x)^2\left(h^2-\frac{k_0yh}{xK(x)^2}\right)}dh\,, \quad (3.39)$$

$$= E_l e^{-i\pi/4}\sqrt{\frac{k_0}{2\pi x}}\sum_n e^{i\varphi_n}e^{\frac{ik_0y^2}{2x}}e^{\frac{-ik_0^2y^2}{4x^2K(x)^2}}\int_{a_n}^{a_{n+1}} e^{iK(x)^2\left(h-\frac{k_0y}{2xK(x)^2}\right)^2}dh\,, \quad (3.40)$$

$$= E_l e^{-i\pi/4}\sqrt{\frac{k_0}{2\pi x}}\sum_n e^{i\varphi_n}e^{\frac{ik_0y^2}{2x}\left(1-\frac{k_0}{2xK(x)^2}\right)}\int_{a_n}^{a_{n+1}} e^{-\left[e^{-i\frac{\pi}{4}}K(x)\left(h-\frac{k_0y}{2xK(x)^2}\right)\right]^2}dh\,. \quad (3.41)$$

With $u = e^{-\frac{i\pi}{4}}K(x)(t-\frac{k_0y}{2xK(x)^2})$, the Fresnel integral can be calculated:

$$\widetilde{E} = E_l\sqrt{\frac{k_0}{2\pi xK(x)^2}}\sum_n e^{i\varphi_n}e^{-\frac{ik_0y^2}{2(f-x)}}\int_{e^{-i\frac{\pi}{4}}K(x)(a_n-\frac{k_0y}{2xK(x)^2})}^{e^{-i\frac{\pi}{4}}K(x)(a_{n+1}-\frac{k_0y}{2xK(x)^2})} e^{-u^2}du\,,$$

and the field writes:

$$\widetilde{E} = \frac{E_l}{2}\sqrt{\frac{f}{f-x}}e^{-\frac{ik_0y^2}{2(f-x)}}\sum_n e^{i\varphi_n} \times \left(\mathrm{erf}\left[e^{-\frac{i\pi}{4}}K(x)\cdot(a_{n+1}-\frac{yf}{f-x})\right]-\mathrm{erf}\left[e^{-\frac{i\pi}{4}}K(x)\cdot(a_n-\frac{yf}{f-x})\right]\right). \quad (3.42)$$

Equation (3.42) gives the exact RPP field at any (x, y) point. In the next chapter (see Chapter 6), this formulation makes it possible to specify any RPP field as initial condition for the PIC calculations.

3.2.2 Approximate Random Phase Plate field near the focal spot

The calculation of the wave propagation is based on the field of two crossing beams at the focal spot. It is therefore necessary to know the expression of one beam field in $x = f$ where f is the focal length. Nevertheless, equation (3.42) is not defined in $x = f$. The approximate analytical value of the RPP field around the focal spot can however be found by applying a Taylor expansion of the field around $x = f$. We start from Eq. (3.42): and to express the Taylor expansion, we introduce

$$E_{erf} = \mathrm{erf}\left[e^{-\frac{i\pi}{4}}K(x)\cdot(a_{n+1}-\frac{yf}{f-x})\right]-\mathrm{erf}\left[e^{-\frac{i\pi}{4}}K(x)\cdot(a_n-\frac{yf}{f-x})\right], \quad (3.43)$$

and

$$f_x = \frac{f}{f-x}. \quad (3.44)$$

E_{erf} then recasts as

$$\begin{aligned} E_{erf} &= \mathrm{erf}\left[e^{-\frac{i\pi}{4}}K(x)\cdot(a_{n+1}-yf_x)\right]-\mathrm{erf}\left[e^{-\frac{i\pi}{4}}K(x)\cdot(a_n-yf_x)\right] \\ &= \mathrm{erf}\left[e^{-\frac{i\pi}{4}}\sqrt{\frac{k_0}{2x}}\cdot(a_{n+1}\frac{1}{\sqrt{f_x}}-y\sqrt{f_x})\right]-\mathrm{erf}\left[e^{-\frac{i\pi}{4}}\sqrt{\frac{k_0}{2x}}\cdot(a_n\frac{1}{\sqrt{f_x}}-y\sqrt{f_x})\right]. \end{aligned} \quad (3.45)$$

As $1/\sqrt{(f-x)} \to \infty$, the expression of the function erf(z) behaves as [1]

$$erfc(z) = 1 - erf(z) \underset{z\to\infty}{\sim} \frac{e^{-z^2}}{\sqrt{\pi}z}. \quad (3.46)$$

Equation (3.45) becomes

$$E_{erf} = \frac{-1}{\sqrt{\pi}}\left[\frac{e^{iK(x)^2(a_{n+1}-yf_x)^2}}{e^{-i\pi/4}K(x)(a_{n+1}-yf_x)} - \frac{e^{iK(x)^2(a_n-yf_x)^2}}{e^{-i\pi/4}K(x)(a_n-yf_x)}\right],$$
$$= \frac{-1}{\sqrt{\pi}}\frac{e^{iK(x)^2(a_{n+1}-yf_x)^2}}{e^{-i\pi/4}K(x)(a_{n+1}-yf_x)}\Big(1-e^{iK(x)^2(a_n^2-2a_nyf_x+y^2f_x^2-(a_n^2+2a_nd+d^2)+2(a_n+d)yf_x-y^2f_x^2)}\times\frac{(a_{n+1}-yf_x)}{(a_n-yf_x)}\Big), \tag{3.47}$$

where

$$\frac{(a_{n+1}-yf_x)}{(a_n-yf_x)} \simeq 1, \tag{3.48}$$

which leads to

$$E_{erf} = \frac{-1}{\sqrt{\pi}}\frac{e^{iK(x)^2(a_{n+1}-yf_x)^2}}{e^{-i\pi/4}K(x)(a_{n+1}-yf_x)}\Big(1-e^{-iK(x)^2(2a_nd+d^2-2dyf_x)}\Big),$$
$$= -\frac{1}{\sqrt{\pi}}\frac{e^{iK(x)^2(a_{n+1}-yf_x)^2}}{e^{-i\pi/4}K(x)(a_{n+1}-yf_x)}e^{-iK(x)^2(a_nd+d^2/2-dyf_x)}\Big(2i\sin[K(x)^2(a_nd+d^2/2-dyf_x)]\Big),$$
$$\simeq \frac{2}{\sqrt{\pi}}de^{-i\pi/4}K(x)e^{iK(x)^2\left(a_n^2+2da_n+d^2-2yf_x(a_n+d)+y^2f_x^2-a_nd-d^2/2+dyf_x\right)}\operatorname{sinc}\big(\frac{k_0dy}{2f}+\epsilon\big), \tag{3.49}$$

where $\epsilon = K(x)^2(a_nd+d^2/2) \ll \frac{k_0dy}{2f}$ can be neglected. We used $K(x)^2dyf_x \simeq \frac{k_0dy}{2f}$ when f is close to x. Thus,

$$E_{erf} \simeq \frac{2}{\sqrt{\pi}}de^{-i\pi/4}K(x)e^{iK(x)^2\left((a_n+d/2)^2+d^2/4-dyf_x-2yf_xa_n+y^2f_x^2\right)}\operatorname{sinc}\frac{k_0dy}{2f},$$
$$\implies \widetilde{E} \simeq E_le^{-i\pi/4}\sqrt{\frac{k_0d^2}{2\pi f}}\operatorname{sinc}\frac{k_0dy}{2f}e^{\frac{ik_0y^2}{2x}-i\frac{k_0dy}{2f}}\sum_{n=-N/2}^{N/2}e^{i\varphi_n}e^{iK(x)^2((a_n+d/2)^2-2a_nyf_x)},$$
$$\simeq E_le^{-i\pi/4}\sqrt{\frac{k_0d^2}{2\pi f}}\operatorname{sinc}\frac{k_0dy}{2f}e^{\frac{ik_0y^2}{2x}}\sum_{n=-N/2}^{N/2}e^{i\varphi_n}e^{i\frac{k_0}{2f}\left(\frac{f-x}{x}d^2(n+1/2)^2-2y(n+1/2)\right)d}\Big). \tag{3.50}$$

At this point, 1/2 can be neglected compared to n and the expression becomes

$$\widetilde{E} \simeq E_l e^{-i\pi/4}\sqrt{\frac{k_0 d^2}{2\pi f}}\,\mathrm{sinc}\,\frac{k_0 dy}{2f} e^{\frac{ik_0 y^2}{2f}} \sum_{n=-N/2}^{N/2} e^{i\varphi_n} e^{\frac{ik_0}{2}\left(\frac{d^2 n^2 (f-x)}{f^2} - 2ynd/f\right)}. \tag{3.51}$$

Introducing the variable $\widehat{x} = x - f$ to center the calculation at the focal spot,

$$\widetilde{E} \simeq E_l e^{-i\pi/4}\sqrt{\frac{k_0 d^2}{2\pi f}}\,\mathrm{sinc}\,\frac{k_0 dy}{2f} e^{\frac{ik_0 y^2}{2f}} \sum_{n=-N/2}^{N/2} e^{i\varphi_n} e^{\frac{ik_0}{2}\left(-\frac{d^2 n^2 \widehat{x}}{f^2} - 2ynd/f\right)}. \tag{3.52}$$

Adding the beam propagation $e^{i(k_0\widehat{x} - i\omega_0 t)}$

$$E \simeq e^{-i\omega_0 t} E_l e^{-i\pi/4}\sqrt{\frac{k_0 d^2}{2\pi f}}\,\mathrm{sinc}\,\frac{k_0 dy}{2f} e^{\frac{ik_0 y^2}{2f}} \sum_{n=-N/2}^{N/2} e^{i\varphi_n} e^{ik_0\left(\widehat{x} - \frac{d^2 n^2 \widehat{x}}{2f^2} - ynd/f\right)}, \tag{3.53}$$

and noting

$$\boxed{\theta_n = \frac{nd}{f} \equiv \frac{nD}{(N+1)f}} \tag{3.54}$$

as shown in Fig. 3.4,

$$E \simeq e^{-i\omega_0 t} E_l e^{-i\pi/4}\sqrt{\frac{k_0 d^2}{2\pi f}}\,\mathrm{sinc}\,\frac{k_0 dy}{2f} e^{\frac{ik_0 y^2}{2f}} \sum_{n=-N/2}^{N/2} e^{i\varphi_n} e^{ik_0\left((1-\theta_n^2/2)\widehat{x} + y\theta_n\right)}. \tag{3.55}$$

Then, to second order in $\theta_n \ll 1$, it is convenient to write,

$$E \simeq e^{-i\omega_0 t} E_l e^{-i\pi/4}\sqrt{\frac{k_0 d^2}{2\pi f}}\,\mathrm{sinc}\,\frac{k_0 dy}{2f} e^{\frac{ik_0 y^2}{2f}} \sum_{n=-N/2}^{N/2} e^{i\varphi_n} e^{ik_0\widehat{x}\cos\theta_n + ik_0 y\sin\theta_n}. \tag{3.56}$$

The different phase-shifted beamlets in the sum are focused at the same location, and their interferences lead to the speckle pattern, in the focal spot envelope. The focal spot shape is described by the $\mathrm{sinc}\,\frac{k_0 dy}{2f}$. This will result in an Airy disk which will be visible in our simulations in Chapter 6. To avoid this dispersion and in order to obtain a homogeneous focal spot, common phase plates are built so as to focus the energy in a limited envelope, as

a hypergaussian, out of the scope of the analytical calculations presented here. Turning our attention close to the beam center ($y \ll 1$),

$$E \simeq E_l e^{-i\pi/4} \sqrt{\frac{k_0 D^2}{2\pi f}} \frac{1}{N+1} e^{-i\omega_0 t} \sum_{n=-N/2}^{N/2} e^{i\varphi_n} e^{ik_0 \cos\theta_n \widehat{x} + ik_0 \sin\theta_n y} \,. \tag{3.57}$$

This expression is equivalent to a beam constructed by the addition of slightly tilted plane waves around the mean k_0 [93], with random phases, leading to a finite speckle size. Equation (3.57) allows to calculate the field of each beam at the focal spot, from which it will be possible to deduce the crossing field.

Introducing the f number, $f_\# = f/D$, the perpendicular component of the wave number of each plane wave is

$$\boxed{k_n^\perp = \frac{k_0 n}{(N+1) f_\#} \,,} \tag{3.58}$$

with the maximum value, written here for $N+1 \simeq N \gg 1$,

$$\boxed{k_{max} = \frac{k_0 D}{2f} \equiv \frac{k_0}{2f_\#} \,,} \tag{3.59}$$

In the limit $\theta_{k^\perp} \ll 1$, $\cos\theta_{k^\perp} \simeq 1$ and $\sin\theta_{k^\perp} \simeq \theta_{k^\perp}$ and Eq. (3.57) becomes the well known formula [94]:

$$E = E_0 e^{ik_0 \widehat{x} - i\omega_0 t} \frac{1}{N+1} \sum_{k^\perp=-k_{max}}^{k_{max}} e^{i\varphi_{k^\perp}} e^{ik^\perp y} \,, \tag{3.60}$$

where we introduced $E_0 = E_l e^{-i\pi/4} \sqrt{k_0 D^2/2\pi f}$. Figure 3.3 (from Ref. [94]) exhibits the speckles intensity statistic. The dashed curve is the statistic in the Gaussian limit, the plain curve is the statistic of intense hot spots, and the intensity histogram is plotted by finding the local maxima of E^2 (E being defined in Eq. (3.60), and in Eq. (1) and (5) in Ref. [94]) in many realizations of E. For $N \gg 1$, Fig. 3.3 shows that Eq. (3.60) is found to reproduce the speckles intensity statistic.

Moreover, from now the vector potential A is used instead of E. This comes from our choice to derive the beam propagation equations as well as the forthcoming wave mixing equations with the potential vector, in order to have the conservation of the transverse canonical momentum.

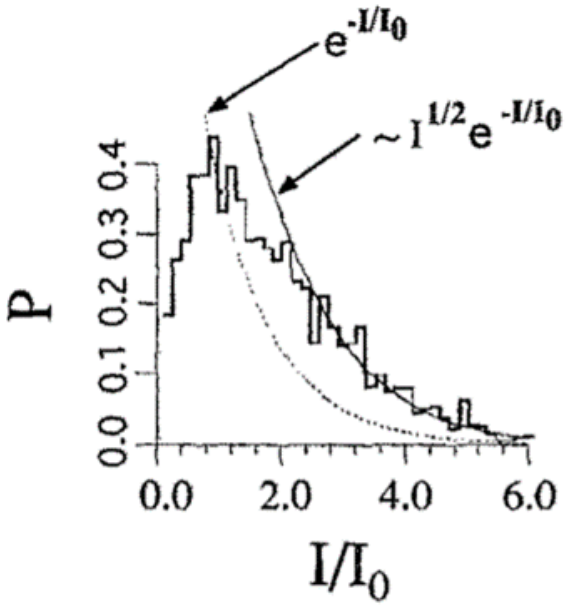

Figure 3.3: Numerically determined histogram of hot spot intensities as derived in [94], deduced from the probability distribution of Eq. (3.60). About 3000 hot spots in about 100 realizations of the phase ensemble were sampled to construct the histogram.

Equation (3.57) therefore becomes

$$A = ae^{-i\omega_0 t}\frac{1}{N+1}\sum_{n=-N/2}^{N/2} e^{i\varphi_n}e^{ik_0\cos\theta_n\widehat{x}+ik_0\sin\theta_n y}\,, \tag{3.61}$$

and Eq. (3.60) becomes

$$A = ae^{ik_0\widehat{x}-i\omega_0 t}\frac{1}{N+1}\sum_{k^\perp=-k_{max}}^{k_{max}} e^{i\varphi_{k^\perp}}e^{ik^\perp y}\,, \tag{3.62}$$

with $a = E_0/(-i\omega_0)$. For a beam propagating in any direction $\boldsymbol{r}$, this expression can be generalized in

$$A = ae^{i\boldsymbol{k_0}\cdot\boldsymbol{r}-i\omega_0 t}\frac{1}{N+1}\sum_{k^\perp=-k_{max}}^{k_{max}} e^{i\varphi_{k^\perp}}e^{i\boldsymbol{k}^\perp\cdot\boldsymbol{r}}\,. \tag{3.63}$$

Both expressions will be used in Chapter 6 to resolve the wave equation. However, Eq. (3.61) sums up different $k_x = k_0 \cos\theta_n x$ components whereas Eq. (3.63) only adds up plane waves with equal $k_x = k_0$ components. Even though the random phase shift between the beamlets is taken into account, Eq. (3.63) leads to infinite longitudinal speckles. This amounts to neglecting the diffraction of the beamlets near focus. In the following, we will refer to this situation as the case **without diffraction**. Conversely, we will refer to the field of Eq. (3.61) as the case **with diffraction**. To illustrate the difference between the speckles shape with and

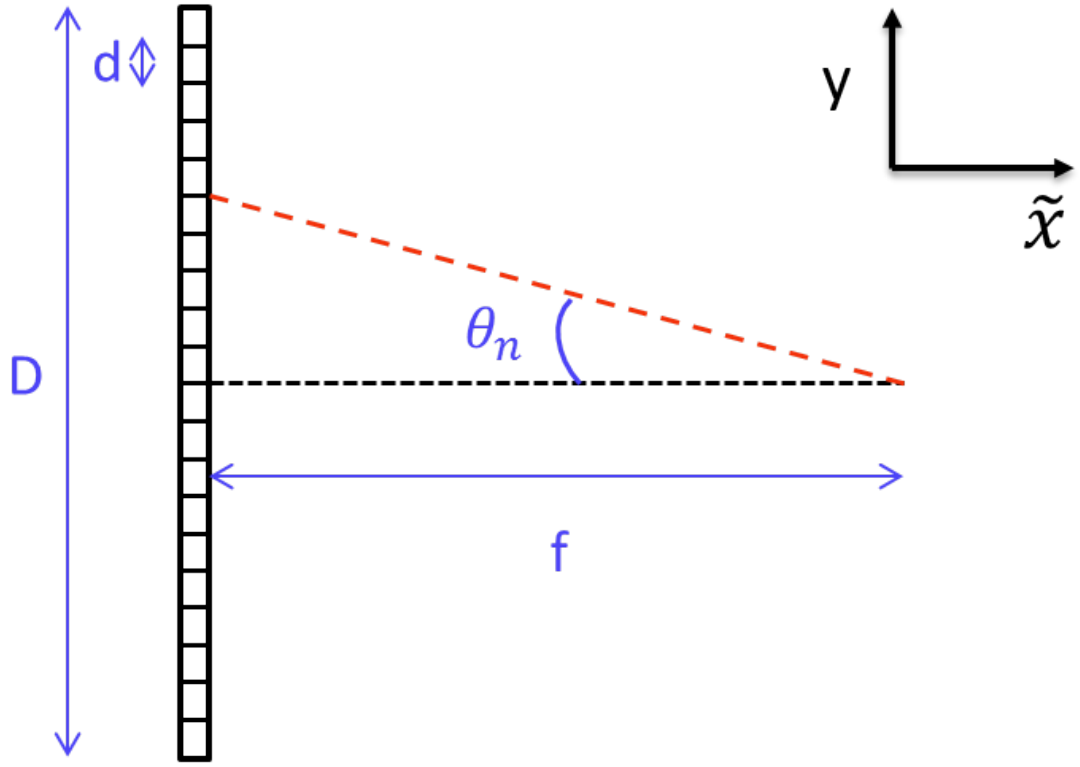

Figure 3.4: Scheme of the phase plate and the focal geometry

without diffraction, Fig. 3.5 exhibits the beam intensity for N=6, 40 or 100. For the case N=6, the y axis is $6 \times 2\pi N f_{\#}$ long which corresponds to six patterns. In this way, the periodicity is visible. As the beam dimension is infinite, the same pattern is reproduced. For the case N=40 and N=100, only one pattern is plotted to allow a clear distinction of the speckles. Theses figures allow to see the number of speckles evolving with the phase plate number, as well as the shape of the speckles. Without diffraction, speckles are straight and infinite, although they have finite and different sizes in the case with diffraction. For the CBET calculation, the exchange depends on the crossing zone sizes which is mainly determined by the transverse speckle's size.

Unless the beams are nearly parallel, the size of the crossing zone does not depend on the longitudinal speckle's size so the diffraction can be neglected. This statement will be proven in Section 6.1. However, it does have an important impact when the instability grows along the speckle's direction, as for forward SBS.

3.3 Speckles characteristics

The speckles, plotted in Fig. 3.5, have specific sizes that can be estimated with the spatial autocorrelation function of the E-field. While the calculation of the transverse size can be made with or without considering diffraction, the calculation of the longitudinal size is made accounting for the diffraction. Indeed, only the expression with diffraction allows to obtain a finite longitudinal speckle size. For a better readability, the calculation is made with the simplified equation on A, considering Eq. (3.63) to calculate the transverse size and Eq. (3.61) for the longitudinal size.

3.3.1 Calculation of the transverse speckles size

Let us introduce the random normalized variable G_N defined by

$$G_N = \frac{\sum_{n=-N/2}^{N/2} g_n e^{i\varphi_n}}{[\sum_{n=-N/2}^{N/2} |g_n|^2]^{1/2}}\,, \tag{3.64}$$

where

$$g_n = a e^{k_0 x - i\omega_0 t} \frac{1}{N+1} e^{ik^\perp y}\,, \tag{3.65}$$

and we recall that $k^\perp = k_0 n/(N+1) f_\#$ so the sum can be expressed either on n or on $k^\perp$. For a large number of elements, $N \to \infty$, the random variable G_N converges to the normal law, of mean value $\mathbb{E}[G_N] = 0$ and variance $\mathbb{E}[|G_N|^2] = 1$ (where $\mathbb{E}[X]$ is the expectation value of X.). The autocorrelation Γ function writes

$$\Gamma(y, y') = \mathbb{E}\left[\big(G(y) \times G^\star(y')\big)\right]. \tag{3.66}$$

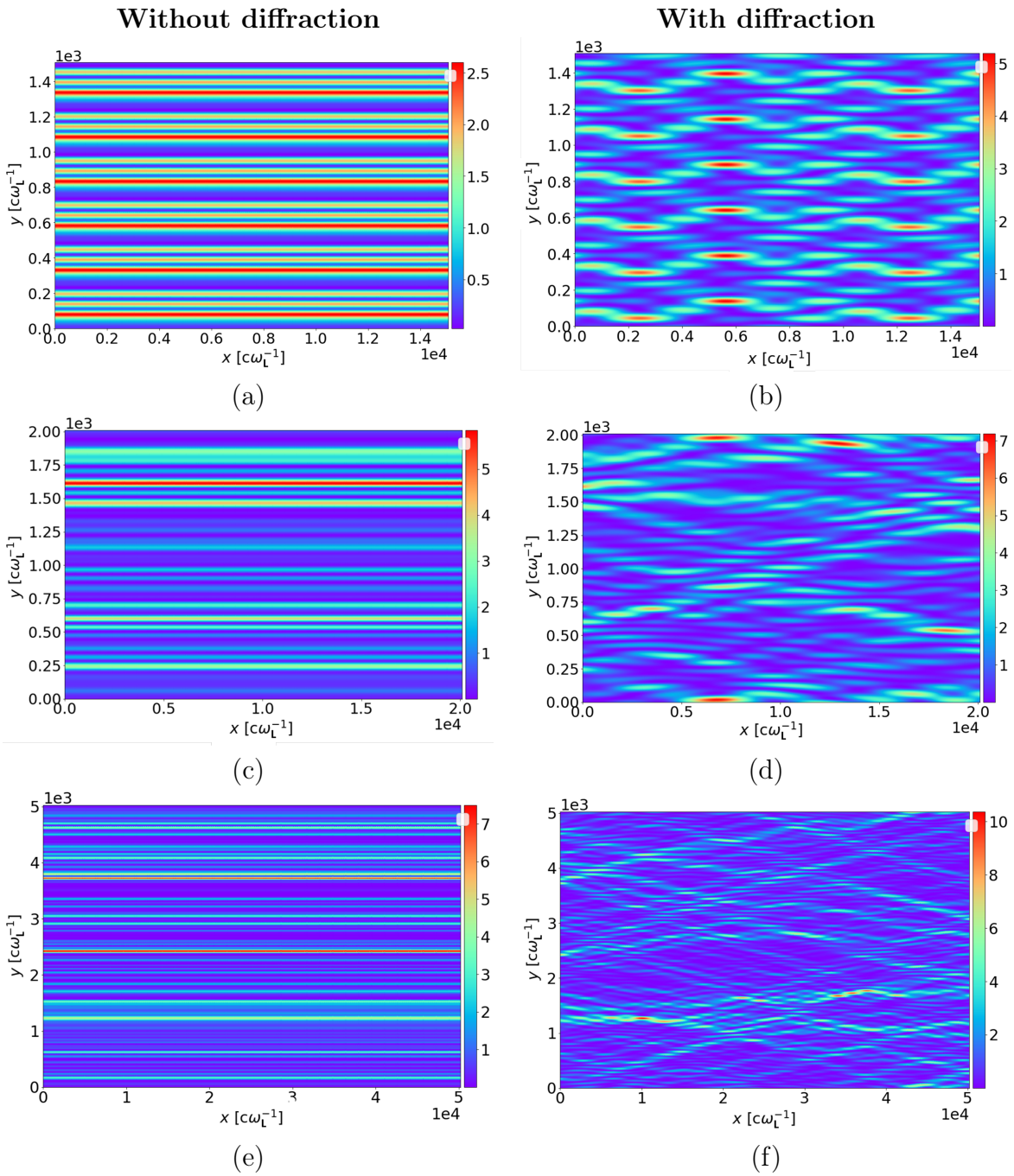

Figure 3.5: Intensity maps of a RPP beam focal spot normalized to the averaged intensity (left) without diffraction (right) with diffraction, (up) N = 6, five patterns are plotted, (middle) N = 40, one pattern is plotted, (down) N=100, one pattern is plotted. The periodicity corresponds to $L = 2\pi N f_{\#}$ where $f_{\#} = 8$.

Introducing

$$I = \langle |A|^2 \rangle \,, \tag{3.67}$$

$$= \sum_{n=-N/2}^{N/2} |g_n|^2 \,, \tag{3.68}$$

$$= \frac{a^2}{N+1} \,, \tag{3.69}$$

the autocorrelation function recasts as

$$\Gamma(y, y') = \frac{1}{I^{1/2}} \frac{1}{I'^{1/2}} \sum_{n=-N/2}^{N/2} \sum_{n'=-N/2}^{N/2} g_n(y) g_{n'}^{\star}(y') \, \mathbb{E}\left[e^{i(\varphi_n - \varphi_{n'})}\right] . \tag{3.70}$$

Developing the expression and noting that $\mathbb{E}\left[e^{i(\varphi_n - \varphi_{n'})}\right] = \delta_{n-n'}$ where δ is the Kronecker delta,

$$\Gamma(y, y') = \frac{1}{N+1} \sum_{n=-N/2}^{N/2} \sum_{n'=-N/2}^{N/2} \delta_{n-n'} e^{-i\frac{k_0 d}{f}[yn - y'n']} \,, \tag{3.71}$$

$$= \frac{1}{N+1} \sum_{n=-N/2}^{N/2} e^{-i\frac{k_0 n d}{f}[y - y']} \,. \tag{3.72}$$

For a large number of elements ($N \to \infty$), the sum converges to an integral and the autocorrelation function becomes

$$\Gamma(y, y') = \operatorname{sinc} \frac{N k_0 d}{2f}(y - y') = \operatorname{sinc} \frac{k_0}{2 f_{\#}}(y - y') \,. \tag{3.73}$$

This result reveals the sinus cardinal shape of the speckle. The radius of the speckle is defined as the first zero of $\Gamma(y, y')$ and leads to $\rho_{sp} = f_{\#} \lambda_0$ [32], with $\lambda_0 = 2\pi / k_0$, which also corresponds to the waist at $2/\pi$ of the maximum. In Fig. 3.5 with $f_{\#} = 8$, the speckle width is $2\pi f_{\#} \simeq 50$.

3.3.2 Calculation of the longitudinal speckles size

Here the same method is applied for the calculation of the autocorrelation function $\Gamma(x, x')$ and starting from Eq. (3.61). Here,

$$g_n = ae^{-i\omega_0 t}\frac{1}{N+1}e^{ik_0\cos\theta_n x + ik_0\sin\theta_n y}\,. \tag{3.74}$$

I is still equal to $a^2/(N+1)^2$. The autocorrelation function

$$\Gamma(x, x') = \mathbb{E}\left[\left(G(x)\times G^\star(x')\right)\right], \tag{3.75}$$

leads to

$$\Gamma(x, x') = \frac{1}{N+1}\sum_{n=-N/2}^{N/2}\sum_{n'=-N/2}^{N/2}\delta_{n,n'}e^{ik_0\left[\cos\theta_n x - \cos\theta_{n'}x' + \sin\theta_n y - \sin\theta_{n'}y\right]}\,, \tag{3.76}$$

$$= \frac{1}{N+1}\sum_{n=-N/2}^{N/2}e^{-ik_0\cos\theta_n(x'-x)}\,. \tag{3.77}$$

Considering $\theta_n << 1$ we can use the first order Taylor expansion $\cos\theta_n \simeq 1-\theta_n^2/2$ and obtain

$$\Gamma(x, x') = e^{-ik_0(x'-x)}\frac{1}{N+1}\sum_{n=-N/2}^{N/2}e^{ik_0\frac{\theta_n^2}{2}(x'-x)}\,. \tag{3.78}$$

For a large number of elements ($N\to\infty$), the previous sum converges to an integral, and after some algebra becomes

$$\Gamma(x, x') = \sqrt{\pi}e^{i\pi/4}\sqrt{\frac{2f_\#^2}{k_0(x'-x)}}e^{-ik_0(x'-x)}\mathrm{erf}\left[e^{-i\pi/4}\frac{1}{2}\sqrt{\frac{k_0(x'-x)}{2f_\#^2}}\right]. \tag{3.79}$$

This expression does not cancel out. The longitudinal correlation length is therefore defined as the the half-width of $|\Gamma(x, x')|$, leading to a correlation length of $\sim 10f_\#^2\lambda_0$ which is similar to the value found in Refs. [32, 10]. For $f_\# = 8$, the speckle length is $\simeq 4000$. This value also coincides with the Fig. 3.5 (bottom right, for large N).

In this chapter, the equations of the beam propagation after a phase plate have been established. The expression of the fields found here will be used, together with the wave mixing equations of Chapter 4, to derive the wave equation and the energy exchange produced by two RPP beams in Chapter 6.

Chapter 4

Cross-Beam Energy Transfer equations

Contents

This chapter presents the usual calculations of CBET which will be used as starting point for Chapter 5. First, the well-known Landau damping value in the linear kinetic regime is recalled in Section 4.1.1 in order to be added as a phenomenological correction in the wave mixing calculation in Section 4.2. Then, the different wave propagation equations are presented. As an illustration, this system, describing the energy exchange, is solved in the case of two Gaussian beams in Section 4.3.

4.1 Wave damping

This section is in SI to allow an easier comparison with the literature.

4.1.1 Landau Damping

The Landau Damping denotes the non-collisional damping of electrostatic waves in a plasma. When a particle velocity is close to the phase velocity of a wave, an energy exchange occurs between the particle and the wave. If the particles whose initial velocity is slightly smaller than the wave phase velocity, the particles are globally accelerated with the wave energy. Conversely, if the particles whose velocity is higher than the wave phase velocity, the particles are globally decelerated and loses energy. In the case of a Maxwellian particle velocity distribution, there is more particles with a smaller velocity than particles with a higher velocity that interact with the wave, as shown in Fig. 4.1.

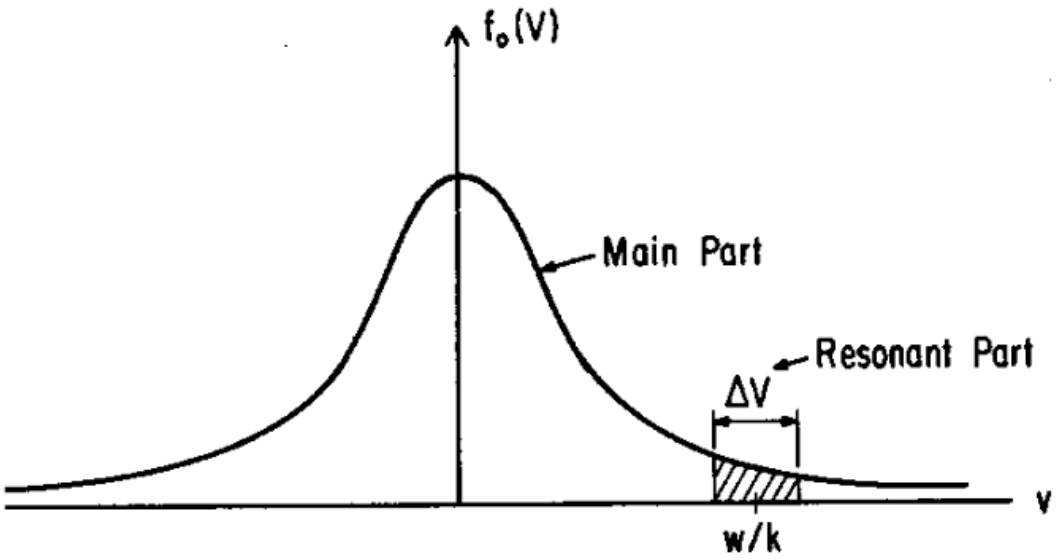

Figure 4.1: Division of the distribution function between a resonant and a non-resonant (main) part. From [81]

The latter is therefore damped. The damping can be derived from the linearized Vlasov (Eq. (2.1)) and Poisson equations, writing $f_\alpha(\boldsymbol{r}, \boldsymbol{v}, t) = f_{\alpha,0}(\boldsymbol{v}) + f_{1\alpha,}(\boldsymbol{r}, \boldsymbol{v}, t)$. At first order and choosing $\boldsymbol{E}$ along the y direction, these equations become

$$\partial_t f_1 + v\partial_y f_1 + \frac{q}{m} E \cdot \partial_v f_0 = 0\,, \tag{4.1}$$

and

$$\partial_y E = \frac{e}{\epsilon_0}(n_{i,1} - n_{e,1})\,, \tag{4.2}$$

which corresponds to Gauss law. This system can be resolved as an initial value problem as described in [46]. The response to an initial perturbation is composed of normal modes given by the dispersion equation:

$$\varepsilon(\omega, k) = 1 + \sum_\alpha \chi_\alpha(\omega, k) = 0\,. \tag{4.3}$$

where the susceptibility for the species α is:

$$\chi_\alpha(k, \omega) = \frac{q_\alpha^2}{m_\alpha \epsilon_0 k^2} \int d^3v \frac{\nabla_v f_{\alpha,0}}{\omega/k - v}\,, \tag{4.4}$$

where the integration contour lies above the pole $\omega/k = v$.

Considering Maxwellian distribution functions for $f_{\alpha,0}$ as initial conditions

$$f_{\alpha,0}(v) = \frac{n_{\alpha,0}}{\sqrt{2\pi}v_{th\alpha}} e^{-v^2/2v_{th\alpha}^2} . \tag{4.5}$$

where $v_{th\alpha}$ is the thermal velocity of the species α, we obtain

$$\chi_\alpha(\omega, k) = -\frac{\omega_{p\alpha}^2}{2k^2 v_{th\alpha}^2} \mathcal{Z}' \left(\frac{\omega}{\sqrt{2}kv_{th\alpha}} \right) , \tag{4.6}$$

where $\mathcal{Z}$ is the Fried and Conte's plasma dispersion function [28], $\omega_{pe} = \sqrt{e^2 n_e / m_e \varepsilon_0}$ is the electron plasma frequency and $\omega_{pi} = \sqrt{Z^2 e^2 n_i / m_i \varepsilon_0}$ is the ion plasma frequency. Resolving the real part of Eq. (4.3) allows to find the IAW and EPW dispersion relations. Under appropriate limits, the latter coincide with the fluid theory (Eqs. (2.16) and (2.19)). The damping effect cannot be caught by a fluid theory.

A solution to the dispersion relation Eq. (4.3) can be numerically found by plotting the value of $v_\varphi = \mathrm{Re}\{\omega/k\}$ and $\nu/k = \mathrm{Im}\{\omega/k\}$ for which the real and the imaginary part of ε is zero [29, 117] under the approximation $k^2 v_{the}^2/\omega_{pe}^2 \ll |\mathcal{Z}'(\omega/kv_{the})| \sim 2$. Multiple solutions correspond to both $\mathrm{Im}\{\varepsilon\} = 0$ and $\mathrm{Re}\{\varepsilon\} = 0$, each one of these solutions corresponds to an eigenmode of acoustic wave propagation. The one to be considered here is the least damped (purple arrow), as shown in Fig. 4.2.

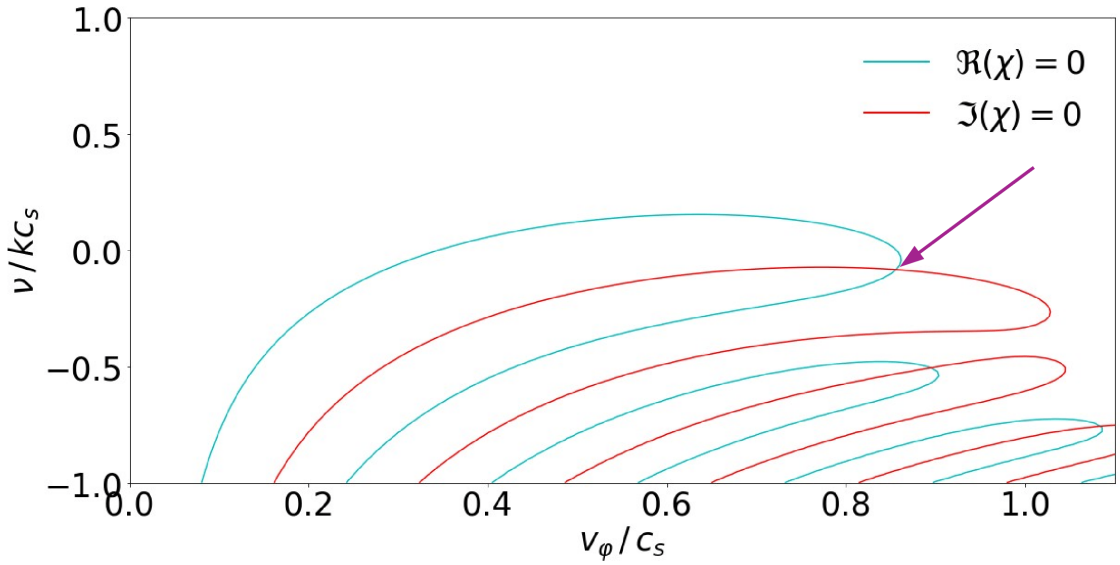

Figure 4.2: Plot of the solutions of $\mathrm{Im}\{\epsilon\} = 0$ and $\mathrm{Re}\{\epsilon\} = 0$ in the limit $k^2 v_{the}^2/\omega_{pe}^2 \ll 1$

versus v_φ/c_s and ν/kc_s. The purple arrow shows the solution considered. Here, a CH plasma is considered, with $T_i = 1\,\mathrm{keV}$ and $T_e = 2\,\mathrm{keV}$ and c_s is the acoustic velocity calculated with the mean A (=6.5) and Z(=3.5).

For a weak damping, we can write $\omega = kv_\varphi + i\nu$ where $\nu \ll \omega$. A Taylor expansion of ε thus gives

$$\varepsilon(kv_\varphi + i\nu, k) \simeq \varepsilon(kv_\varphi, k) + i\nu\partial_\omega\varepsilon(kv_\varphi, k) = 0\,, \tag{4.7}$$

where

$$\partial_\omega\chi_\alpha(kv_\varphi, k) = -\frac{\omega_{p\alpha}^2}{2^{3/2}k^3 v_{th\alpha}^3}\mathcal{Z}''\left(\frac{v_\varphi}{\sqrt{2}v_{th\alpha}}\right)\,. \tag{4.8}$$

Finally, considering $k^2 v_{the}^2/\omega_{pe}^2 \ll 1$,

$$\nu = k \times \mathrm{Im}\left\{\frac{\sum_{\alpha_i}\frac{\omega_{pi}^2}{v_{th\alpha_i}^2}\mathcal{Z}'(\frac{v_\varphi}{\sqrt{2}v_{thi}}) + \frac{\omega_{pe}^2}{v_{the}^2}\mathcal{Z}'(\frac{v_\varphi}{\sqrt{2}v_{the}})}{\sum_{\alpha_i}\frac{\omega_{pi}^2}{\sqrt{2}v_{th\alpha_i}^3}\mathcal{Z}''(\frac{v_\varphi}{\sqrt{2}v_{thi}}) + \frac{\omega_{pe}^2}{\sqrt{2}v_{the}^3}\mathcal{Z}''(\frac{v_\varphi}{\sqrt{2}v_{the}})}\right\}, \tag{4.9}$$

where α_i denotes the ion species. For a single ion species, this formula gives satisfying results compared to the numerical resolution of (4.6). Nevertheless, the value of v_φ is not

straightforward for multi species ions, and this expression yields erroneous values when calculating c_s with the ion mean values of Z and A. For a single species ion and $ZT_e/T_i \gg 1$, an analytical solution is found with $v_\varphi = c_s$

$$\frac{\nu}{kc_s} = \sqrt{\frac{\pi}{8}}\left[\frac{\omega_{pi}}{\omega_{pe}} + \frac{c_s^3}{v_{thi}^3} e^{-c_s^2/2v_{thi}^2}\right], \tag{4.10}$$

where

$$c_s = \sqrt{\frac{Zk_BT_e + 3T_i}{m_i}}\,. \tag{4.11}$$

4.1.2 Additional collisional damping

Albeit weak, the collisional damping of ion acoustic waves depends both on e-i and i-i collision rate [9, 23, 8] and can be comparable or even higher than the Landau damping rate for a high Z plasma such as gold. The electron-ion mean-free path is defined as (in S.I. units)

$$\lambda_{e,i} = \frac{3k_B^2T_e^2(4\pi\varepsilon_0)^2}{4\sqrt{2\pi}n_eZe^4\ln\Lambda}\,, \tag{4.12}$$

where $\ln\Lambda = \ln\lambda_D/p_0$ is called the Coulomb logarithm and the impact factor p_0 corresponds to a $\pi/2$ diffusion of an electron by an ion. The ion-ion mean free path is

$$\lambda_{i,i} = \frac{3k_B^2T_i^2(4\pi\varepsilon_0)^2}{4\sqrt{\pi}n_iZ^4e^4\ln\Lambda}\,. \tag{4.13}$$

Estimation of the IAW damping rates including both Landau and collisional damping can be deduced from Fig. 4.3. After the calculation of $\lambda_{e,i}$ and $\lambda_{i,i}$ with Eq. (4.12) and (4.13), we can evaluate the damping rate by finding the corresponding $k\lambda_{e,i}$ and $k\lambda_{i,i}$ values on both figures. The simulations of the left curves (electron-ion) are made with the code SPRING which solves Fokker-Planck and cold-ion fluid equations. The damping rate γ account for both Landau and electron-ion collisional damping ($\gamma = \gamma_{Landau+ei}$). Note that the parameter β is a scaling factor chosen so that most curves are merged for the weak damping. The right panel shows analytical fluid calculations of the ion-ion damping (plain curves) compared to Fokker-Planck simulations (points). The damping rate γ corresponds to the sum of the Landau and the ion-ion collisional damping ($\gamma = \gamma_{Landau} + \gamma_{ii}$). In Chapters 5 and 6, the maximum collisional damping rate is

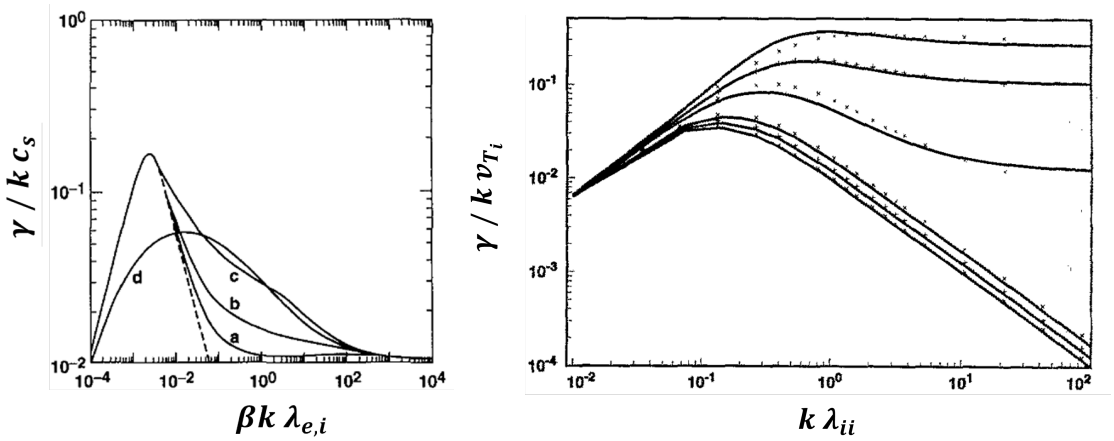

Figure 4.3: (left) normalised damping rate accounting for electron-ion collision from [23], β is a scaling factor (β = 0.24, 0.68, 0.2, and 1 for Z = 1, 8, 64, and ∞ respectively.) The dashed curve is the fluid result and the solid curves represent simulations with Z = 1 (a), 8 (b), 64 (c), ∞ (d). (right) normalised damping rate accounting for ion-ion collision from [9] The six solid curves are analytically calculated for the temperature ratios ZT_e/T_i of 4, 8, 16, 48, 64, 80 (top to bottom). For comparison, the points are the numerical results of Ref. [91] for the ratios 4, 8 and 16, and of Ref. [111] for the ratios 48, 64 and 80.

estimated by taking the greater value between γ_{ei} and γ_{ii}. For high Z plasmas such as gold, the electron-ion collisional damping rate is comparable to the Landau damping rate, and the ion-ion collisional damping rate remains negligible. For moderate Z such as CH or Carbon plasmas, collisions become negligible. This will be verified in Chapter 6.

4.2 Wave mixing

In this section, we go back to PIC normalized expressions.

4.2.1 Ponderomotive force for two crossing laser beams

The expression of the ponderomotive force is

$$F_p = \frac{1}{2}\langle \partial_y \mathrm{Re}\Big\{\widetilde{A}e^{iS(\boldsymbol{r},t)}\Big\}^2\rangle_T\,, \tag{4.14}$$

where $T = 2\pi/\omega_0$ is a laser period and $S(\boldsymbol{r},t) = i\boldsymbol{k}\cdot\boldsymbol{r} - i\omega t$. Writing

$$\mathrm{Re}\Big\{\widetilde{A}e^{iS(\boldsymbol{r},t)}\Big\} = \frac{1}{2}(\widetilde{A}e^{iS(\boldsymbol{r},t)} + \widetilde{A}^{\star}e^{-iS(\boldsymbol{r},t)})\,, \tag{4.15}$$

the calculation of the ponderomotive force for $A = A_0 + A_1$ leads to

$$\begin{aligned}
F_p &= \frac{1}{2}\langle\partial_y\big(\,\mathrm{Re}\Big\{\widetilde{A_0}e^{iS_0(\boldsymbol{r},t)}\Big\} + \mathrm{Re}\Big\{\widetilde{A_1}e^{iS_1(\boldsymbol{r},t)}\Big\}\big)^2\rangle_T\,,\\
&= \frac{1}{8}\langle\partial_y\big(\widetilde{A_0}e^{iS_0(\boldsymbol{r},t)} + \widetilde{A_0}^{\star}e^{-iS_0(\boldsymbol{r},t)} + \widetilde{A_1}e^{iS_1(\boldsymbol{r},t)} + \widetilde{A_1}^{\star}e^{-iS_1(\boldsymbol{r},t)}\big)^2\rangle_T\,,\\
&= \frac{1}{8}\langle\partial_y\big(\widetilde{A}_0^2e^{2iS_0(\boldsymbol{r},t)} + \widetilde{A}_1^2e^{2iS_1(\boldsymbol{r},t)} + \widetilde{A}_0^{\star 2}e^{-2iS_0(\boldsymbol{r},t)} + \widetilde{A}_1^{\star 2}e^{-2iS_1(\boldsymbol{r},t)}\\
&+ 2\big[\widetilde{A}_0\widetilde{A}_1e^{iS_0(\boldsymbol{r},t)+iS_1(\boldsymbol{r},t)} + \widetilde{A}_0^{\star}\widetilde{A}_1^{\star}e^{-iS_0(\boldsymbol{r},t)-iS_1(\boldsymbol{r},t)} + \widetilde{A}_0\widetilde{A}_1^{\star}e^{iS_0(\boldsymbol{r},t)-iS_1(\boldsymbol{r},t)}\\
&+ \widetilde{A}_0^{\star}\widetilde{A}_1e^{-iS_0(\boldsymbol{r},t)+iS_1(\boldsymbol{r},t)} + \widetilde{A}_0\widetilde{A}_0^{\star} + \widetilde{A}_1\widetilde{A}_1^{\star}\big]\big)\rangle_T\,.
\end{aligned} \tag{4.16}$$

Where $S_0(\boldsymbol{r},t) = \boldsymbol{k}_0\cdot\boldsymbol{r} - i\omega_0 t$, $S_1(\boldsymbol{r},t) = \boldsymbol{k}_1\cdot\boldsymbol{r} - i\omega_1 t$ and $S(\boldsymbol{r},t) = S_0(\boldsymbol{r},t) - S_1(\boldsymbol{r},t)$. Terms with phases equal to $\pm 2S_0(\boldsymbol{r},t)$, $\pm 2S_1(\boldsymbol{r},t)$, $\pm(S_0(\boldsymbol{r},t) + S_1(\boldsymbol{r},t))$ oscillate at $\simeq 2\omega_0$ and their average value over T is therefore zero. Other terms being slowly variable over T, their average value is equal to their value at time t. It remains

$$F_p = \frac{1}{4}\partial_y\big(\widetilde{A_0}\widetilde{A_0}^{\star} + \widetilde{A_1}\widetilde{A_1}^{\star} + \widetilde{A_0}\widetilde{A_1}^{\star}e^{iS(\boldsymbol{r},t)} + \widetilde{A_0}^{\star}\widetilde{A_1}e^{-iS(\boldsymbol{r},t)}\big)\,. \tag{4.17}$$

In the following, we neglect $\partial_y\widetilde{A_0}\widetilde{A_0}^{\star}$, $\partial_y\widetilde{A_1}\widetilde{A_1}^{\star}$ and $\partial_y\widetilde{A_0}\widetilde{A_1}^{\star}$ in front of $\partial_y S(\boldsymbol{r},t)$, keeping only the beating terms,

$$F_p = \frac{1}{4}\partial_y\big(\widetilde{A_0}\widetilde{A_1}^{\star}e^{iS(\boldsymbol{r},t)} + c.c.\big) \implies \partial_y F_p = -\frac{k^2}{4}\big(\widetilde{A_0}\widetilde{A_1}^{\star}e^{iS(\boldsymbol{r},t)} + c.c.\big)\,. \tag{4.18}$$

4.2.2 Damped acoustic wave equation

We introduce the notation $\delta N_{e,i}^R$ to denote the value of $\delta N_{e,i}$ in the real space, and to contrast with its imaginary value used for the calculations of Section 4.3. Starting from Eq. (2.8) for a

wave propagating along y, we use the expansions

$$n_i = n_{i,0} + \delta N_i^R \,, \tag{4.19}$$

$$v_i = v_d + \delta v_i \,. \tag{4.20}$$

To alleviate the algebra, a stationary plasma with $v_d = 0$ is considered, and the perturbed continuity equation is obtained

$$\partial_t \delta N_i^R + n_{i,0} \partial_y \delta v_i = 0 \,. \tag{4.21}$$

Then, writing the normalized motion equation for electrons and ion

$$m_i \partial_t \delta v_i = ZE - \frac{\partial_y P_i}{n_{i,0}} \,, \tag{4.22}$$

$$\partial_t v_e = -E - \frac{\partial_y P_e}{n_{e,0}} + F_p \,, \tag{4.23}$$

and considering $n_e = Z n_i$ and and neglecting the electrons inertia,

$$m_i \partial_t \delta v_i = -\frac{\partial_y P_i}{n_{i,0}} - Z \frac{\partial_y P_e}{n_{e,0}} + Z F_p. \tag{4.24}$$

In the adiabatic limit for ions ($P_i = 3 n_i T_i$) and isothermal for electrons ($P_e = n_e T_e$)

$$\partial_t \delta v_i = -c_s^2 \frac{\partial_y \delta N_i^R}{n_{i,0}} + \frac{Z F_p}{m_i} \,, \tag{4.25}$$

where $c_s = \sqrt{(Z T_e + 3 T_i)/m_i}$ is the ion acoustic velocity. Differentiating Eq. (4.25) with respect to y and using Eq. (4.21), $\partial_y F_p$ appears in the equations and we can use Eq. (4.18) which yields:

$$\partial_t^2 \delta N_i^R - c_s^2 \partial_y^2 \delta N_i^R = -\frac{Z n_{i,0} |\boldsymbol{k}|^2}{4 m_i} \left(\widetilde{A_0} \widetilde{A_1}^\star e^{iS(\boldsymbol{r},t)} + c.c. \right) . \tag{4.26}$$

Then, the damping is added as a phenomenological correction, where ν is evaluated as explained in 4.1.1 and the damped IAW is obtained

$$[\partial_t^2 + 2\nu\partial_t - c_s^2\partial_y^2]\delta N_e^R = -\frac{Zn_{e,0}|\boldsymbol{k}|^2}{4m_i}\widetilde{A}_0\widetilde{A}_1^\star e^{i\boldsymbol{k}\cdot\boldsymbol{r}-i\omega t} + c.c.\,, \tag{4.27}$$

As the diffusion of photons is due to electrons, the choice has been made to recast the equation with $\delta N_e = Z\delta N_i$ instead of δN_i. Noting $\delta N_e = \frac{1}{2}\delta\widetilde{N}_e e^{i\boldsymbol{k}\cdot\boldsymbol{r}-i\omega t}$ the (imaginary) component of δN_e^R with the phase $i\boldsymbol{k}\cdot\boldsymbol{r} - i\omega t$ allows to identify terms with the same phase, and Eq. (4.27) becomes (in the imaginary space)

$$[\partial_t^2 + 2\nu\partial_t - c_s^2\partial_y^2]\delta N_e = -\frac{Zn_{e,0}|\boldsymbol{k}|^2}{2m_i}\widetilde{A}_0\widetilde{A}_1^\star e^{i\boldsymbol{k}\cdot\boldsymbol{r}-i\omega t}.\,, \tag{4.28}$$

4.2.3 Laser envelopes coupling equation

Now that the damped wave equation is set, we establish the envelopes coupling equations, required for the energy exchange calculation in the two following Chapters 5 and 6. The starting point has been explained in 3.1.1 and consists in resolving Maxwell equation with a slowly varying envelope field. Thus, starting from Eq. (3.20)

$$\Delta\boldsymbol{A} - \partial_t^2\boldsymbol{A} = n_e\boldsymbol{A}\,,$$

and noting the vector potentials of the laser fields as: $\mathbf{A} \approx \frac{1}{2}\sum_{j=0}^{1}\widetilde{\boldsymbol{A_j}}e^{i\mathbf{k}_j\cdot\mathbf{r}-i\omega_j t} + c.c.$, Eq. (3.20) becomes

$$n_e\mathbf{A} = \sum_{j=0}^{1} e^{i\mathbf{k}_j\cdot\mathbf{r}-i\omega_j t}(\Delta\widetilde{\boldsymbol{A_j}} - \widetilde{\boldsymbol{A_j}}k_j^2 + 2i\boldsymbol{k}_j\cdot\boldsymbol{\nabla}\widetilde{\boldsymbol{A_j}} + \omega_j^2\widetilde{\boldsymbol{A_j}} + 2i\omega_j\partial_t\widetilde{\boldsymbol{A_j}} - \partial_t^2\widetilde{\boldsymbol{A_j}}) + c.c.\,, \tag{4.29}$$

neglecting the second order terms, considering the slow varying envelope approximation, the stationary regime, $n_e = n_{e,0} + \frac{1}{2}(\delta\widetilde{N}_e e^{i\boldsymbol{k}\cdot\boldsymbol{r}-i\omega t} + \delta\widetilde{N}_e^\star e^{-i\boldsymbol{k}\cdot\boldsymbol{r}-i\omega t})$ where $\delta\widetilde{N}_e^\star$ denotes the complex conjugate of $\delta\widetilde{N}_e$, and the dispersion equation $(\omega_i^2 - k_i^2) = n_{e0}$ it remains:

$$[\delta\widetilde{N}_e e^{i\boldsymbol{k}\cdot\boldsymbol{r}-i\omega t} + \delta\widetilde{N}_e^\star e^{-i\boldsymbol{k}\cdot\boldsymbol{r}-i\omega t}](\widetilde{\boldsymbol{A_0}}e^{i(\boldsymbol{k}_0\cdot\boldsymbol{r}-\omega_0 t)} + \widetilde{\boldsymbol{A_1}}e^{i(\boldsymbol{k}_1\cdot\boldsymbol{r}-\omega_1 t)} + c.c.) =$$
$$4i(\boldsymbol{k}_0\cdot\boldsymbol{\nabla}\widetilde{\boldsymbol{A_0}}e^{i(\boldsymbol{k}_0\cdot\boldsymbol{r}-\omega_0 t)} + \boldsymbol{k}_1\cdot\boldsymbol{\nabla}\widetilde{\boldsymbol{A_1}}e^{i(\boldsymbol{k}_1\cdot\boldsymbol{r}-\omega_1 t)}) + c.c.\,. \tag{4.30}$$

After the identification of the terms with the same phase, the coupling equations on the laser envelopes $\widetilde{\boldsymbol{A_i}}$, finally write:

$$4i\boldsymbol{k_0}\cdot\boldsymbol{\nabla}\widetilde{\boldsymbol{A_0}} = \delta\widetilde{N}_e\,\widetilde{\boldsymbol{A_1}}\,, \tag{4.31}$$

$$4i\boldsymbol{k_1}\cdot\boldsymbol{\nabla}\widetilde{\boldsymbol{A_1}} = \delta\widetilde{N}_e^{\star}\,\widetilde{\boldsymbol{A_0}}\,. \tag{4.32}$$

4.3 Cross-Beam Energy Transfer between two Gaussian Beams

The simplest CBET configuration is the crossing of two plane waves. These plane waves can be either considered as idealized laser beams or as two isolated speckles. To calculate the energy exchange in this configuration, we first recall the model, presented in [18], of two Gaussian beams crossing each other in a homogeneous plasma with a half-angle θ. The polarisation of the lasers is perpendicular to the crossing plane.

4.3.1 Wave propagation

Compared to Ref. [18], we consider a plasma with a drift velocity v_d where $v_d = \boldsymbol{v_d}\cdot\hat{\boldsymbol{y}}$ is < 0 as $\boldsymbol{v_d}$ is chosen in a direction opposed to $\boldsymbol{k}$. This way, the exchange goes in the same direction whether considering $v_d = 0$, $\omega > 0$ or $\omega = 0$, $v_d < 0$. Equation (4.28) with a plasma flow writes

$$[(\partial_t + v_d\partial_y)^2 + 2\nu(\partial_t + v_d\partial_y) - c_s^2\partial_y^2]\delta N_e = -\frac{Zn_{e,0}|\boldsymbol{k}|^2}{2m_i}\widetilde{A_0}.\widetilde{A_1}^{\star}e^{ik.y-i\omega t}\,, \tag{4.33}$$

where we remind that δN_e is a complex. This equation can either be found by following the perturbative procedure around $v_i = v_d + \delta v_i$ as explained in Sec. 4.2.2 or by applying a Galilean transform of Eq. (4.27) from the plasma reference frame to the lab frame. Assuming the beam waist is large compared to the characteristic Landau damping distance, $[\nabla a_{0,1}/a_{0,1}]^{-1} \gg c_s/\nu$, where $\widetilde{A_0}\widetilde{A_1}^{\star} = a_0 a_1^{\star}$. In the limit where $\widetilde{A_0}.\widetilde{A_1}^{\star}$ is constant, equation (4.33) can be solved in Fourier space. Then, by returning to the real space, we can deduce an expression of δN_e.

Let us apply the FT of Eq. (4.33) $\overline{f} = \int_{-\infty}^{+\infty} f(y) e^{-i\overline{k}y} dy$, assuming a simple r.h.s of the form: $a_0 a_1^\star = \beta e^{iky - i\omega t}$.

$$\left[(\partial_t + i\overline{k}v_d)^2 + 2\nu(\partial_t + i\overline{k}v_d) + \overline{k}^2 c_s^2\right] \delta\overline{N}_e = \beta\pi e^{-i\omega t}\delta(\overline{k} - k)\,. \tag{4.34}$$

$\delta\overline{N}_e = 0$ and $\partial_t \delta\overline{N}_e = 0$ being the initial conditions at t = 0, the solution is:

$$\delta\overline{N}_e = \frac{\beta\pi\delta(\overline{k} - k)}{-(\omega - \overline{k}v_d)^2 - 2i\nu(\omega - \overline{k}v_d) + c_s^2\overline{k}^2}$$

$$\times \left(e^{-i\omega t} + \frac{i\omega + \lambda(\overline{k})_-}{\lambda(\overline{k})_+ - \lambda(\overline{k})_-} e^{\lambda(\overline{k})_+ t} - \frac{i\omega + \lambda(\overline{k})_+}{\lambda(\overline{k})_+ - \lambda(\overline{k})_-} e^{\lambda(\overline{k})_- t} \right), \tag{4.35}$$

where

$$\lambda_\pm(k) = -\nu - ikv_d \pm i\sqrt{c_s^2 k^2 - \nu^2}\,. \tag{4.36}$$

The inverse FT gives $\delta N_e = \beta f(y, t, k, \omega)$ with

$$f(y, t, k, \omega) = \frac{e^{iky}}{-(\omega - kv_d)^2 - 2i\nu(\omega - kv_d) + c_s^2 k^2}$$

$$\times \left(e^{-i\omega t} + \frac{i\omega + \lambda_-}{\lambda_+ - \lambda_-} e^{\lambda_+ t} - \frac{i\omega + \lambda_+}{\lambda_+ - \lambda_-} e^{\lambda_- t} \right). \tag{4.37}$$

We obtain:

$$\delta N_e(y, x, z, t) \approx -\frac{Z n_{e,0} |\boldsymbol{k}|^2}{2m_i} f(y, t, k, \omega) a_0 . a_1^\star\,. \tag{4.38}$$

The IAW is the sum of three waves corresponding to the three terms in the rightmost parenthesis of Eq. (4.37), one driven wave ($\propto e^{iky - i\omega t}$) and two damped waves, moving in opposite directions, whose amplitudes vary according to the proximity to the resonance. When the asymptotic regime is reached, only the driven wave remains ($e^{\lambda(k)_\pm t} \xrightarrow[t\to\infty]{} 0$) and writes:

$$\delta N_e^{driven} = 2\alpha \widetilde{f}(k,\omega) e^{iky - i\omega t}\,, \tag{4.39}$$

where

$$\boxed{\widetilde{f}(k,\omega) = \frac{1}{c_s^2 k^2 - (\omega - k v_d)^2 - 2i\nu(\omega - k v_d)}\,,} \tag{4.40}$$

where $\widetilde{f}(k,\omega)$ is the driven acoustic wave envelope and

$$\alpha = -\frac{Z n_{e,0} |\boldsymbol{k}|^2}{4 m_i} a_0 . a_1^\star\,. \tag{4.41}$$

This asymptotic solution is used in most of linear models.

4.3.2 Exchange calculation

Introducing the intensities $I_{0,1} = |a_{0,1}|^2$, $\alpha_I(t) = \frac{Z n_{e,0} |\boldsymbol{k}|^2}{2 m_i} \mathrm{Im}[f(t)]$, and the change of variables $Y_0 = \cos\theta y + \sin\theta x$ and $Y_1 = -\cos\theta y + \sin\theta x$ where θ is the half-angle between the beams, the wave coupling equations (4.31) and (4.32) simplify to

$$\partial_{Y_1} I_0 = -\alpha_I(t) I_0 I_1\,, \tag{4.42}$$

$$\partial_{Y_0} I_1 = \alpha_I(t) I_0 I_1\,. \tag{4.43}$$

The resolution of the system [61] leads to

$$I_0 = f_0 \frac{e^{[-P_0^0]}}{e^{[P_1^0]} + e^{[-P_0^0]} - 1}\,, \tag{4.44}$$

$$I_1 = f_1 \frac{e^{[P_1^0]}}{e^{[P_1^0]} + e^{[-P_0^0]} - 1}\,, \tag{4.45}$$

where

$$P_0^0 = \frac{\alpha_I(t)}{\sin 2\theta} \int_{-\infty}^{Y_0} f_0 dY_0'\,, \tag{4.46}$$

$$P_1^0 = \frac{\alpha_I(t)}{\sin 2\theta} \int_{-\infty}^{Y_1} f_1 dY_1'\,, \tag{4.47}$$

$f_{0,1}$ are the initial conditions,

$$f_{0,1} = I^0_{0,1} e^{-\frac{Y^2_{0,1}+x^2}{w^2_{0,1}}}, \tag{4.48}$$

and $w_{0,1}$ is the waist of the beam 0,1. Thus, the exchange direction is determined by the sign of Im$[f(t)]$. With $\theta_f(t)$ the phase shift between the IAW and the grating, it comes Im$[f(t)] \propto \sin\theta_f(t)$. From this it can be deduced that a negative phase shift leads to a transfer of energy from high to low frequencies and vice versa.

The IAW propagation and the energy exchange for two plane waves has been established. The same resolution method will be used for more complex situations in Chapter 5 and in Chapter 6.

Chapter 5

Effect of the phase-shift between successive speckle crossings

Contents

Laser beams used in ICF experiments are spatially smoothed with phase plates, described in Section 2.3. Their resulting intensity pattern is composed of a multitude of speckles. Thus, two crossing beams are equivalent to numerous crossing speckles and CBET occurs at each of these crossings. In this chapter, we focus on the exchange due to the wavelength shift between the beams and we consider a stationnary plasma. If the grating velocity is equal to the ion acoustic velocity c_s, the density modulation induced by the ponderomotive force propagates, leading to an IAW moving in the grating direction. In a weakly Landau-damped plasma, the IAW created at a crossing can reach another crossing without being damped, thus affecting the exchange. It is therefore required to distinguish cases where the gratings are in-phase, and out-of-phase. The latter case, more realistic according to the randomness of speckles distribution, induces a significant drop down of the exchange rate compared to the in-phase case. However, in most hydrodynamic models, this speckle structure is not taken into account and may explain the difficulties to reproduce the experimental results. The lacks in CBET modeling had been identified in Section 2.4.2, and reproducing the experimental results is often achieved by artificially saturating the density perturbation [47, 39]. This chapter aims at demonstrating that neglecting the inhomogeneities in the laser intensity would usually lead to an overestimate of the energy exchange. This chapter is organized as follows. Section 5.1 presents a CBET linear model including a random phase shift between the speckles. Section 5.2 presents 2D PIC simulations of CBET occurring between eight speckles in a weakly-damped plasma. The phase between the speckles has been varied so as to observe the destructive ion acoustic wave interference on the energy exchange.

5.1 Cross-Beam Energy Transfer model

In the first physical situation, we investigate the field at focal spot resulting from the crossing of two smoothed laser beams is modeled by a sinusoidal envelop. Doing so, we impose equal size and amplitude for each crossing envelope. Even though a realistic model is introduced in the next chapter, this simplified model allows to control more laser parameters and therefore explore the speckles structure influence. Typically, this model allows to choose the phase shift between two successive SCs which is the purpose of the section.

5.1.1 Wave propagation

In the laboratory referential, the crossing envelope is defined as $\widetilde{A}_0\widetilde{A}_1^\star = \frac{a_0 a_1^\star}{2}(\cos k_{sp}y + 1)$. In this chapter, the focus is on the difference between the wavelength shift case with and without phase shift so $v_d = 0$. It is still left in the equations for the consistency of notations in the manuscript. The maximum amplitude is 1 and the crossings are represented by successive sinusoidal envelopes as shown in Fig. 5.1 (a). The wave equation, defined in Eq. (4.33), in this case writes

$$[(\partial_t + v_d\partial_y)^2 + 2\nu(\partial_t + v_d\partial_y) - c_s^2\partial_y^2]\delta N_e = \alpha(\cos k_{sp}y + 1)e^{i(ky-\omega t)}\,, \tag{5.1}$$

where we recall α from Eq. (4.41): $\alpha = -\frac{Zn_{e,0}|\boldsymbol{k}|^2}{4m_i}a_0.a_1^\star$. The sinusoidal envelope implies that all the gratings are following each other, they are therefore in phase. As a consequence, the IAW created in one crossing will interact without phase shift with the IAW created in the next crossing. In a realistic situation, the distance between crossings may vary depending on the phase plate elements as well as the grating phase. It is very unlikely that two IAWs interact in phase. The phase shift between IAW and the resulting destructing interference is one of the speckles structure element that can modify the exchange. To take the phase shift into consideration, a sinusoidal phase change $\Phi(y)$ along the y direction is introduced. Thereby, the r.h.s. term of Eq. (4.33) is multiplied by

$$\boxed{\Phi(y) = e^{i\pi\sin\beta y} = \sum_{n\in\mathbb{Z}} J_n(\pi)e^{in\beta y}\,,} \tag{5.2}$$

where J_n is the Bessel function of the first kind,

$$J_n(\pi) = \sum_{p\in\mathbb{N}} \frac{(-1)^p}{(n+p)!p!}\left(\frac{\pi}{2}\right)^{2p+n}. \tag{5.3}$$

$\widetilde{A}_0\widetilde{A}_1^\star$ thus becomes $\widetilde{A}_0\widetilde{A}_1^\star = \frac{a_0 a_1^\star}{2}(\cos k_{sp}y + 1)\Phi(y)$. By varying the parameter β between 0 and $k_{sp}/12$, $\phi = \pi\sin\beta y$ varies from 0 to $\pi/2$ in one period λ_{sp}. Note that with realistic smoothed laser beams, the maximum phase shift between two SCs can reach π. Yet, owing to the continuous phase change approximation of Eq. (5.2), the maximum phase shift was fixed to $\pi/2$ to avoid a significant phase change along one SC. As a result, our model will probably

underestimate the phase shift effect on CBET.

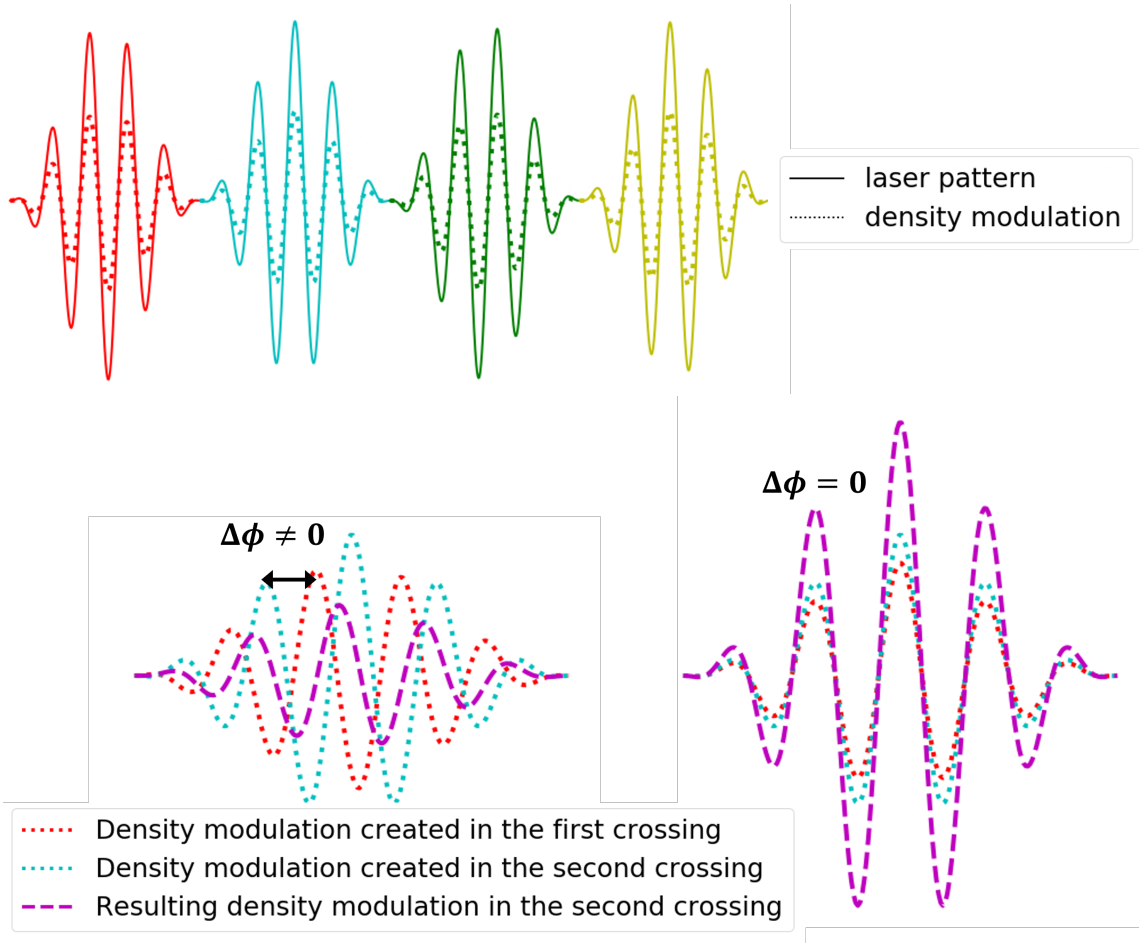

Figure 5.1: Crossing section geometry at $L_x/2$. (top) At t=0 the laser pattern (plain line) creates a density modulation (dotted line) with its corresponding phase ϕ. Each colour represent one SC. (bottom) Example of the wave from the red pattern (partially damped after its propagation) reaching the blue one at $t = \lambda_{sp}/c_s$. The magenta dashed line is the resulting amplitude of the waves interaction. The phase-shift case is represented (left) and the final amplitude results from the partially destructive interference of the waves. In the in-phase case (right), the interference is constructive and the final wave amplitude is bigger.

To illustrate our model, Fig. 5.1 (top) represents four crossings and therefore four IAWs which are going to interfer with the next crossing. We recall that the phase $\phi_i = \pi \sin \beta y$ is continuously varying, but the variation is small enough to consider that the phase is the same in one SC. Then, Fig. 5.1 (bottom) illustrates the interaction when the IAW has reached the next crossing area. The wave issued from the red pattern is represented after a propagating

distance of λ_{sp}, when reaching the blue pattern. Its amplitude is smaller due to its damping after the propagation. The interaction between both waves is destructive when considering a phase shift between the wave, and constructive when considering no phase shift.

Writing the wave equation 5.1 with the phase shift term leads to

$$\left[(\partial_t + v_d\partial_y)^2 + 2\nu(\partial_t + v_d\partial_y) - c_s^2\partial_y^2\right]\delta N_e = \alpha(\cos k_{sp}y + 1)e^{i(ky-\omega t)}\sum_{n\in\mathbb{Z}} J_n(\pi)e^{in\beta y}\,. \quad (5.4)$$

By linearity of Eq. (4.34), any linear combination, at the r.h.s., of the form $\beta_1 e^{ik_1 y - i\omega_1 t} + \beta_2 e^{ik_2 y - i\omega_2 t}$, is also solution, with $\delta N_e = \beta_1 f(y,t,k_1,\omega_1) + \beta_2 f(y,t,k_2,\omega_2)$. Applying a decomposition of $\frac{1}{2}(\cos k_{sp}y + 1)e^{iky-i\omega t}$ into three terms:

$$\delta N_e = \alpha\sum_{n\in\mathbb{Z}} J_n(\pi) \times \left[f(k+n\beta) + \frac{f(k+k_{sp}+n\beta)}{2} + \frac{f(k-k_{sp}+n\beta)}{2}\right], \quad (5.5)$$

where the dependencies on y, t and ω have not been written to simplify the notation, and f has been defined in Eq. (4.37). The solution of Eq. (5.5) is found using the decomposition into an infinite set of waves. At long times, the remaining wave results from the beating between the many driven waves,

$$\begin{aligned}\delta N_e^{driven} = {} & \alpha e^{iky-i\omega t}\sum_{n\in\mathbb{Z}} J_n(\pi)e^{in\beta y} \\ & \times \left[\widetilde{f}(k+n\beta) + \frac{1}{2}\widetilde{f}(k+k_{sp}+n\beta)e^{ik_{sp}y} + \frac{1}{2}\widetilde{f}(k-k_{sp}+n\beta)e^{-ik_{sp}y}\right], \end{aligned} \quad (5.6)$$

where $\widetilde{f}$ is defined in eq. (4.40) and the wave envelope,

$$\delta\widetilde{N}_e^{driven} = \delta N_e^{driven} e^{-(iky-i\omega t)}\,, \quad (5.7)$$

is

$$\delta\widetilde{N}_e^{driven} = \alpha \sum_{n\in\mathbb{Z}} J_n(\pi) e^{in\beta y} \Big[\widetilde{f}(k+n\beta) + \frac{1}{2}\widetilde{f}(k+k_{sp}+n\beta) e^{ik_{sp}y} + \frac{1}{2}\widetilde{f}(k-k_{sp}+n\beta) e^{-ik_{sp}y} \Big] \tag{5.8}$$

At resonance $\omega = kc_s$,

$$\begin{aligned}\delta\widetilde{N}_e^{driven} = \alpha \sum_{n\in\mathbb{Z}} J_n(\pi) e^{in\beta y} \times \Big[& \frac{1}{-2i\nu k c_s + 2c_s^2 kn\beta + c_s^2 n^2\beta^2} \\ & + \frac{e^{ik_{sp}y}}{2\times(-2i\nu k c_s + 2kc_s^2(n\beta+k_{sp}) + c_s^2(n\beta+k_{sp})^2)} \\ & + \frac{e^{-ik_{sp}y}}{2\times(-2i\nu k c_s + 2kc_s^2(n\beta-k_{sp}) + c_s^2(n\beta-k_{sp})^2)} \Big], \end{aligned} \tag{5.9}$$

The resonance between the IAW and the crossing envelope induces a beating between k and k_{sp} preventing the resonance of ω/k with c_s. Hence, the bracket term in Eq. (5.9) is smaller than $\widetilde{f}$ at resonance ($= 1/2i\nu k c_s$) that is to say smaller than the plane wave case. The effect of the phase shift between the speckles further decreases the IAW amplitude compared to the plane wave case.

5.1.2 Exchange calculation

The role of the beating waves on the energy exchange can be analysed perturbatively. The wave coupling described by the system of Eqs. (4.31)-(4.32), can be simplified by introducing $\widetilde{A}_0 = \widetilde{A}_0^0 + \delta\widetilde{A}_0$ and $\widetilde{A}_1 = \widetilde{A}_1^0 + \delta\widetilde{A}_1$ and rewrites, to leading order in $\delta\widetilde{A}_{0/1}$,

$$4i\boldsymbol{k_0}\cdot\boldsymbol{\nabla}\delta\widetilde{A}_0 = \delta\widetilde{N}_e\,\widetilde{A}_1^0\,, \tag{5.10}$$

$$4i\boldsymbol{k_1}\cdot\boldsymbol{\nabla}\delta\widetilde{A}_1 = \delta\widetilde{N}_e^\star\,\widetilde{A}_0^0\,. \tag{5.11}$$

Introducing $I_{0,1} = |\widetilde{A}_{0,1}|^2$ and $\delta I_{0,1} = \widetilde{A}_{0,1}\delta\widetilde{A}_{0,1}^\star + c.c.$, the previous set of equations recasts as:

$$\boldsymbol{k_0}\boldsymbol{\nabla}\delta I_0 = \frac{1}{2}\,\mathrm{Im}\left[\delta\widetilde{N}_e\widetilde{A}_1^0\widetilde{A}_0^{0\star}\right], \tag{5.12}$$

In the asymptotic limit ($t \to \infty$), only the driven waves remain and $\delta\widetilde{N}_e^{driven} = \delta N_e^{driven} e^{-i\boldsymbol{k}\cdot\boldsymbol{r}+i\omega t}$ leads to:

$$\boldsymbol{k_0}\boldsymbol{\nabla}\delta I_0 = \gamma I_0^0 I_1^0 = \frac{1}{2}\,\mathrm{Im}\left[\delta\widetilde{N}_e^{driven}\widetilde{A}_1^0\widetilde{A}_0^{0\star}\right]. \tag{5.13}$$

As $\mathbf{k}_0 \cdot \nabla = k_0\cos\theta\partial_x + k_0\sin\theta\partial_y$ and δI_0 only depends on y it comes

$$k_0\sin\theta\int d_y\delta I_0 dy = \frac{1}{2}\int \mathrm{Im}\left[\delta\widetilde{N}_e^{driven}\widetilde{A}_1^0\widetilde{A}_0^{0\star}\right]. \tag{5.14}$$

The calculation of Eq. (5.14) over a length $L = N\lambda_{sp}$ leads to:

$$\begin{aligned} k_0\sin\theta\int_{-N\lambda_{sp}/2}^{N\lambda_{sp}/2} d_y\delta I_0 dy = \mathrm{Im}\Bigg\{\frac{\alpha a_0^\star a_1}{2}\int_{-N\lambda_{sp}/2}^{N\lambda_{sp}/2} dy\sum_{n\in\mathbb{Z}} J_n(\pi)e^{in\beta y}\Big(1+\frac{1}{2}e^{ik_{sp}y}-\frac{1}{2}e^{-ik_{sp}y}\Big) \\ \times\Big[\widetilde{f}(k+n\beta)+\frac{1}{2}\widetilde{f}(k+k_{sp}+n\beta)e^{ik_{sp}y}+\frac{1}{2}\widetilde{f}(k-k_{sp}+n\beta)e^{-ik_{sp}y}\Big]\Bigg\}, \end{aligned} \tag{5.15}$$

where N is chosen large enough to compute an exchange including numerous different phase shifts. The product between the terms into brackets and the terms into parenthesis is reduced to only three terms, and it remains:

$$\begin{aligned} k_0\sin\theta\delta I_0 &= \mathrm{Im}\Bigg\{\frac{\alpha a_0^\star a_1}{2}\sum_{n\in\mathbb{Z}} J_n(\pi)\int_{-N\lambda_{sp}/2}^{N\lambda_{sp}/2} dy\Big[\widetilde{f}(k+n\beta)+\frac{1}{4}\widetilde{f}(k+k_{sp}+n\beta)+\frac{1}{4}\widetilde{f}(k-k_{sp}+n\beta)\Big]\Bigg\}, \\ &= \mathrm{Im}\Bigg\{\frac{\alpha a_0^\star a_1 N\lambda_{sp}}{2}\sum_{n\in\mathbb{Z}} J_n(\pi)\times\Big[\widetilde{f}(k+n\beta)+\frac{1}{4}\widetilde{f}(k+k_{sp}+n\beta)+\frac{1}{4}\widetilde{f}(k-k_{sp}+n\beta)\Big]\Bigg\}, \end{aligned} \tag{5.16}$$

which describes the exchange over the distance $N\lambda_{sp}$. The normalized exchange after a characteristic propagation length of $\lambda_{sp}/\sin\theta$ (corresponding to one SC) writes:

$$\frac{\delta I_0}{I_0} = \frac{\lambda_{sp}\alpha_1}{k_0\sin\theta}\,\mathrm{Im}\Bigg\{\sum_{n\in\mathbb{Z}} J_n(\pi)\times\Big[\widetilde{f}(k+n\beta)+\frac{1}{4}\widetilde{f}(k+k_{sp}+n\beta)+\frac{1}{4}\widetilde{f}(k-k_{sp}+n\beta)\Big]\Bigg\}, \tag{5.17}$$

where we defined

$$\boxed{\alpha_1 = -\frac{Zn_{e,0}k^2}{4\tilde{m}_i}a_1 a_1^\star.} \tag{5.18}$$

The solution can also be written

$$\delta I_0 = \frac{\lambda_{sp}}{k_0 \sin\theta} \langle \gamma I_0^0 I_1^0 \rangle_{y,\phi} \,, \tag{5.19}$$

where $\langle\,\rangle_{y,\phi}$ is the mean value along y (and along β for the phase shift case. The in-phase case corresponds to $\phi = 0$ so $\beta = 0$.) This equation describes the energy exchange between the two beams in the perturbation limit. The phase change effect on the energy exchange can be explored by comparing the value of $\delta I_0/I_0$ for different phase shifts. The dependence of $\delta I_0/I_0$ on the Landau damping rate is shown in Fig. 5.2 (top). The model does not account for the laser depletion, thus explaining the unrealistic values $\delta I_0/I_0 > 1$. First, the plane wave case (black solid line) corresponds to the higher energy gain. Then, the intensity gain has been calculated at resonance with or without phase shifts, in a stationary plasma. The latter has also been estimated by performing an average over 200 phase shifts between two successive SCs, ranging from 0 to $\pi/2$, generated with β ranging from 0 to $k_{sp}/12$ (red dashed line). The purpose of this averaging is to estimate the exchange rate for a weakly Landau-damped wave that can cross several SCs and thus *see* a few different phase shifts. When all SCs are in-phase (orange solid line), the energy exchange in the weakly-damped regime is reduced by 30% compared to the plane wave case. Due to the constructive interferences of the IAWs, the in-phase case is an upper bound of the energy exchange compared to the out-phase cases. In the worst scenario (limited to $\Delta\phi = \pi/2$ in our model), the intensity gain is reduced by a factor ~ 6 compared to the in-phase case, and the maximum of the exchange value is not located at the smallest damping value. Because the phase shift diminishes the amplitude of the IAW owing to the destructive interference, a long damping distance ($\nu \ll 1$) reduces the exchange compared to the ideal plane wave case [85]. The averaged phase shift case (red dashed line), demonstrates a reduction by 65 % of the CBET. In the limit of large damping rates (here $\nu > 0.1\,kc_s$ for $k_{sp} = 0.3k$), the effect of the phase shift between SCs becomes negligible. Indeed, in a strongly-damped regime, the IAWs are driven by the interference pattern located at one SC. The asymptotic amplitude is thus roughly linked to the local field, averaged over a damping distance. In a spectral point of view, the IAWs are not resonantly driven according to Eq. (5.9). Yet, this asymptotic limit also depends on the ratio between the damping distance and the interspeckle one, $\nu/k_{sp}c_s$. Figure 5.2 (bottom) shows the ratio between the averaged phase shift case and the in-phase case at resonance (corresponding respectively to the red dashed line and the solid dark orange line of the (top) pannel), at asymptotic time, versus the distance between SC, for three different species. When $k_{sp} \ll k$, the envelope is infinite so no phase-shit effect exists. For a larger value of k_{sp} (or smaller speckles), the SC are closer so the

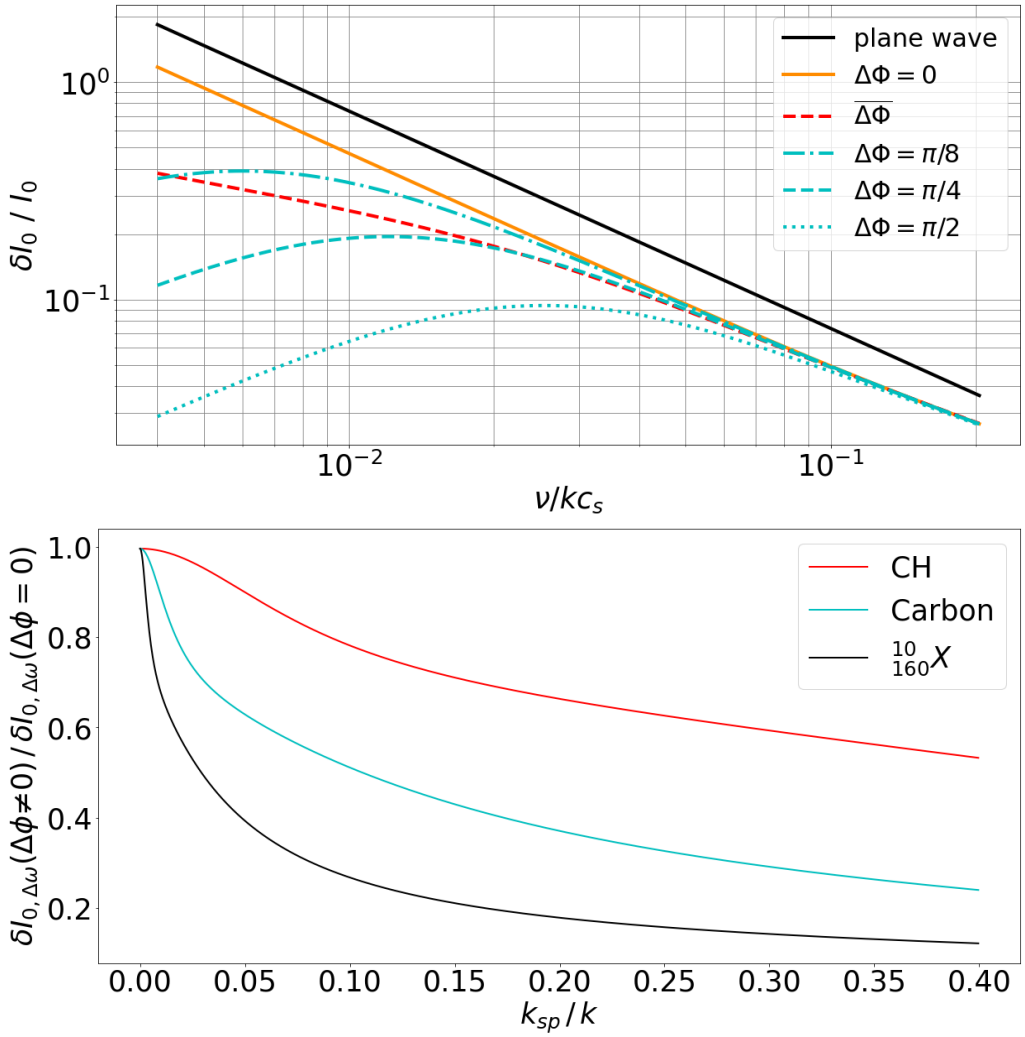

Figure 5.2: (top)log-log plots of $\delta I_0/I_0$ for the plane wave, the in-phase and phase shifted speckles cases versus the ratio between the speckle length and the Landau damping length, at resonance $\omega = kc_s$. The out-of-phase case, $\delta I_0/I_0$ for $\overline{\Delta\phi}$, is a double averaging along y and for a phase varying from 0 to $\pi/2$ in one period λ_{sp}. The latter average was performed along β generated with β ranging from 0 to $k_{sp}/12$. The parameters are $k_{sp} = 0.3\,k$ with ν varying between $0.0041\,\omega$ and $0.2\,\omega$. (bottom) Ratio of $\delta I_0/I_0$ between the wavelength shift case with averaged phase shift and the wavelength shift case without phase shift versus k_{sp}/k. The plasma Z=10 A=160 corresponds to the plasma parameters of this section. The carbon (C) and plastic (CH) plasma parameters are similar to those of the PIC simulations described in the next section.

IAWs undergo more phase-shits. This effect is even more important as the damping is weak because the number of crossed SC increases. In conclusion, Fig. 5.2 shows that the difference

between the cases with and without phase shift depends on both the damping distance and the inter-speckles distance.

5.2 Cross-Beam Energy Transfer simulations

5.2.1 Parameters

In this section we present Calder PIC simulations [56], on simple physics configurations, in order to illustrate the influence of the speckle phase differences on the resulting energy exchange. Furthermore, these linear models neglect ion trapping and heating due to collisions.

Numerical parameters

The box size is $L_x \times L_y = 8000 \times 3200\, c^2\, \omega_L^{-2}$, with a mesh size of $0.44 \times 0.44\, c^2\, \omega_L^{-2}$, so as to be close to the Debye length. Cells are filled by 20 macro-ions and 20 macro-electrons. The time step is $0.3\, \omega_L^{-1}$. Boundary conditions are reflective for the plasma and absorbing for the fields. A 4th-order alternating interpolation scheme [103] has been used together with a high mode current filtering.

Plasma parameters

The simulations are performed in a homogeneous and non collisional plasma. The electron density is equal to $0.04\, n_c$ where n_c is the critical density. The other plasma parameters have been chosen so as to obtain a long Landau-damping distance, covering several SCs. For the Landau damping rate, the expression

$$\nu = \sqrt{\pi}|k|c_s^4 \left[\frac{e^{-c_s^2 m_i/2T_i}}{(2T_i/m_i)^{3/2}} + \frac{m_i}{Z(2T_e)^{3/2}} \right], \tag{5.20}$$

can be used for a single ion species, as explained in 4.1.1. With $c_s = \sqrt{(ZT_e + 3T_i)/m_i}$, this expression shows that a weakly-damped IAW is characterized by $c_s/v_{T_i} \gg 1$, corresponding to $ZT_e \gg T_i$. This typical situation corresponds to a gold plasma in ICF condition where the ionization state is $Z^\star \approx 50$, $A = 197$, $T_e \sim 4{-}5$ keV and $T_i \sim 1{-}2$ keV [114, 71] although other hohlraum materials have been studied [83, 25, 72]. Alas, the numerical heating which varies as

Z^2, imposes us to use a smaller Z. The plasma is composed of ion with $A = 160$, $Z = 10$, and ion and electron temperatures of $T_i = 1\,\text{keV}$ and $T_e = 4\,\text{keV}$, respectively. Moreover, 3 filters have been applied to smooth the current deposited by the macro-particles [113] to completely eliminate the heating. The damping characteristic distance is $c_s/\nu = 646\,c\,\omega_L^{-1}$ ($\sim$100 μm for a wavelength of $1\,\mu$m), a value much larger than the typical distance between the SCs. Landau damping distances estimates based on the electronic and ionic temperatures from different studies [79, 119] provide values between $225\,c\,\omega_L^{-1}$ and $500\,c\,\omega_L^{-1}$. It is worth pointing out that collisions have been neglected to avoid the plasma heating by the laser light that would otherwise shift the resonance condition during the simulation. Due to the small resonance width, this effect would affect the energy exchange during the simulations by changing the resonance condition. In Section 4.1.2, we saw that collisional damping can be comparable or even higher than the Landau damping for high Z plasma such as gold, but becomes marginal for low Z plasma as the one chosen in this chapter. Moreover, the damping distance covers several SCs and does not significantly affect the role of the speckle phase in modifying the energy exchange rate.

Laser parameters

Four Gaussian beams intersect four other Gaussian beams at an angle of $20°$. This configuration mimics 4 speckles of a beam crossing 4 speckles of another beam. All beams are linearly polarized, with their electric fields lying in the (x-y) simulation plane. The laser pulses propagate from the left to the right. The temporal evolution is a ramp of $1000\,\omega_L^{-1}$ followed by a plateau until the end of the simulation. The focal spots of the eight speckles are located in the middle of the simulation box and their intensity is $I = 8.8 \times 10^{13}\,\text{Wcm}^{-2}$ ($a_0 = 0.008$) with equal beam waists at $1/e$ of $w = 70\,c\,\omega_L^{-1}$ ($11\,\mu$m for $\lambda = 1\,\mu$m) at FWHM. All speckles are equally spaced by $\Delta y = 150\,c\,\omega_L^{-1}$. In the following, the group of 4 speckles is referred to as the beam. The field of each Gaussian speckle is defined in a theta-shifted plane with respect to y at focal spot. The field in the theta-shifted plane corresponds to the 2D Gaussian beam at focal spot as described in Eq. 3.32, with a phase shift term $e^{i\phi}$

$$E_{sp} = E_0 \sqrt{\frac{w_0}{w(x)}} e^{-i\frac{1}{2}\arctan x/x_r} e^{\frac{ik_0 y^2}{2R(x)}} e^{-\frac{y^2}{w(x)^2}} e^{i\phi}\,. \tag{5.21}$$

We recall that w_0 is the beam waist, $x_r = \frac{\pi w_0^2}{\lambda_0}$ is the Rayleigh length, and E_0 the amplitude at the beam center. The following notations are used $w(x) = w_0\sqrt{1 + \frac{x^2}{x_r^2}}$, $R(x) = x + \frac{x_r^2}{x}$. The

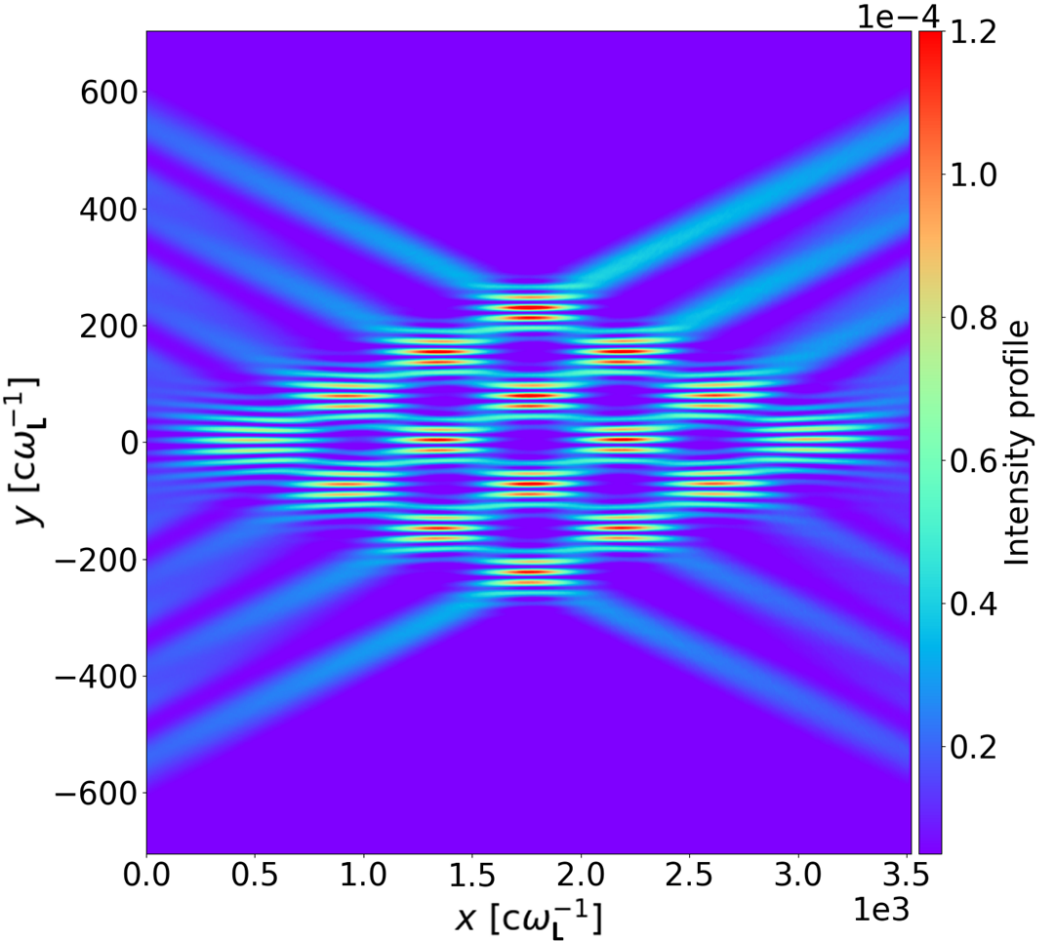

Figure 5.3: Intensity profile normalized to $2.74 \times 10^{18}/\lambda_{\mu m}^2\,\mathrm{W\ cm^{-2}}$ at time $3.4 \times 10^5\,\omega_L^{-1}$ for the wavelength shift case with phase shift.

frequency shift is chosen so as to match the resonance condition $\omega = kc_s = 1.81 \times 10^{-4}\,\omega_L$, the lower beams having the lowest frequency $(= 1 - 1.81 \times 10^{-4})$. For the phase shift case, the phases are (bottum up) $\phi = 0,\ 0.4,\ 4.5,\ 0.2$ for the upper beams $(y > 0)$ and $1,\ 0.1,\ 0.9,\ 5$ for the lower ones $(y < 0)$ and $\phi = 0$ for all beams for the in-phase case.

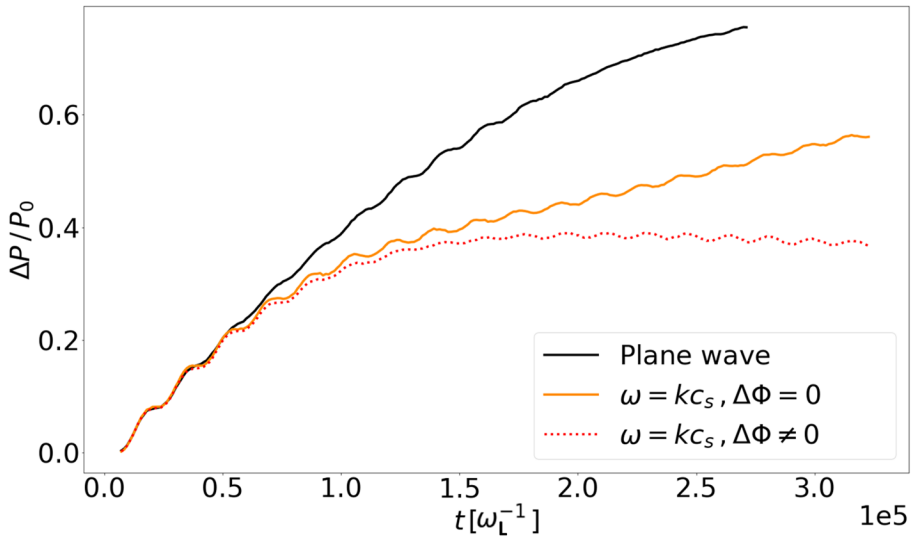

Figure 5.4: Difference between the power per unit length of the red-shifted and the blue-shifted beam normalized to the initial power versus time. Wavelength shift case without phase shift in orange solid line, with phase shift in red dashed line. The plane wave case, in dark solid line, is in fact the plasma flow case. The equivalence between those cases is demonstrated in Chapter 6.

5.2.2 Simulations results

Figure 5.3 is an intensity map showing the configuration of the simulations. Speckles enter the simulation box through the left side with the same energy, and escape through the right side. The Exchange occurs at each of the sixteen SC and the energy gain of the red-shifted beam, escaping through the upper right boundary, is discernible. To quantitatively compare the power exchange rate between cases with and without phase-shift, the exchanged powers per unit length are plotted in Fig. 5.4. All curves represent the power per unit length of the four escaping red-shifted speckles minus the power of the four blue-shifted speckles, normalized to the initial power per unit length. The power of the red-shifted / blue shifted beam has been obtained by integrating the Poynting vector at x_{max} over the upper ($y > 0$) / lower ($y < 0$) half of the simulation box shown in Fig. 5.3. Black line represents the plane wave case where the exchange reaches $\sim 70\%$. The orange line represents the in-phase SC case and the red dotted line the phase shifted SC case.

Both simulations exhibit the same tendency at early times. At late times, the in-phase case leads to more energy exchange (55%) than the out-of-phase case (35%). Note that the oscillations persist due to the long transient (the asymptotic regime is not reached at $t =$

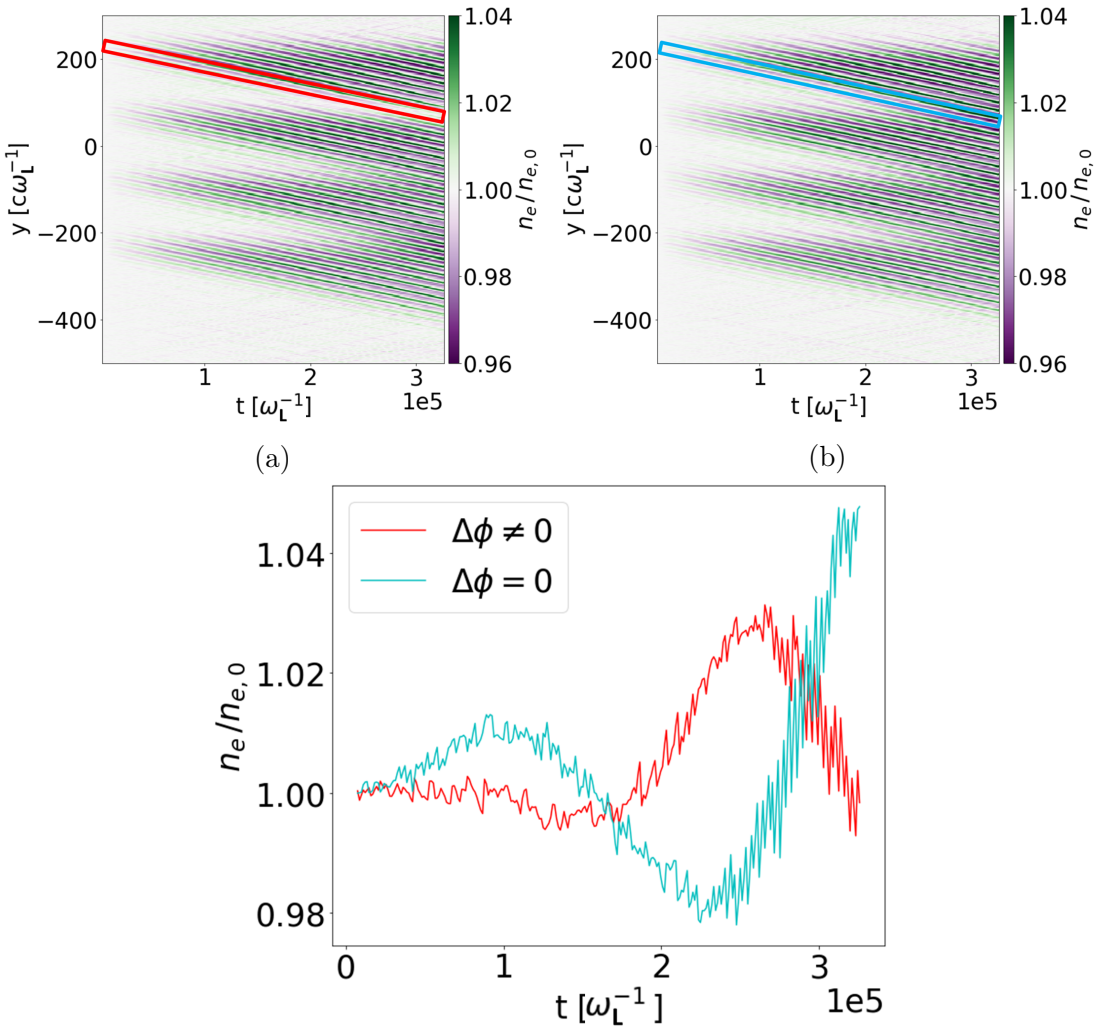

Figure 5.5: (y-t) density map for the in-phase (a) and out-of-phase (b) cases. (c) Envelope amplitude corresponding to the framed areas in panels (a) and (b).

$3.4 \times 10^5 \omega_L^{-1}$). The temporal difference between the two cases is attributed to the destructive interferences of the IAWs propagating from one SC to another. This effect is evidenced, shown by the (y-t) map of the ion density at the middle of the simulation ($x = 1750\,\mathrm{c}\omega_L^{-1}$), presented in Fig. 5.5 (a) and (b). The different temporal behaviors of the power exchange start as soon as the IAW generated at one SC has reached another crossing, confirming that both situations are equivalent before IAWs interfere and phase effects occur. Since the speckles centers are spaced by $\Delta y = 150\,\mathrm{c}\,\omega_L^{-1}$, the rising front of the IAW, generated roughly at $1/e$ of the speckle maximum intensity, reaches the next SC in a time of $\sim 80\,\mathrm{c}\,\omega_L^{-1}/c_s = 1.5 \times 10^5\,\omega_L^{-1}$. This

value is consistent with Fig. 5.4 where the difference between in-phase and out-of-phase cases appears at $t > 1.5 \times 10^5\, \omega_L^{-1}$ $(80\,\mathrm{ps})$. To further illustrate the evolution of the ion grating due to the IAWs propagation, Fig. 5.5 (c) shows the amplitude of an IAW following its trajectory at the sound speed $[n_e(y - c_s t, t, t_0 = 0, y_0 = 100)]$. In the in-phase case ($\Delta\phi = 0$), the IAW envelope reaches higher values owing to the constructive interference compared to the out-of-phase case. These IAWs interferences may explain the overestimate of the energy exchange by plane wave models.

To conclude, we have investigated the exchange between two laser beams with different frequencies in the lab frame, by means of kinetic simulations and a linear model. The random phase shift between the interference gratings, situated at each crossing speckles, is an important factor of energy exchange inhibition. Indeed, the driven IAWs issued from each crossing speckles, can interfere destructively, thereby reducing the light scattering by the ion gratings. This effect is particularly efficient in weakly damped plasmas where the IAWs can travel through many speckles. In strong Landau damped plasma, such as plastic CH, an inhibition of CBET persists, with values around 10 to 30 % compared to the plane wave limit. When the damping distance is comparable with the speckle transverse size, the ponderomotive force producing the moving grating in the plasma reference frame is averaged over the speckle, thereby reducing the amplitude of the driven IAW. These findings are supported by a linear model that describes the IAW response due to out-of-phase speckles, derived in a homogeneous plasmas and valid from weak to highly Landau-damped plasmas. Additionally, a substantial modification of the IAW could question the validity of plane wave-based non-linear models, regarding RPP beams. These results can partly explain why the experimental exchange is often over-estimated in the indirect-drive approach, when using different laser frequencies.

Chapter 6

Difference between a plasma flow and a wavelength shift

Contents

In virtue of the resonance condition, two laser beams with a matching frequency shift, crossing in a stationary plasma should lead to the same amount of energy exchange, as two laser beams without frequency shift, crossing in a sonic plasma. Most CBET models [107, 67, 16, 15, 61, 106, 27, 17] assume this equivalence as they are built from a nearly plane wave assumption. This chapter aims at demonstrating that this assertion is false due to the speckle structure of the laser intensity profile. Within the plane wave approximation, equal frequency laser beams crossing in a sonic plasma ($\widehat{k} \cdot \mathbf{v}_d = -c_s$) exchange the same amount of energy as two laser beams with frequency difference $\omega_0 - \omega_1 = |\boldsymbol{k_0} - \boldsymbol{k_1}|c_s$, in a plasma with no flow. Nevertheless, there is an inherent difference between these two configurations. In the reference frame of a moving plasma, the envelope of two crossing speckles, together with the interference grating, are moving at $\mathbf{v}_d$. In a stationary plasma, the wavelength shift leads to an interference grating moving at $\omega/|\mathbf{k}|$ whereas the SC envelope remains motionless. For infinite laser envelope or when the Landau damping distance is small compared to the speckle waist, both situations become equivalent. Yet, in most ICF plasmas, these two systems are distinct because the IAWs are not stimulated by the same potential well. In the present chapter, we demonstrate that the speckle structure questions the relevance of the plane wave approximation in the wavelength shift case, and can explain the disagreement between models and experimental results involving low to high Z materials, before accounting for ion trapping [69, 118, 35] or beam deflection and self-focusing [89]. The speckle structure may reduce CBET by about 30% in strongly damped CH plasmas, and up to 50-70% in high Z silicon ablators [34] or in the gold bubble in low gas filled hohlraum [47].

In Section 6.1, we present a linear model to estimate the plasma parameters for which the speckle structure cannot be neglected, supported by subsequent simulations. Then, 2D Calder [56] PIC simulations describing the exchange between two beams, each composed of four speckles in a weakly damped plasma are shown in Section 6.2. Finally, 6.3 presents Smilei simulations with a realistic RPP configuration. For both section 6.2 and 6.3, we consider situations with and without plasma flow, and when CBET is at, or out of, resonance.

6.1 Cross-Beam Energy Transfer Random Phase Plate model

6.1.1 Calculation with speckles of infinite length

Wave propagation

In the laboratory reference frame (where we recall that $v_d < 0$, as explained in 4.3.1), the wave is stimulated by the field resulting from the beating between the two crossing beams along y according to

$$[(\partial_t - v_d\partial_y)^2 + 2\nu(\partial_t - v_d\partial_y) - c_s^2\partial_y^2]\delta N_e = -\frac{Zn_{e,0}|\boldsymbol{k}|^2}{2m_i}A_0A_1^\star\,, \tag{6.1}$$

where the laser fields A_0 and $A_1^\star$ can be calculated considering the problem geometry shown in Figure. 6.1. We recall Eq. (3.63), written hereafter for $N+1 \simeq N \gg 1$:

$$A = ae^{i\boldsymbol{k_0}\cdot\boldsymbol{r}-i\omega t}\frac{1}{N}\sum_{k^\perp=-k_{max}}^{k_{max}} e^{i\varphi_{k^\perp}}e^{i\boldsymbol{k}^\perp\cdot\boldsymbol{r}}\,. \tag{6.2}$$

Here, the calculation is centered at focal spot considering the focal plane is located at $x = 0$. Then, applying a rotation of $\pm\theta$ for each beam

$$A_0 = \frac{a_0}{N}\sum_{k_1^\perp} e^{-i\omega_0 t}e^{ix(k_{01}\cos\theta - k_1^\perp\sin\theta)}e^{iy(k_{01}\sin\theta + k_1^\perp\cos\theta)}e^{i\varphi_1(k_1^\perp)}\,,$$

$$A_1 = \frac{a_1}{N}\sum_{k_2^\perp} e^{-i\omega_1 t}e^{ix(k_{02}\cos\theta + k_2^\perp\sin\theta)}e^{iy(-k_{02}\sin\theta + k_2^\perp\cos\theta)}e^{i\varphi_2(k_2^\perp)}\,. \tag{6.3}$$

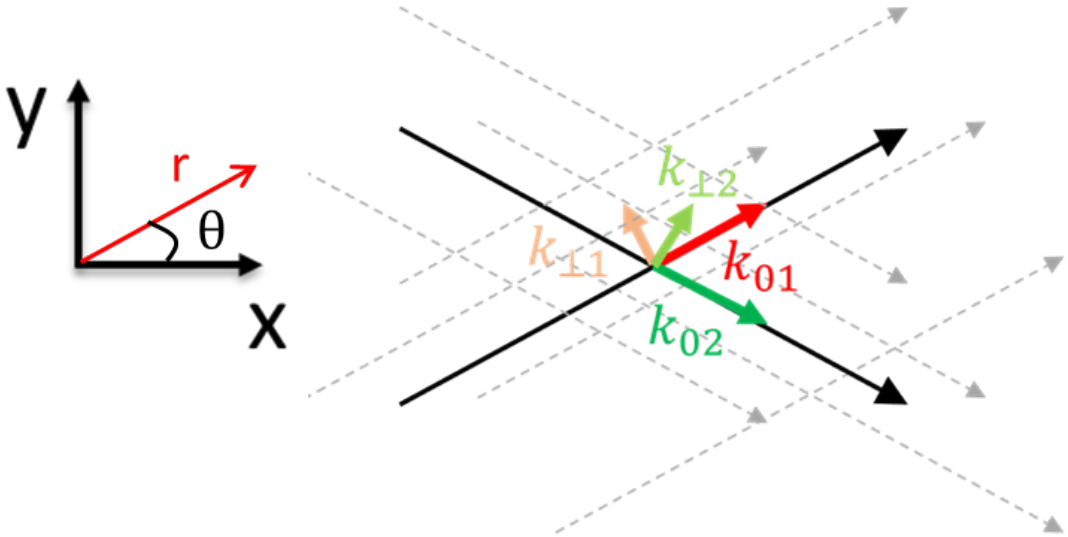

Figure 6.1: RPP wave vector scheme

The ponderomotive beat wave thus writes

$$\begin{aligned} A_0 A_1^\star &= \frac{1}{N^2}(a_0 \sum_{k_1^\perp} e^{-i\omega_0 t} e^{ix(k_{01}\cos\theta - k_1^\perp \sin\theta)} e^{iy(k_{01}\sin\theta + k_1^\perp \cos\theta)} e^{i\varphi_1(k_1^\perp)}) \\ &\quad \times (a_1 \sum_{k_2^\perp} e^{-i\omega_1 t} e^{ix(k_{02}\cos\theta + k_2^\perp \sin\theta)} e^{iy(-k_{02}\sin\theta + k_2^\perp \cos\theta)} e^{i\varphi_2(k_2^\perp)})^\star , \\ &= e^{ix\cos\theta(k_{01}-k_{02})} e^{iy\sin\theta(k_{01}+k_{02})} e^{-i\omega_0 t + i\omega_1 t} \frac{a_0 a_1^\star}{N^2} \sum_{k_1^\perp} \sum_{k_2^\perp} e^{-ix\sin\theta(k_1^\perp + k_2^\perp)} e^{iy(\cos\theta(k_1^\perp - k_2^\perp))} e^{i(\varphi_1(k_1^\perp) - \varphi_2(k_2^\perp))} . \end{aligned} \tag{6.4}$$

From this expression, with $\omega = \omega_0 - \omega_1$ and $k = (k_{01} + k_{02})\sin\theta \simeq 2k_0 \sin\theta$, the envelope of the beat wave, $\widetilde{A}_0 \widetilde{A}_1^\star = A_0 A_1^\star e^{-iky + i\omega t}$, can be deduced

$$\widetilde{A}_0 \widetilde{A}_1^\star = e^{ix\cos\theta(k_{01}-k_{02})} \frac{a_0 a_1^\star}{N^2} \sum_{k_1^\perp} \sum_{k_2^\perp} e^{-ix\sin\theta(k_1^\perp + k_2^\perp)} e^{iy(\cos\theta(k_1^\perp - k_2^\perp))} e^{i(\varphi_1(k_1^\perp) - \varphi_2(k_2^\perp))} . \tag{6.5}$$

The wave propagation in the laboratory reference frame recasts

$$
\begin{aligned}
&[(\partial_t - v_d\partial_y)^2 + 2\nu(\partial_t - v_d\partial_y) - c_s^2\partial_y^2]\delta N_e \\
&= 2\alpha e^{iky-i\omega t} e^{ix\cos\theta(k_{01}-k_{02})} \frac{1}{N^2} \sum_{k_1^\perp} \sum_{k_2^\perp} e^{-ix\sin\theta(k_1^\perp + k_2^\perp)} e^{iy(\cos\theta(k_1^\perp - k_2^\perp))} e^{i(\varphi_1(k_1^\perp) - \varphi_2(k_2^\perp))} ,
\end{aligned}
\tag{6.6}
$$

where α is defined in Eq. (4.41). This equation is resolved applying a spatial FT along the y axis, defined as $\overline{f} = \int f(y)\mathrm{e}^{-i\overline{k}y}dy$. Equation (6.6), thus becomes an ordinary differential equation:

$$
\begin{aligned}
&[\partial_t^2 + (2\nu - 2i\overline{k}v_d)\partial_t - 2i\nu v_d\overline{k} - (v_d^2 - c_s^2)\overline{k}^2]\delta\overline{N}_e = \\
&2\alpha e^{-i\omega t} \frac{1}{N^2} e^{ix\cos\theta(k_{01}-k_{02})} \sum_{k_1^\perp} \sum_{k_2^\perp} e^{-ix\sin\theta(k_1^\perp + k_2^\perp)} \delta(\overline{k} - k - \cos\theta(k_1^\perp - k_2^\perp)) e^{i(\varphi_1(k_1^\perp) - \varphi_2(k_2^\perp))} ,
\end{aligned}
\tag{6.7}
$$

with the particular solution:

$$
\begin{aligned}
\delta\overline{N_e}^{PS} &= \frac{2\alpha}{N^2} e^{-i\omega t} e^{ix\cos\theta(k_{01}-k_{02})} \\
&\times \sum_{k_1^\perp} \sum_{k_2^\perp} e^{-ix\sin\theta(k_1^\perp + k_2^\perp)} e^{i(\varphi_1(k_1^\perp) - \varphi_2(k_2^\perp))} \frac{\delta(\overline{k} - k - \cos\theta(k_1^\perp - k_2^\perp))}{-(\omega + \overline{k}v_d)^2 - 2i\nu(\omega + \overline{k}v_d) + c_s^2\overline{k}^2} .
\end{aligned}
\tag{6.8}
$$

Taking $\overline{N}_{e_{|t=0}} = 0$ and $\partial_t\delta\overline{N}_{e_{|t=0}} = 0$ as initial conditions, it comes

$$
\delta\overline{N_e} = \frac{2\alpha}{N^2} e^{-i\omega t} e^{ix\cos\theta(k_{01}-k_{02})} \sum_{k_1^\perp} \sum_{k_2^\perp} e^{-ix\sin\theta(k_1^\perp + k_2^\perp)} e^{i(\varphi_1(k_1^\perp) - \varphi_2(k_2^\perp))} \delta(\overline{k} - k - \cos\theta(k_1^\perp - k_2^\perp)) f(\overline{k}) ,
\tag{6.9}
$$

where we recall Eq. (4.37)

$$
\begin{aligned}
f(K) = &\frac{1}{-(\omega + Kv_d)^2 - 2i\nu(\omega + Kv_d) + c_s^2K^2} \\
&\times \left(1 + \frac{i\omega + \lambda(K)_-}{\lambda(K)_+ - \lambda(K)_-} e^{\lambda(K)_+ t - i\omega t} + \frac{i\omega + \lambda(K)_+}{\lambda(K)_+ - \lambda(K)_-} e^{\lambda(K)_- t - i\omega t}\right) ,
\end{aligned}
\tag{6.10}
$$

and

$$\lambda_{\pm}(K) = -\nu + iKv_{d_{\parallel}} \pm i\sqrt{c_s^2K^2 - \nu^2}\,. \tag{6.11}$$

Applying the inverse FT, we obtain the acoustic wave:

$$\begin{aligned}\delta N_e = &\frac{2\alpha}{N^2}e^{i(ky-\omega t)}e^{ix\cos\theta(k_{01}-k_{02})}\\ &\times\sum_{k_1^\perp}\sum_{k_2^\perp}e^{iy\cos\theta(k_1^\perp-k_2^\perp)}e^{-ix\sin\theta(k_1^\perp+k_2^\perp)}e^{i(\varphi_1(k_1^\perp)-\varphi_2(k_2^\perp))}f(k+\cos\theta(k_1^\perp-k_2^\perp))\,.\end{aligned} \tag{6.12}$$

Let δN_e^{driven} be the asymptotic solution when $t \longrightarrow \infty$, in which case $e^{\lambda(k)\pm t} \longrightarrow 0$ and $\delta\widetilde{N}_e^{driven} = \delta N_e^{driven}e^{-(iky-i\omega t)}$ is the wave envelope,

$$\begin{aligned}\delta\widetilde{N}_e^{driven} = &\frac{2\alpha}{N^2}e^{ix\cos\theta(k_{01}-k_{02})}\\ &\times\sum_{k_1^\perp}\sum_{k_2^\perp}e^{iy\cos\theta(k_1^\perp-k_2^\perp)}e^{-ix\sin\theta(k_1^\perp+k_2^\perp)}e^{i(\varphi_1(k_1^\perp)-\varphi_2(k_2^\perp))}\,\widetilde{f}(k+\cos\theta(k_1^\perp-k_2^\perp))\,,\end{aligned} \tag{6.13}$$

where we recall Eq. (4.40)

$$\widetilde{f}(K) = \frac{1}{-(\omega+Kv_d)^2 - 2i\nu(\omega+Kv_d) + c_s^2K^2}\,. \tag{6.14}$$

Energy exchange

The wave coupling is analyzed perturbatively as in Chapter 5 and leads to Eq. (5.13):

$$\begin{aligned}\boldsymbol{k}_{01}\boldsymbol{\nabla}\cdot\delta I_0 \simeq k_0\partial_r\delta I_0 &= \frac{1}{2}\,\mathrm{Im}\Big\{\delta\widetilde{N}_e^{driven}\widetilde{A}_1^0\widetilde{A}_0^{0\star}\Big\}\,,\\ &= \mathrm{Im}\Bigg\{\frac{\alpha a_0^\star a_1}{N^4}\sum_{k_1^\perp}\sum_{k_2^\perp}\sum_{k_3^\perp}\sum_{k_4^\perp} e^{-ix\sin\theta(k_1^\perp+k_2^\perp-k_3^\perp-k_4^\perp)}e^{iy\cos\theta(k_1^\perp-k_2^\perp-k_3^\perp+k_4^\perp)}\\ &\qquad\times e^{i(\varphi_1(k_1^\perp)-\varphi_2(k_2^\perp)-\varphi_1(k_3^\perp)+\varphi_2(k_4^\perp))}\widetilde{f}(k+(k_1^\perp-k_2^\perp)\cos\theta)\Bigg\}. \quad (6.15)\end{aligned}$$

To resolve this equation, coordinates are changed using $x = x_0 + r\cos\theta$ and $y = y_0 + r\sin\theta$. Coordinates $x_0 = 0$ and y_0 are chosen so as to be on a speckle (i.e. intensity maximum of I_0+I_1, without considering the grating). When y_0 is not chosen conveniently, the characteristic may be on the area between two speckles. In this case, the intensity variation observed is not relevant and the deduced δI_0 can be considered as a noise compared to CBET.

$$\begin{aligned}&k_0\partial_r\delta I_0 =\\ &\quad\mathrm{Im}\Bigg\{\frac{\alpha a_0^\star a_1}{N^4}\sum_{k_1^\perp}\sum_{k_2^\perp}\sum_{k_3^\perp}\sum_{k_4^\perp} e^{-ir\cos\theta\sin\theta(k_1^\perp+k_2^\perp-k_3^\perp-k_4^\perp)}e^{i\cos\theta(r\sin\theta+y_0)(k_1^\perp-k_2^\perp-k_3^\perp+k_4^\perp)}\\ &\qquad\times e^{i(\varphi_1(k_1^\perp)-\varphi_2(k_2^\perp)-\varphi_1(k_3^\perp)+\varphi_2(k_4^\perp))}\widetilde{f}(k+(k_1^\perp-k_2^\perp)\cos\theta)\Bigg\},\\ \implies\ &\delta I_0 = \frac{\alpha a_0^\star a_1}{k_0N^4}\times\mathrm{Im}\Bigg\{\sum_{k_1^\perp,k_2^\perp,k_3^\perp,k_4^\perp} e^{i(\varphi_1(k_1^\perp)-\varphi_2(k_2^\perp)-\varphi_1(k_3^\perp)+\varphi_2(k_4^\perp))}e^{iy_0\cos\theta(k_1^\perp-k_2^\perp-k_3^\perp+k_4^\perp)}\\ &\qquad\times\widetilde{f}(k+(k_1^\perp-k_2^\perp)\cos\theta)\int_{-R/2}^{R/2}e^{2ir\cos\theta\sin\theta(-k_2^\perp+k_4^\perp)}dr\Bigg\} \quad (6.16)\end{aligned}$$

The integration over the width L of the beam corresponds to r varying from $-L/2\sin 2\theta$ to

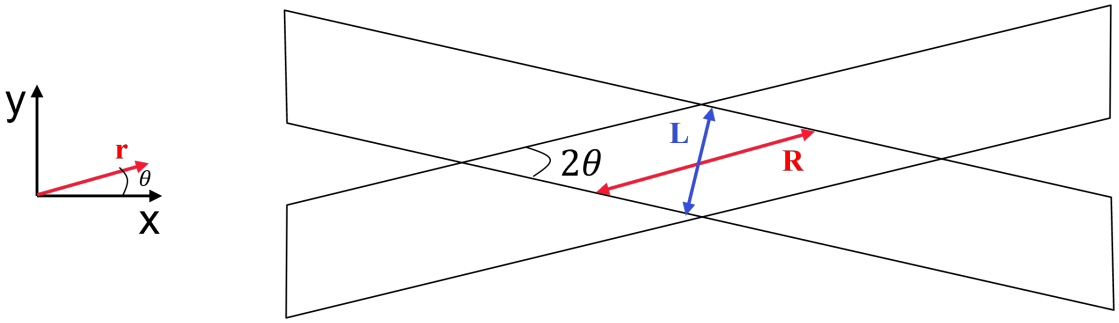

Figure 6.2: crossing zone geometry

$L/2\sin 2\theta$ according to fig. 6.2:

$$\delta I_0 = \frac{\alpha a_0^\star a_1}{k_0 N^4} \times \mathrm{Im}\Bigg\{ \sum_{k_1^\perp,k_2^\perp,k_3^\perp,k_4^\perp} e^{i(\varphi_1(k_1^\perp)-\varphi_2(k_2^\perp)-\varphi_1(k_3^\perp)+\varphi_2(k_4^\perp))} e^{iy_0\cos\theta(k_1^\perp-k_2^\perp-k_3^\perp+k_4^\perp)} \times \widetilde{f}(k+(k_1^\perp-k_2^\perp)\cos\theta)\int_{-L/2\sin 2\theta}^{L/2\sin 2\theta} e^{2ir\cos\theta\sin\theta(-k_2^\perp+k_4^\perp)}dr \Bigg\},$$

$$= \frac{\alpha a_0^\star a_1}{k_0 N^4} \times \mathrm{Im}\Bigg\{ \sum_{k_1^\perp,k_2^\perp,k_3^\perp,k_4^\perp} e^{i(\varphi_1(k_1^\perp)-\varphi_2(k_2^\perp)-\varphi_1(k_3^\perp)+\varphi_2(k_4^\perp))} e^{iy_0\cos\theta(k_1^\perp-k_2^\perp-k_3^\perp+k_4^\perp)} \times \widetilde{f}(k+(k_1^\perp-k_2^\perp)\cos\theta)\,\mathrm{sinc}\left[\frac{L}{2}(-k_2^\perp+k_4^\perp)\right]\frac{L}{\sin 2\theta} \Bigg\}, \quad (6.17)$$

$$\Longrightarrow \frac{\delta I_0}{I_0} = \frac{\alpha_1 L}{k_0 N^2 \sin 2\theta} \times \mathrm{Im}\Bigg\{ \sum_{k_1^\perp,k_2^\perp,k_3^\perp,k_4^\perp} e^{i(\varphi_1(k_1^\perp)-\varphi_2(k_2^\perp)-\varphi_1(k_3^\perp)+\varphi_2(k_4^\perp))} \times e^{iy_0\cos\theta(k_1^\perp-k_2^\perp-k_3^\perp+k_4^\perp)} \times \widetilde{f}(k+(k_1^\perp-k_2^\perp)\cos\theta)\,\mathrm{sinc}\,\frac{L}{2}(-k_2^\perp+k_4^\perp) \Bigg\}, \quad (6.18)$$

where $\alpha_1 = -\frac{Z n_{e,0} k^2}{4\tilde{m}_i}\frac{a_1 a_1^\star}{N} = -\frac{Z n_{e,0} k^2}{4\tilde{m}_i} I_1$.

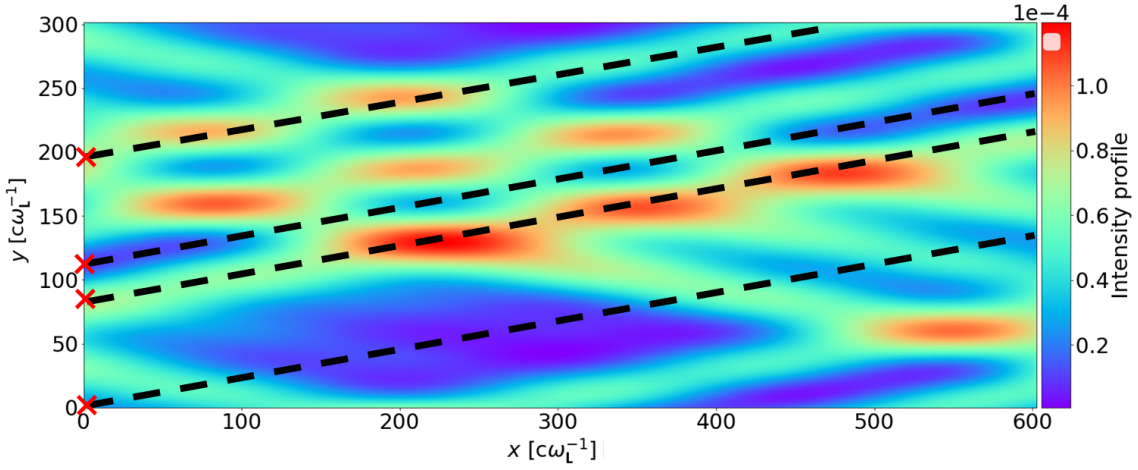

(a)

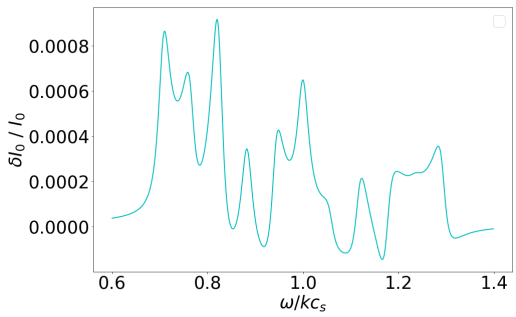

(b) $y_0 = 0$

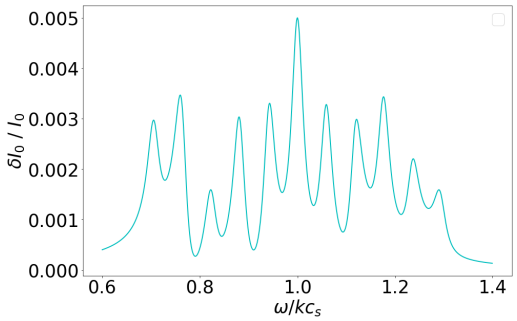

(c) $y_0 = 81$

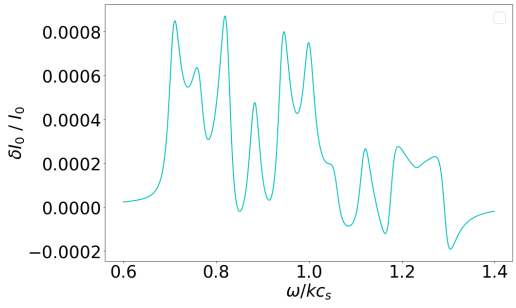

(d) $y_0 = 110$

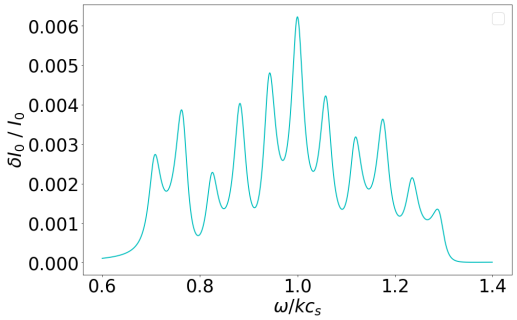

(e) $y_0 = 191$

Figure 6.3: (a) Speckles intensity envelope $(I_0 + I_1)$. The dashed lines represent the characteristics issued from different y_0 represented by red cross and used to calculate the exchange in the other panels. (b)-(f) Exchange versus the distance from the resonance for five different characteristics, for the wavelength shift case and N=6.

To illustrate the importance of the initial condition, Fig. 6.3 shows the intensity exchange versus the resonance for different y_0. When the latter is located on a speckle of the red-

shifted beam, the energy exchange is only positive. When y_0 lies in an intensity minimum, the amplitude of the exchange is almost ten times smaller, with sometimes anti-stokes energy exchange. The exchange rate along the speckle remains low and these curves do not seem to allow a realistic quantitative estimation of the exchange. We introduce the average of the energy exchange issued from the crossing of two RPP beams by performing an average over φ. This definition is equivalent to having many realisations of CBET between RPP beams with different phase plates. As the exchange in the regions without speckles is negligible, the main contribution in this average comes from the SC. As $\varphi_1(k_1^\perp)$ is correlated to $\varphi_1(k_3^\perp)$, and $\varphi_2(k_2^\perp)$ to $\varphi_2(k_4^\perp)$, Eq. (6.18) reduces to

$$\frac{\langle \delta I_0 \rangle_\varphi}{I_0} = \frac{\alpha_1 L}{k_0 N^2 \sin 2\theta} \mathrm{Im} \Bigg\{ \sum_{k_1^\perp, k_2^\perp, k_3^\perp, k_4^\perp} \delta(k_1^\perp - k_3^\perp)\delta(k_2^\perp - k_4^\perp) e^{iy_0 \cos\theta (k_1^\perp - k_2^\perp - k_3^\perp + k_4^\perp)} \times \widetilde{f}(k + (k_1^\perp - k_2^\perp)\cos\theta)\, \mathrm{sinc}\, \frac{L}{2}(-k_2^\perp + k_4^\perp) \Bigg\}, \quad (6.19)$$

$$\implies \frac{\langle \delta I_0 \rangle_\varphi}{I_0} = \frac{\alpha_1 L}{k_0 N^2 \sin 2\theta} \times \mathrm{Im} \Bigg\{ \sum_{k_1^\perp, k_2^\perp} \widetilde{f}(k + (k_1^\perp - k_2^\perp)\cos\theta) \Bigg\}, \quad (6.20)$$

where δ is the Kronecker delta. The exchange mainly depends on the crossing zone size, which changes with the crossing angle. Except for very small ($1/f \simeq 0.5°$) or very large ($180 - 1/f \simeq 179.5°$) angles, the speckles Rayleigh length exceeds the size of the crossing zone. Moreover, the speckles have a high probability to intersect in 2D so diffraction should not affect the exchange. The calculation is made bellow to verify this assumption.

6.1.2 Calculation with finite length speckles

Wave propagation

The finite length of the speckles stems from diffraction and is described by formula Eq. (3.61), written here with the sum over n :

$$A = ae^{-i\omega_0 t}\frac{1}{N}\sum_{n=-N/2}^{N/2} e^{ik_0\cos\theta_n x + ik_0\sin\theta_n y}e^{i\varphi_n}\,. \tag{6.21}$$

As in the previous section, the calculation is centered at focal spot considering $x \simeq 0$, and the calculation of the IAW response and CBET is similar. First, applying a rotation of $+\theta$ to A_0 and $-\theta$ to A_1 allows to express the beating wave term as:

$$\begin{aligned}
A_0 &= \frac{a_0}{N}e^{-i\omega_1 t}\sum_{n_1=-N/2}^{N/2} e^{ik_0[\cos(\theta+\theta_{n1})x + sin(\theta+\theta_{n1})y]}e^{i\varphi_1(n_1)}\,,\\
A_1 &= \frac{a_1}{N}e^{-i\omega_2 t}\sum_{n_2=-N/2}^{N/2} e^{ik_0[\cos(-\theta+\theta_{n2})x + \sin(-\theta+\theta_{n2})y]}e^{i\varphi_2(n_2)}\,,\\
\implies A_0A_1^\star &= \frac{a_0a_1^\star}{N^2}e^{-i\omega t}\sum_{n_1=-N/2}^{N/2}\sum_{n_2=-N/2}^{N/2} e^{ik_0x[\cos(\theta+\theta_{n1})-\cos(-\theta+\theta_{n2})]}\\
&\qquad\times e^{ik_0y[\sin(\theta+\theta_{n1})-\sin(-\theta+\theta_{n2})]}e^{i\varphi_1(n_1)-i\varphi_2(n_2)}\,.
\end{aligned} \tag{6.22}$$

All phase plate elements are here statistically independent, including between the two beams so that the following average will be applied,

$$\langle e^{i\varphi_{u_1}(n_1)-i\varphi_{u2}(n_2)}\rangle = \delta(u_1-u_2)\delta(n_1-n_2)\,. \tag{6.23}$$

The resolution of the wave equation,

$$\left[(\partial_t + v_d\partial_y)^2 + 2\nu(\partial_t + v_d\partial_y) - c_s^2\partial_y^2\right]\delta N_e = \frac{2\alpha}{N^2}e^{-i\omega t}\sum_{n_1,n_2} e^{ik_0x[\cos(\theta+\theta_{n1})-\cos(-\theta+\theta_{n2})]}e^{ik_0y[\sin(\theta+\theta_{n1})-\sin(-\theta+\theta_{n2})]}e^{i\varphi_1(n_1)-i\varphi_2(n_2)}\,, \tag{6.24}$$

is similar to the previous section and leads to

$$\delta N_e = \frac{2\alpha}{N^2}e^{-i\omega t}\sum_{n_1,n_2} e^{ik_0x[\cos(\theta+\theta_{n1})-\cos(-\theta+\theta_{n2})]}e^{ik_0y[\sin(\theta+\theta_{n1})-\sin(-\theta+\theta_{n2})]} \times e^{i\varphi_1(n_1)-i\varphi_2(n_2)}f(k_0\sin(\theta+\theta_{n1}) - k_0\sin(-\theta+\theta_{n2}))\,. \tag{6.25}$$

For long times, the remaining driven solution is

$$\delta N_e^{\text{driven}} = \frac{2\alpha}{N^2}e^{-i\omega t}\sum_{n_1,n_2} e^{ik_0x[\cos(\theta+\theta_{n1})-\cos(-\theta+\theta_{n2})]}e^{ik_0y[\sin(\theta+\theta_{n1})-\sin(-\theta+\theta_{n2})]} \times e^{i\varphi_1(n_1)-i\varphi_2(n_2)}\widetilde{f}(k_0\sin(\theta+\theta_{n1}) - k_0\sin(-\theta+\theta_{n2}))\,. \tag{6.26}$$

Energy exchange

Starting from Eq. (5.12), we obtain

$$\frac{\mathbf{k}_0\cdot\nabla\delta I_0}{I_0} = \text{Im}\left\{\frac{\alpha_1}{N^2}\sum_{n_1,n_2,n_3,n_4} e^{ik_0x\Theta_{nx}}e^{ik_0y\Theta_{ny}}f(k_0\sin(\theta+\theta_{n1}) - k_0\sin(-\theta+\theta_{n2})) \times e^{i[\varphi_1(n_1)-\varphi_2(n_2)-\varphi_1(n_3)+\varphi_2(n_4)]}\right\}, \tag{6.27}$$

where

$$\Theta_{nx} = \cos(\theta + \theta_{n1}) - \cos(-\theta + \theta_{n2}) \qquad - \cos(\theta + \theta_{n3}) + \cos(-\theta + \theta_{n4}),$$
$$\Theta_{ny} = \sin(\theta + \theta_{n1}) - \sin(-\theta + \theta_{n2}) \qquad - \sin(\theta + \theta_{n3}) + \sin(-\theta + \theta_{n4}). \tag{6.28}$$

The resolution, similar to the previous section, gives

$$\frac{\delta I_0}{I_0} = \frac{\alpha_1 L}{k_0 N^2 \sin 2\theta} \mathrm{Im}\left\{ \sum_{n_1,n_2,n_3,n_4} e^{ik_0 y_0 \Theta_{ny}} f(k_0 \sin(\theta + \theta_{n1}) - k_0 \sin(-\theta + \theta_{n2})) \right.$$
$$\left. \times e^{i[\varphi_1(n_1) - \varphi_2(n_2) - \varphi_1(n_3) + \varphi_2(n_4)]} \times \mathrm{sinc}(k_0 \cos\theta \Theta_{nx} + k_0 \sin\theta \Theta_{ny}) \right\}. \tag{6.29}$$

The average value over φ is

$$\frac{\langle \delta I_0 \rangle_\varphi}{I_0} = \frac{\alpha_1 L}{k_0 N^2 \sin 2\theta} \mathrm{Im}\left\{ \sum_{n_1,n_2} f(k_0 \sin(\theta + \theta_{n1}) - k_0 \sin(-\theta + \theta_{n2})) \right\}. \tag{6.30}$$

6.1.3 Comparison between a plane wave, a plasma flow, and a wavelength shift case

We recall Eq. (6.13) :

$$\delta N_e^{driven} = \frac{2\alpha}{N^2} e^{i(ky - \omega t)} e^{ix \cos\theta (k_{01} - k_{02})}$$
$$\times \sum_{k_1^\perp} \sum_{k_2^\perp} e^{iy \cos\theta (k_1^\perp - k_2^\perp)} e^{-ix \sin\theta (k_1^\perp + k_2^\perp)} e^{i(\varphi_1(k_1^\perp) - \varphi_2(k_2^\perp))} \widetilde{f}(k + \cos\theta (k_1^\perp - k_2^\perp)),$$

where $\widetilde{f}(K)$ at resonance and in the plasma flow case ($\omega = 0$, $v_d = -c_s$) is

$$\widetilde{f}(K) = \frac{1}{2i\nu K c_s}\,, \tag{6.31}$$

$$= \frac{1}{2i\nu c_s k(1+\frac{1}{k}\cos\theta(k_1^\perp - k_2^\perp))}\,, \tag{6.32}$$

$$\simeq \frac{1}{2i\nu c_s k}\,. \tag{6.33}$$

Thus, the driven wave can be expressed as:

$$\begin{aligned}\delta N_e^{driven} = \frac{1}{i\nu c_s k}\frac{\alpha}{N^2}e^{iky}e^{ix\cos\theta(k_{01}-k_{02})} \\ \times\sum_{k_1^\perp}\sum_{k_2^\perp}e^{iy\cos\theta\cdot(k_1^\perp-k_2^\perp)}e^{-ix\sin\theta(k_1^\perp+k_2^\perp)}e^{i(\varphi_1(k_1^\perp)-\varphi_2(k_2^\perp))}\,, \\ = \frac{\alpha}{i\nu c_s k}e^{ikx-i\omega t}\frac{\widetilde{A}_0\widetilde{A}_1^\star}{I_0}\,,\end{aligned} \tag{6.34}$$

which corresponds to the plane wave solution Eq. (4.38) at resonance multiplied by the normalized crossing envelope amplitude $\widetilde{A}_0\widetilde{A}_1^\star/I_0$. This result shows that the amplitude of the wave only depends on the local beating wave as for a plane wave situation. Indeed, when $\omega = 0$, the interference pattern is stationary with respect to the beam envelope (or speckles). There is no travelling wave, so no interference between waves issued from different crossings. In the same way, this equivalence can be demonstrated in the case with diffraction. Recalling Eq. (6.26)

$$\begin{aligned}\delta N_e^{driven} = \frac{2\alpha}{N^2}e^{-i\omega t}\sum_{n_1,n_2}e^{ik_0x[\cos(\theta+\theta_{n1})-\cos(-\theta+\theta_{n2})]}e^{ik_0y[\sin(\theta+\theta_{n1})-\sin(-\theta+\theta_{n2})]} \\ \times e^{i\varphi_1(n_1)-i\varphi_2(n_2)}\widetilde{f}(k_0\sin(\theta+\theta_{n1})-k_0\sin(-\theta+\theta_{n2}))\,,\end{aligned} \tag{6.35}$$

where $\widetilde{f}(k_0\sin(\theta+\theta_{n1})-k_0\sin(-\theta+\theta_{n2}))$ at resonance and in the plasma flow case is

$$\widetilde{f}(k_0\sin(\theta+\theta_{n1})-k_0\sin(-\theta+\theta_{n2})) = \frac{1}{2i\nu c_s k_0(\sin(\theta+\theta_{n1})-\sin(-\theta+\theta_{n2}))}\,. \tag{6.36}$$

When the angle between the beams is larger than the RPP aperture ($\theta \gg \theta_{max} = k_0/2f_\#$), the previous expression becomes

$$\widetilde{f}(k_0 \sin(\theta + \theta_{n1}) - k_0 \sin(-\theta + \theta_{n2})) \simeq \frac{1}{2i\nu c_s 2k_0 \sin\theta}\,, \tag{6.37}$$

$$= \frac{1}{2i\nu k c_s}\,. \tag{6.38}$$

The equivalence between the plasma flow and the plane wave case has been theoretically demonstrated in the case with speckles of finite length. **In the following, we will now refer to the plasma flow case as the plane wave case.**

In the wavelength shift case at resonance ($\omega = kc_s$, $v_d = 0$),

$$\widetilde{f}(k + \cos\theta(k_1^\perp - k_2^\perp)) = \frac{1}{-2i\nu\omega + \cos^2\theta(k_1^\perp - k_2^\perp)^2 c_s^2}\,. \tag{6.39}$$

In this case, the resonance between the IAWs and the crossing envelopes induces a beating between k and the different $k^\perp$ contributions preventing the resonance of ω/k with c_s. This effect leads to a smaller wave amplitude. In the same way for the case with diffraction,

$$\widetilde{f}(k_0 \sin(\theta + \theta_{n1}) - k_0 \sin(-\theta + \theta_{n2})) = \frac{1}{-\omega^2 - 2i\nu\omega + \big(\sin(\theta + \theta_{n1}) - \sin(-\theta + \theta_{n2})\big)^2 k_0^2 c_s^2}\,,$$

$$= \frac{1}{-\omega^2 - 2i\nu\omega + \big(\sin\theta(\cos\theta_{n_1} + \cos\theta_{n_2}) + \cos\theta(\sin\theta_{n_1} - \sin\theta_{n_2})\big)^2 k_0^2 c_s^2}\,. \tag{6.40}$$

Considering the RPP aperture is smal ($\theta_{max} = k_0/2f_\# \ll 1$),

$$\widetilde{f}(k_0 \sin(\theta + \theta_{n1}) - k_0 \sin(-\theta + \theta_{n2})) = \frac{1}{-\omega^2 - 2i\nu\omega + 2\sin^2\theta k_0^2 c_s^2 + \cos^2\theta(\sin\theta_{n_1} - \sin\theta_{n_2})^2 k_0^2 c_s^2}\,,$$

$$= \frac{1}{-2i\nu\omega + \cos^2\theta(\sin\theta_{n_1} - \sin\theta_{n_2})^2 k_0^2 c_s^2}\,. \tag{6.41}$$

As in the case without diffraction, the resonance between the IAWs and the crossing envelopes leads to a smaller wave amplitude.

Effect of the damping rate on the energy exchange

Fig. 6.4 (top) exhibits the ratio between the wavelength shift case and the plane wave case versus the Landau damping rate. The energy exchange is calculated at resonance, in the asymptotic regime, for different numbers of phase plate elements.

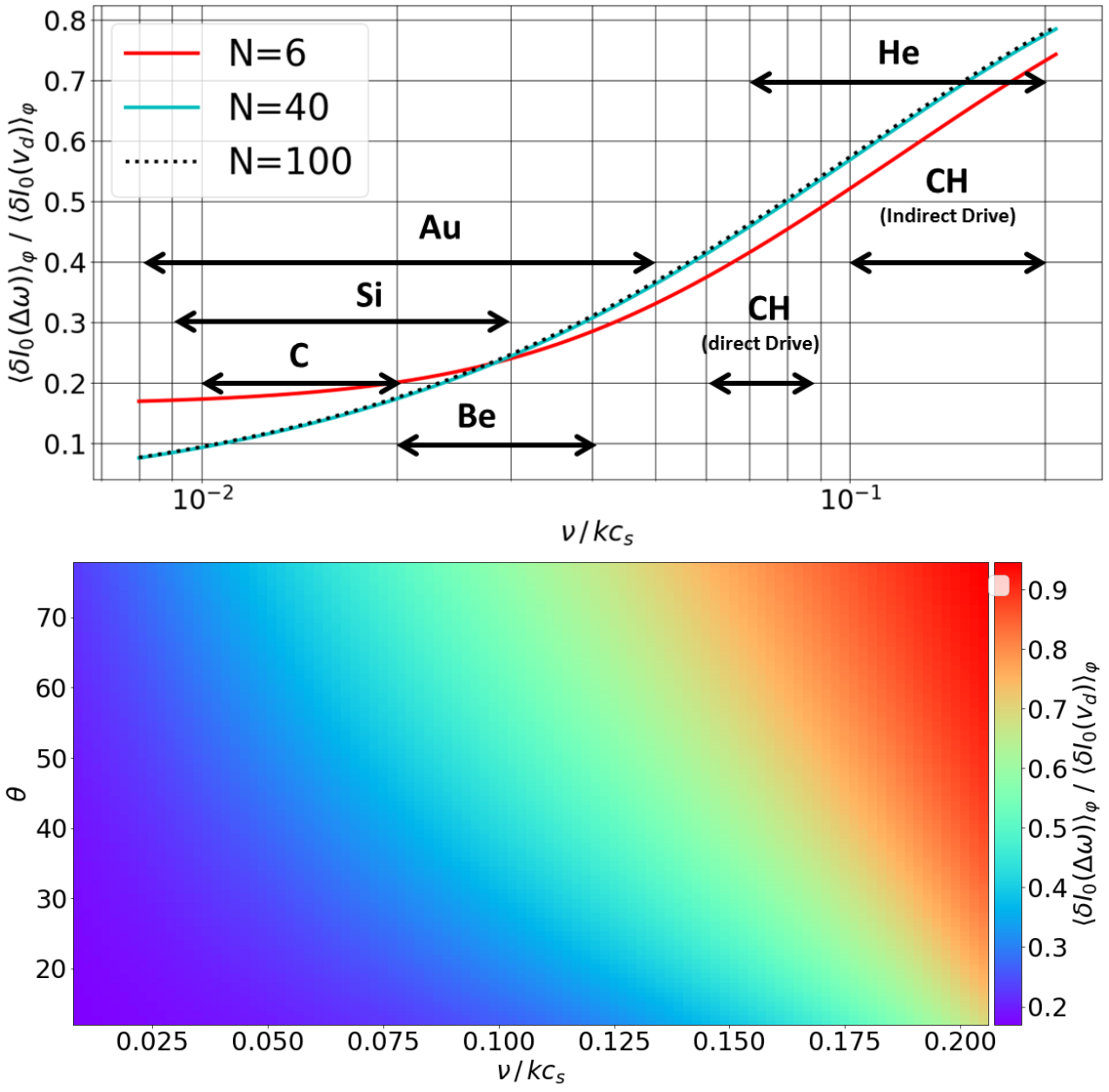

Figure 6.4: (top) Semi-log plots of the resonant $\langle \delta I_0 \rangle_\varphi$ calculated with Eq. (6.20) in the wavelength shift case ($\omega = kc_s$) normalized to the plasma flow case ($v_d = c_s$) against the damping rate, for a crossing angle of 24°. (bottom) Same ratio, in a linear scale, against the crossing half-angle (varying from 12° to 78°) and the damping rate, for N=6.

The laser amplitudes are $a_0 = 0.004$, the half-angle of the (top) panel is $12°$, the plasma density is 0.04, T_i varies from 0.5 to 1 keV and T_e from 2 to 3 keV. These parameters will match the ones chosen in the simulation of Section 6.3. The laser amplitudes, angles, and the plasma density and temperatures match those of the simulations. The damping is varied to illustrate the different interaction regimes. The order of magnitude of this parameter is indicated for a few plasmas relevant to ICF such as the gold bubble in indirect drive configuration, the CH with NIF parameters, the CH in reduced scale facilities such as Omega, carbon, helium and the higher Z ablators silicon and beryllium [26, 34]. The range of the damping rates includes the effect of electron-ion and ion-ion collisions, as explained in Section 4.1.2. For Au (Si), the plasma collisionality may increase the damping rate up to ~ 0.05 (~ 0.03) depending on the cone angle and local plasma parameters. The damping rate was also calculated for CH_4, and the value is found to be identical as for CH, regardless of the parameters, so it is not written on 6.4 (top). In the weakly-damped regime, for gold, carbon or silicon plasmas, a decrease of more than 80% of the exchange is observed for the wavelength shift case compared to the plane wave case. Because the damping distance is greater than the distance between the crossed speckles, the driven wave with a frequency shift is substantially reduced due to destructive interferences as demonstrated in Chapter 5. For intermediate damping rates, as for beryllium plasmas, the difference persists. For strong damping rates, as for He and CH plasmas, a difference of $\approx 25\%$ (indirect drive) and 50% (direct drive) remains. Even though the damping prevents IAWs from interacting, the damping distance is comparable to the speckle size, so the driven IAW still differs from the plane wave case. Even for very large damping rates (> 0.2), all considered situations are not equivalent, hence demonstrating the invalidity of the plane wave approximation. Figure 6.4 also exhibits the ratio between the wavelength shift case and the plane wave case versus the crossing half-angle. The energy exchange is calculated at resonance, in the asymptotic regime, for six phase plate elements. θ is varied between $12°$ and $90 - 12°$. We recall that $k = 2k_0 \sin\theta$. This dependence on θ implies that for a constant value of ν/kc_s, both k and ν are varying with θ. The ratio gets closer to one, i.e. cases get comparable, as the angle is increased. Indeed, the damping rate, $\propto \sin\theta$, increases with the angle. For this reason, discrepancy between cases fades away when θ is increased. As argued in Section 6.1.1, an angle close to 0 or 180 will lead to a great increase of the crossing zone and therefore of the exchange.

Spectrum of the resonance condition

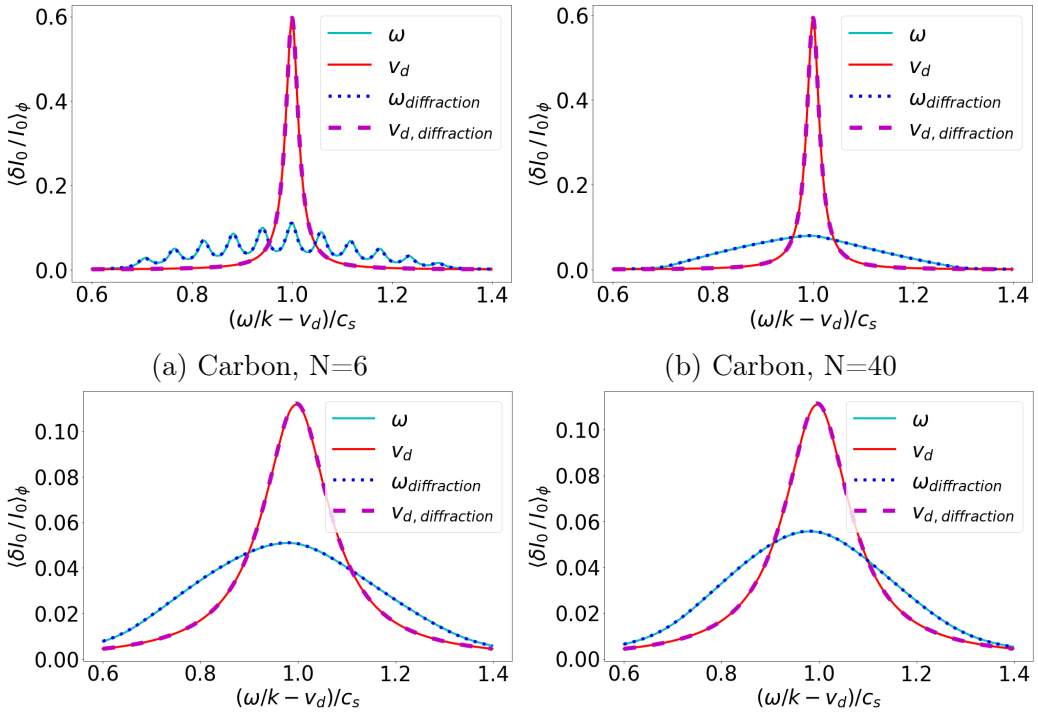

(a) Carbon, N=6 (b) Carbon, N=40

(c) CH, N=6 (d) CH, N=40

Figure 6.5: Amplitude of $\langle \delta I_0/I_0 \rangle_\varphi$ over a distance of $2\pi 6 f_\#/\sin 2\theta$ versus the deviation to resonance for plasma flow case (red curves) and wavelength shift cases (cyan curves) with diffraction (dotted lines) and without (plain lines) for the carbon and the CH, for 6 or 40 elements of the phase plate.

Figure 6.5 illustrates the dependence of $\langle \delta I_0/I_0 \rangle_\varphi$ on $(\omega/k - v_d)/c_s$ that is to say the deviation from the resonance. $\langle \delta I_0/I_0 \rangle_\varphi$ represents $\delta I_0/I_0$ averaged over φ and calculated over a distance of $2\pi 6 f_\#/\sin 2\theta$. As the model neglects the beam depletion, the amount of exchanged power is proportional to the distance along which the exchange is computed. As a result, the exchange for a beam passing through a N=40 elements RPP exhibits almost seven times more exchange than a N=6 elements RPP. To properly compare different cases, the exchange is computed along the same distance regardless the RPP elements number. The latter is fixed to $L = 2\pi 6 f_\#/\sin 2\theta$, corresponding to the beam length of the forthcoming simulations. The cases represented are the plasma flow (red) and the wavelength shift (cyan), for Carbon (a), (b) and CH (c), (d). Calculations are performed for 6 elements of the phase plate (a), (c), and 40 elements (b), (d). The amplitudes of the normalized wavelength shift case at resonance

are the same as in Fig. 6.4. Yet, for the wavelength shift case, N-1 peaks are found out of resonance. Those peaks are located at $\omega/(k \pm k_\perp) = c_s$ for the case without diffraction, and at $\omega/k_0(\sin(\theta + \theta_{n1}) - \sin(-\theta + \theta_{n2})) = c_s$. These resonances are due to the beating between the IAW induced by the grating and the IAWs induced by the speckles envelope. For realistic phase plate number RPP beams, the randomness of the speckles position involves a wide range of wave vectors, and results in a broadening of the resonance bandwidth, instead of additional peaks. This explains why the peaks are discernible in the N=6 case and not in the N=40 case. For the CH case, because the IAWs are damped before reaching an other SC, there is no resonance with the envelope. For this reason, Fig. 6.5 (c) does not exhibit peaks as Fig 6.5 (a). Finally, no difference is discernible between the cases with and without diffraction because of the unchanged crossing zone size, as predicted in Section 6.1.1. Diffraction is therefore negligible for 2D RPP CBET studies when considering angles $\theta \gg 1/f_\#$ and $\theta \ll \pi/2 - 1/f_\#$. In 3D, the probability for an infinite longitudinal speckle to cross an other speckle is still very high and close to 1. For a finite size, it is less evident. Discrepancy between these cases is expected in 3D, the case with diffraction includes less crossing zone and therefore less exchange.

6.2 Cross-Beam Energy Transfer simulations: Academic configuration

Most parameters are the same as in 5.2.1. The configuration is shown in Fig. 6.6. The simulations setup consists in two beams, each composed of four equally spaced speckles, crossing each other. Compared to real spatially smoothed beams addressed in the following part, this simplified configuration allows to compare the results with the plane wave case while having a perfect knowledge of the amplitudes and the phase shifts between the waves. Figure 6.7 plots the normalized profile of the laser intensity, and of the electron density perturbation $\delta N_e/n_{e0}$, along y. In a stationary plasma with a wavelength shift [Fig. 6.7(a)], the propagating IAWs are clearly visible and have time to reach the next crossing regions due to the small damping rate. When there is a plasma flow, but no frequency shift, the IAWs are stationary in the lab frame, as shown in Fig. 6.7(b). The amplitude of the density perturbation is weaker when the plasma is stationary, because the propagating wave does not have the time to locally grow. Moreover, the phase shift between waves created in the vicinity of different crossing regions may decrease the total IAW amplitude, exacerbating the disparities with the plasma flow case. From

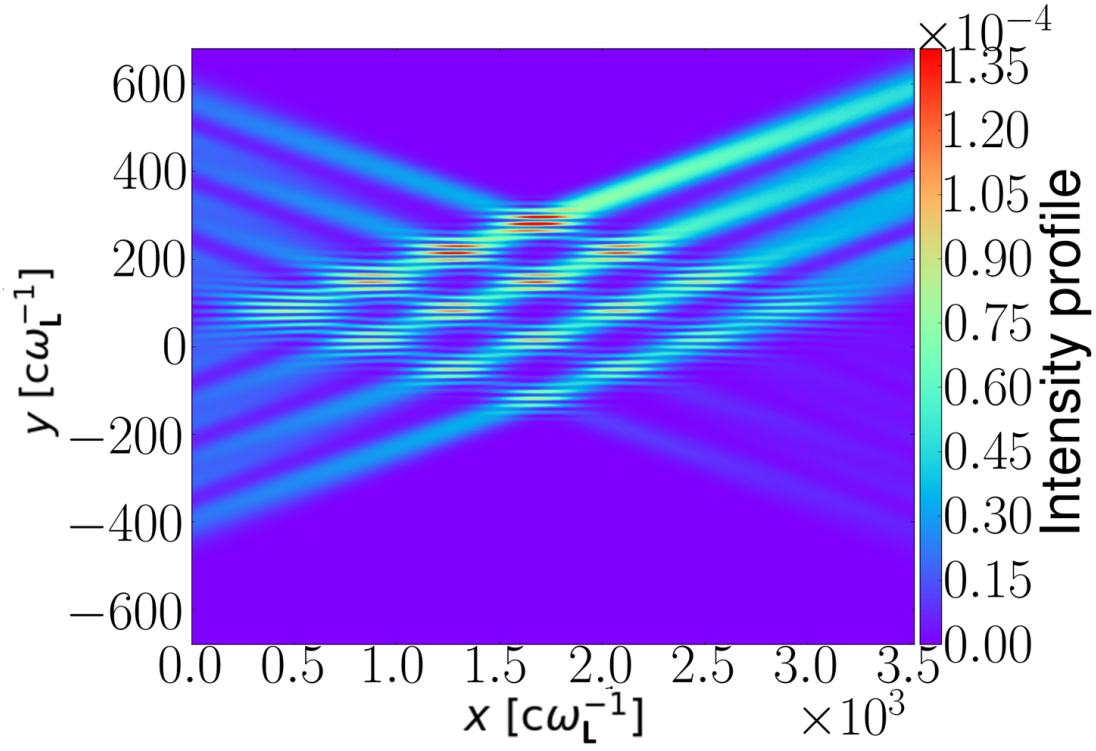

Figure 6.6: Intensity profile normalized to $2.74 \times 10^{18}/\lambda_{\mu m}^2\,\mathrm{W\ cm^{-2}}$ at time $3.4 \times 10^5\,\omega_L^{-1}$ for the plasma flow case.

these different IAW amplitudes, we anticipate a substantial difference in the energy exchange. We checked this numerically by performing several simulations, with or without plasma flow, and with various phase shifts between the SCs. Because the waves are weakly damped, we could not reach the asymptotic regime in our simulations. Hence, our results are only for the transient regime. Figure 6.8 (a) compares the gain/loss of linear power of the upper/lower escaping beams for different laser and plasma parameters. The red diamonds correspond to the temporal plane wave model inspired from [18] and presented in 4.3 and show a satisfactory correspondence with the plasma flow case. At resonance, the exchange in energy is 20% larger when there is a plasma flow case (dotted line) than when there is a wavelength shift case (dashed-dotted line). This difference is further increased beyond 100% by adding a phase shift between the SCs (dashed line). It is worth pointing out that the upper beam is significantly depleted in the plasma flow case, thereby limiting the inner beam power growth. For smaller intensities, the disparities between the three cases would be even more pronounced. Despite this intrinsic difference in the IAW growth shown in Fig. 6.7, the energy exchange due to a plasma

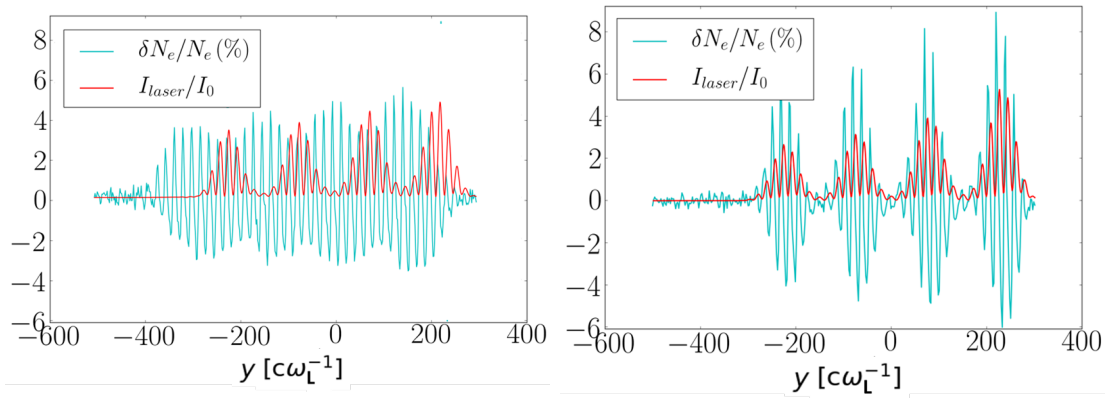

Figure 6.7: Percentage of electronic wave perturbation (cyan) and normalized laser intensity (red) as a function of y and averaged from x = 1600 to x = 1800 $c\,\omega_L^{-1}$ in the laboratory frame at $t = 2.71 \times 10^5\,\omega_L^{-1}$ for the wavelength shift case (a), and for the plasma flow case (b).

flow can be cancelled out by adding a frequency shift ($\omega/k = c_s$ and $v_d = c_s$) as illustrated by the black curve in Fig. 6.8 (a). Indeed, out of resonance the IAW amplitude is very small. To study the resonance bandwidth, the exchanged power is plotted in Fig. 6.8 (b) for one out-of-resonance plasma flow case, and three values of ω/k for the wavelength shift case. For a flow velocity, $v_d = 0.905\,c_s$, the transient exchange oscillates around zero, before vanishing at long times, in a similar way as in Fig. 2a of Ref. [18]. As explained previously by the linear model, the solution behaves like in the plane wave case, for which the resonance bandwidth of the weakly-damped plasma is thin. By contrast, the exchange persists in the wavelength shift case. The different values of ω/kc_s (0.88, 0.905 and 0.93) are chosen so as to explore the resonance bandwidth. The comparable amount of power exchange in the three cases suggests a larger resonance bandwidth than in the plasma flow case. This peculiar tendency has been explained with our model in Section 6.1.3: in the wavelength shift case, the IAW propagates and can be resonant with the SC envelope, broadening the resonance spectrum.

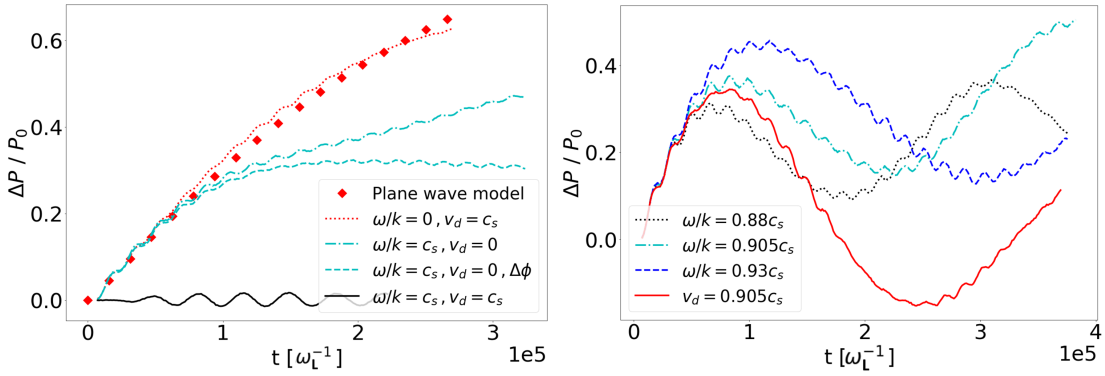

(a) (b)

Figure 6.8: Difference between the linear power of the upper and the lower beam versus time. Panel (a), at resonance for the plasma flow case in red (dotted line), the wavelength shift case in cyan, with (dashed lines) and without (dashed-dotted line) phase shift, and out of resonance in black (plane line) ; Panel (b), out of resonance for the plasma flow case (plane red line) and for the wavelength shift case for three values of ω/k corresponding to three different near-resonance conditions in cyan, blue and black.

6.3 Cross-Beam Energy Transfer simulations: Realistic Random Phase Plate configuration

6.3.1 Parameters

Smilei PIC simulations [19] of CBET with realistic RPP beams have been performed to confirm the relevance of our previous results, and to further investigate the strongly damped regime. Normalizations are the same as in 5.2.1 and the configuration is shown in Fig. 6.10.

Numerical parameters

The box size is $L_x \times L_y = 2412 \times 1206\, c^2\, \omega_L^{-2}$, with cells size of $0.7 \times 0.7\, c^2\, \omega_L^{-2}$. Cells are filled by 20 ions of each species and 20 electrons. One simulation is performed with a single species (Carbon, Z=6) and the other one with two species (CH). The time step is $0.45\, \omega_L^{-1}$. For the wavelength shift case, boundary conditions are reflective for the plasma, and absorbing (Silver-Muller) for the fields. For the plasma flow case, x_{min} and x_{max} boundary conditions are reflective for the plasma and absorbing (Silver-Muller) for the fields, and y_{min} and y_{max}

boundary conditions are periodic for both the plasma and the fields.

Plasma parameters

The simulations are performed in a homogeneous and non collisional plasma as justified in 5.2.1, and the plasma is fully ionized. Two different plasmas are considered: carbon (C) for the weakly-Landau damped case and a plastic ablator (CH) for the strongly-Landau damped case. For these species, the fluid limit incorrectly approximates the value of the IAW velocity as well as the damping. Thus the calculation is made by graphically resolving the sound kinetic dispersion relation as explained in Section 4.1.1 and we obtain a damping distance of $141\, c\,\omega_L^{-1}$ for the C and $28\, c\,\omega_L^{-1}$ for the CH [117] respectively corresponding to damping times of $1.2\times10^5\,\omega_L^{-1}$ and $2.4\times10^4\,\omega_L^{-1}$. The electron and ions temperatures are $T_e = 2\,\text{keV}$ and $T_i = 1\,\text{keV}$, respectively. The electron density is fixed to $n_e = 0.04\, n_c$.

Laser parameters

Two RPP beams are crossing at an angle of $24°$. The initial condition for each beam is the exact solution of the field of a paraxial beam passing through a spherical lens and a random phase plate composed of small elements adding a phase shift of 0 or π. As explained in Section 6.42, the field set as initial condition can be deduced from the 2D inverse FT of the field at focal spot, but the numerical cost of such a calculation at each timestep is too high. Knowing the exact field everywhere allows to give the analytical expressions of two RPP beams with an angle as initial conditions. The calculation is shown in Chapter 3 and leads to

$$E = \frac{E_l}{2}\sqrt{\frac{f}{f-x}}e^{\frac{iky^2}{2(f-x)}}\sum_n e^{i\varphi_n}\times\left(\text{erf}\left[e^{-\frac{i\pi}{4}}K(x)\cdot(a_{n+1}-\frac{yf}{f-x})\right]-\text{erf}\left[e^{-\frac{i\pi}{4}}K(x)\cdot(a_n-\frac{yf}{f-x})\right]\right), \tag{6.42}$$

valid for $x < f$. $a_n = nd$ where d is the size of one phase plate element, $n \in [-N/2, N/2]$ where $Nd = D$ is the size of the phase plate, and $K(x)^2 = \frac{k}{2x} - \frac{k}{2f}$ where f is the focal length. The field given as x_{min} boundary initial condition is $E_{tot} = E_0 + E_1$ where $E_{0,1}$ are the field of a beam as described in eq (6.42) with an angle $\theta_0 = \theta\,, \theta_1 = -\theta$. The laser field is normalized in order to later choose the laser intensity so the pre-factor of Eq. (6.42) does not play a role in our simulations. However, as the beams field is enveloped, all the energy is contained in the simulation box and this normalization does not change the speckles intensity distribution. The laser pulses propagate from the left to the right. The temporal evolution is a ramp of $2000\,\omega_L^{-1}$

followed by a plateau until the end of the simulation. The focal spots of the RPP beams are located in the middle of the simulation box and their intensity is $I = 8.8 \times 10^{13}\,\mathrm{Wcm}^{-2}$ corresponding to a = 0.004 or $I = 2.2 \times 10^{13}\,\mathrm{Wcm}^{-2}$ corresponding to a = 0.002, for the study of the resonance spectrum. The simulations are made with $N = 6$ and $f_{\#} = 8$ which corresponds to a beam waist of $w = 48\,\lambda_L$ where $\lambda_L = 1\mu m$.

The frequency shift is chosen so as to match the resonance condition $\omega = kc_s = 4.535 \times 10^{-4}\,\omega_L$ the lower beam having the lowest frequency ($= 1 - 4.535 \times 10^{-4}$) for the CH and $\omega = kc_s = 4.79 \times 10^{-4}\,\omega_L$ for the C.

6.3.2 Simulations results

In this section, the difference of power exchange between plasma flow and wavelength shift cases is investigated assuming RPP beams in both weakly and strongly Landau-damped plasmas. Unlike in 6.2, distinction is not made between the in-phase and out-of-phase cases as this realistic phase plate does not permit to control the phase of the gratings. Due to the randomness of the speckles generation, the phase-shift is inherently included between the different gratings. As in Chapter 5, the exchange is calculated with the difference between the power of the red-shifted / blue shifted, obtained by integrating the Poynting vector at x_{max} over the upper ($y > 0$) / lower ($y < 0$) half of the simulation box shown in Fig. 6.10.

At resonance

First of all, the power exchanged of a RPP plasma flow case is compared to a nearly plane wave case in order to confirm the equivalence between those cases, already theoretically demonstrated in 6.1.3. The plane wave case corresponds to a simulation of the exchange between two Gaussian beams having the same a_0 and same linear power as the RPP beams. The simulation is also performed with a plasma at a velocity v_d along y.

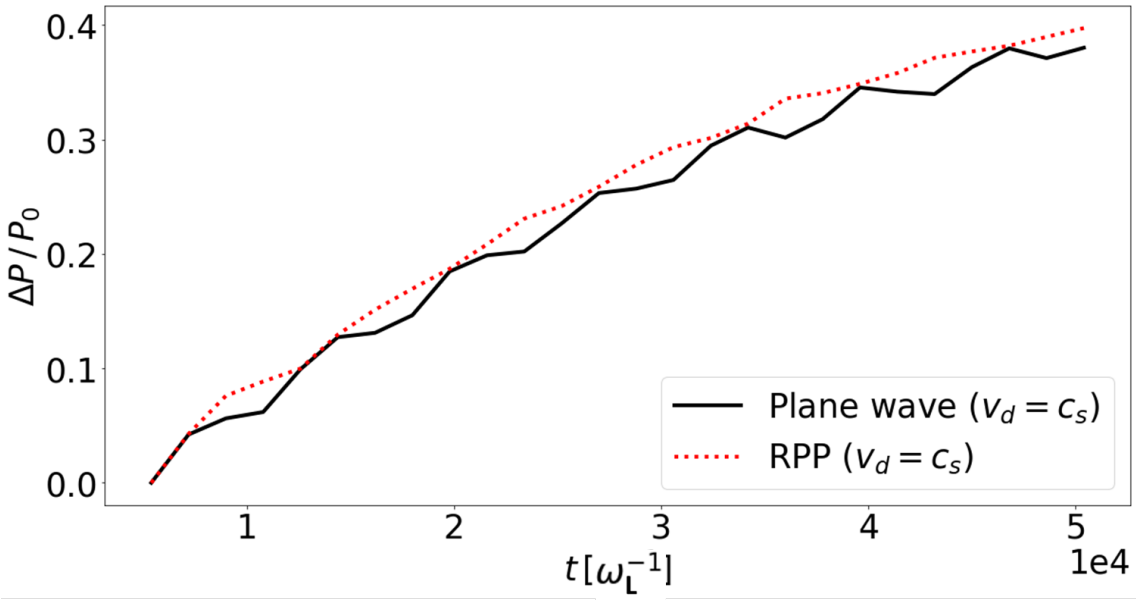

Figure 6.9: Difference between the power per unit length of the red-shifted and the blue-shifted beams escaping the simulation box normalized to the initial power versus time, for a = 0.004. The Gaussian beam simulation is represented in dark solid line, and the RPP case in red dotted line. Both cases include a plasma flow v_d.

In Fig. 6.9, the red dotted curve corresponds to the RPP case as represented in Fig. 6.10 and the plain dark curve corresponds to the plane wave case. The almost merged curves strongly support our theoretical deductions.

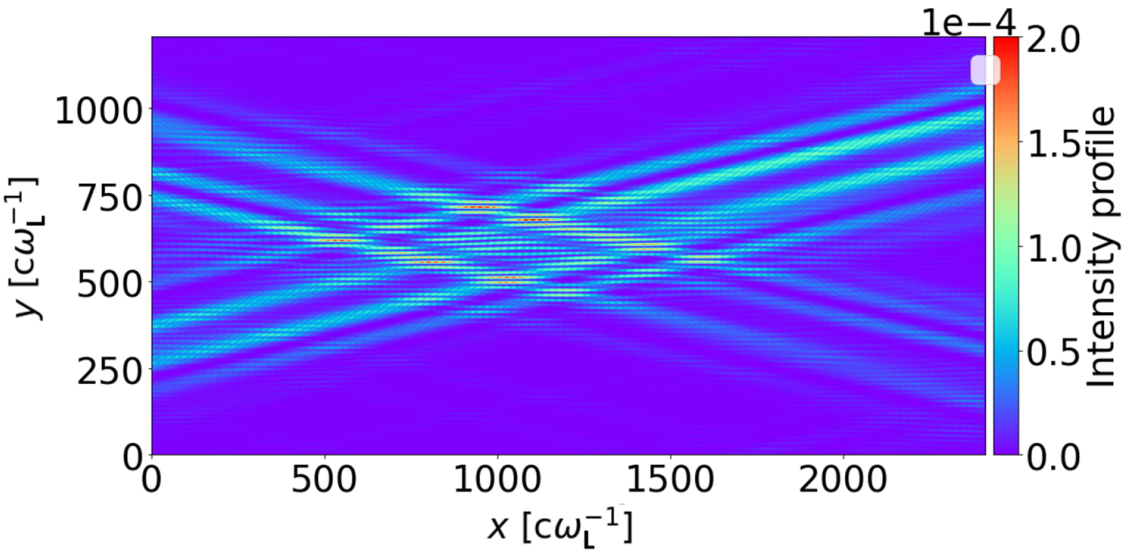

Figure 6.10: Intensity profile normalized to $2.74\times10^{18}/\lambda^2_{\mu m}$ W cm^{-2} at time $10^5\,\omega_L^{-1}$, for a $= 0.004$, for the carbon plasma flow case, with a number of phase plate elements of $N = 6$.

This being clarified, the RPP configuration of the simulation is now shown. The intensity profile for the carbon plasma flow case is plotted on fig. 6.10. The exchange is clearly discernible, the blue-shifted beam seeming to be almost depleted. Some speckles with very low intensities are also discernible, due to the airy disk coming from the sinus cardinal form of the focal spot. Figure 6.11 exhibits the amount of exchanged power between the upper right and the lower right beam versus time for both carbon and CH plasmas. At $t = 5 \times 10^4\omega_L^{-1}$, the exchanged power observed in the wavelength shift case is reduced by 45% compared to the flow case in the carbon plasma, and by 30% in the CH plasma. This confirms the validity of the model even for strongly Landau-damped plasmas. For the CH, the damping distance is comparable with the speckle size ($c_s/\nu\lambda_{sp} \sim 0.5$), and the amplitude of the driven IAW stems from the ponderomotive force averaged over half the CS. It is worth noting that the simulations correspond to the case $k_{max} = 0.15\,k$, i.e the NIF/LMJ condition.

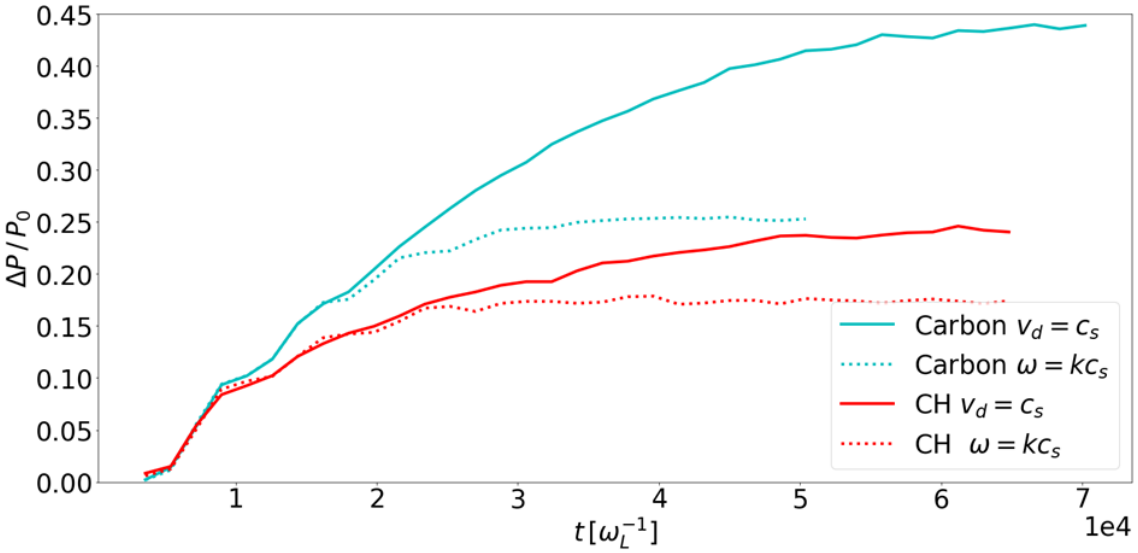

Figure 6.11: Difference between the power per unit length of the upper right and the lower right beam normalized to the initial power versus time at resonance for a $= 0.004$. Plasma flow cases and wavelength shift cases correspond to the plane lines and the dotted lines, respectively. Weakly Landau-damped cases (Carbon) are in cyan, and strongly Landau-damped cases (CH) are in red.

Out of resonance

The comparison between the plasma flow and the wavelength shift cases out of resonance, theoretically studied in Section 6.1.3 and numerically in the academic situation of 6.2, is now explored for carbon and CH plasmas in the case of RPP beams. Figure 6.12 exhibits the exchanged power versus time for the carbon plasma flow and wavelength shift cases out of resonance at $\omega = 0.85\, kc_s$. As predicted by the model, the exchange for the wavelength shift case becomes stronger than the plasma flow case, unlike in the resonance case. The same resonance condition and an even more amplified resonance mismatch ($\omega = 0.70\, kc_s$) have been applied in the CH plasma. The discrepancy between cases is smaller for CH, and was not visible yet for $\omega = 0.85\, kc_s$. In Section 6.1.3, we saw that the resonance bandwidths are larger in CH. For this reason, we had to go further from resonance to see the tendency reversing. These simulations have been performed until seeing the expected tendency, but they have not reached the asymptotic regime. Having this general tendency confirmed by our RPP simulations, it is now interesting to explore the resonance bandwidth shape. The model predicts a thin resonance bandwidth in the carbon plasma in the plane wave case, and a wide bandwidth for the other cases. Several simulations in both carbon and CH plasmas, have been performed to explore

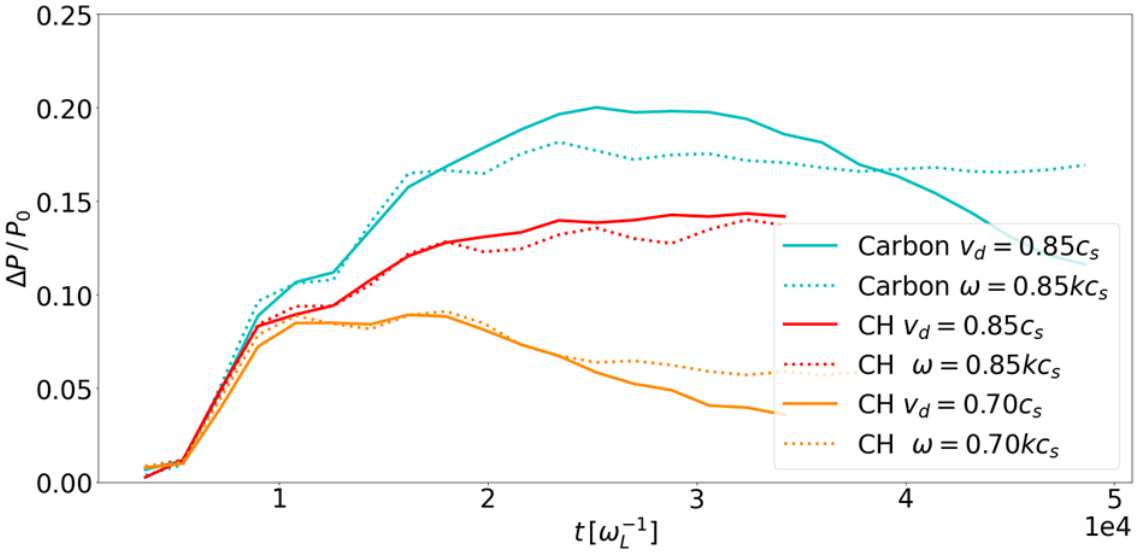

Figure 6.12: Difference between the power per unit length of the upper right and the lower right beam normalized to the initial power versus time out of resonance for a = 0.004. Plasma flow cases and wavelength shift cases correspond to the plane lines and the dotted lines, respectively. Weakly Landau-damped cases (Carbon) are in cyan, and strongly Landau-damped cases (CH) are in in red.

the resonance bandwidth. The beam intensity has been divided by a factor 4 so as to avoid the beam depletion that would otherwise bound the final beam power at resonance. Since the exchange rate is proportional to the laser intensity, we also expect a factor 4 between the power exchange of the previous simulations and these ones. Figure 6.13 shows the value of the normalized exchanged power at asymptotic time in the carbon and CH plasmas for different deviations from resonance. The values on the right side ($(\omega/k - v_d)/c_s = 1$) correspond to the case at resonance. The exchange is not the same because the initial power is reduced, but the ratio between the plasma flow and the wavelength shift cases are the same as in Fig. 6.11. A clear and noteworthy qualitative accordance is still found between the model and the simulations. As expected from the model in Fig. 6.5 and the first simulations out of resonance in Fig. 6.12, the wavelength shift case becomes predominant after a certain deviation from resonance. The resonance bandwidth is also thinner in the Carbon and plasma flow cases. Although we performed many simulations for the Carbon wavelength shift case to explore the resonance bandwidth, the supernumerary peaks of Fig. 6.5 (a) are not discernible. The number of RPP N=6 is the same, but the model only accounts for six SCs while the exchanged power in the simulation results from all the SCs in the crossing zone. Figure 6.10 shows $\simeq 10$ intense SCs and a few less intense, explaining the flattening of the resonance curve. However, a significant

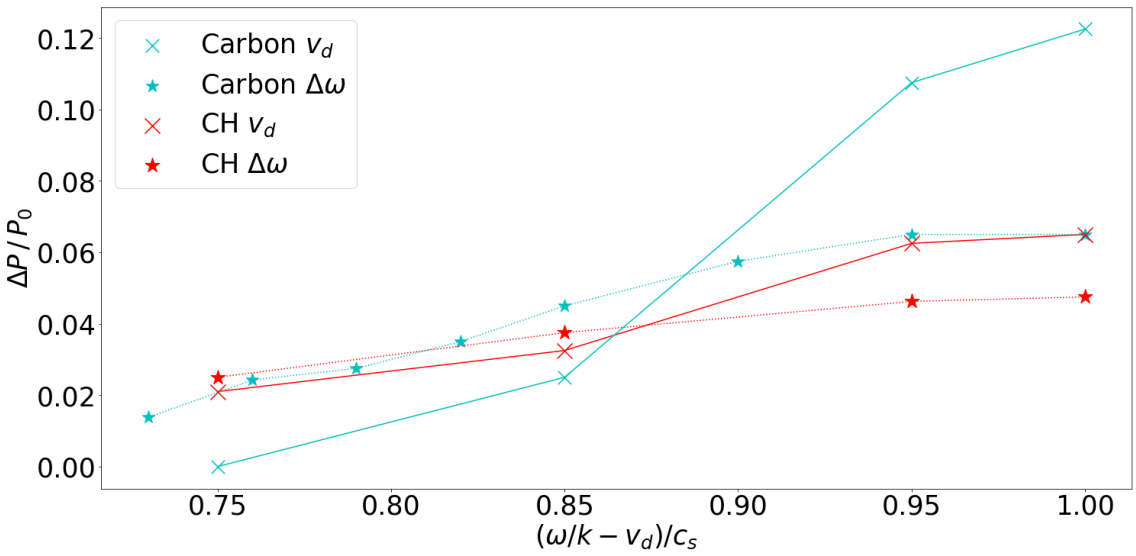

Figure 6.13: Scatter plots of the normalized exchanged power for a = 0.002 versus the deviation to resonance, for the Carbon (cyan) the CH (red), for the plasma flow case (solid lines with crosses) and the wavelength shift case (dotted lines with stars).

gap is found between the maxima of the resonance curves of the model in Fig. 6.5 and the simulation in Fig. 6.13. The model strongly over-estimates the exchange, even without laser depletion. In Sections 4.1.1 and 4.1.2, we have shown that theoretically, Landau damping is the prevailing damping process and that the effect of collisions can be neglected in both C and CH. To confirm this assumption, simulations taking collisions into account were performed. Figure 6.14 exhibits the power exchanged for the Carbon, plasma flow and wavelength shift at resonance, with and without collisions. The choice of the species as well as the resonance was made to study the effect of collisions in the case where they are the more susceptible to affect the exchange. As they do not seem to have an effect in this worst case, we can anticipate that they also have no effect for species with a bigger Landau-damping distance and further from resonance. These simulations therefore confirm the relevance of neglecting collisions in all the previous simulations.

To conclude, these results can partially explain why the experiments often differ from the models and simulations in indirect-drive approach. Furthermore, owing to the frequency shift induced by a moving plasma [20], this effect probably holds true in the direct-drive approach. Alas, most CBET measurements are indirectly made by measuring the symmetry of implosion, which is subsequently reproduced in the simulation by artificially saturating the density perturbation [39, 47]. This lack of direct experimental measurements complicates any quantitative comparison

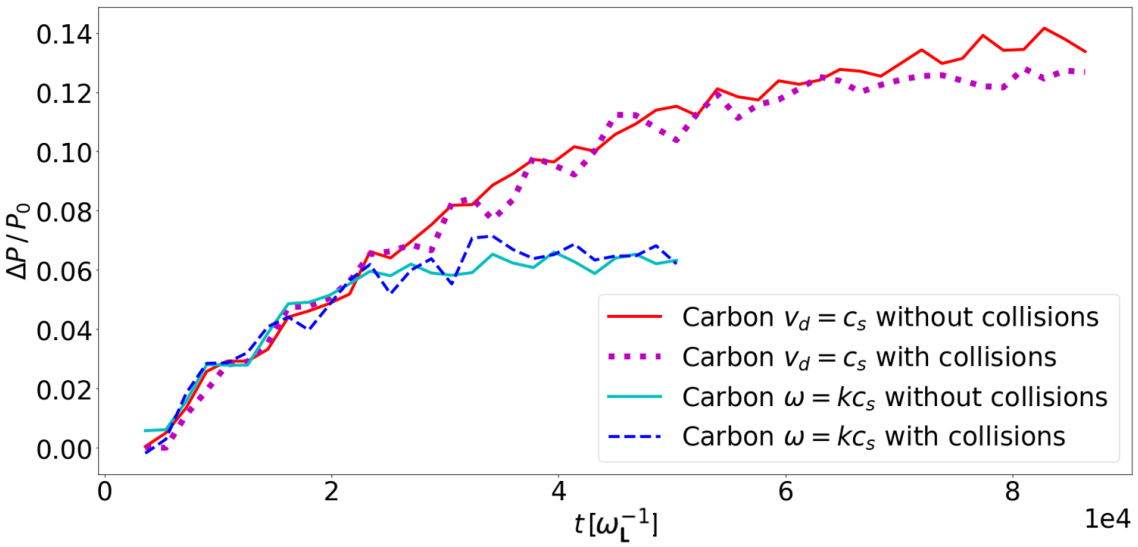

Figure 6.14: Difference between the power per unit length of the upper right and the lower right beam normalized to the initial power versus time at resonance for a = 0.002 and a Carbon plasma. Plane wave case is in solid red line without collisions, dotted magenta line with collisions, and wavelength shift case in solid cyan line without collisions, dashed blue line with collision.

with our models/simulations.

Only 2D cases were studied, but multiplicity as well as proximity of the speckles suggest that many SC are found in a beam section, meaning the observed exchange difference also exists in 3D. SC are however expected to be fewer, which will result in a reduced effect of the interferences in the case of weakly-damped plasmas. However, the discrepancy from the plane wave model still remains in strongly damped-plasmas. There, the diffraction effect is negligible and 3D PIC simulations would lead to roughly the same conclusions.

Conclusion and perspectives

The main innovations of this work are

- The theoretical and numerical demonstration of the difference between the CBET due to the wavelength shift of the laser beams and CBET due to a plasma flow
- The use of a realistic RPP field to establish a linear exchange model.

We have investigated the CBET between many speckles, by means of kinetic PIC simulations and a linear model.
The IAW produced by a flowing plasma is found to be stationary. Since the interference grating is also stationary in the laboratory referential, the IAW remains in the location where it was created and is therefore stimulated by the same potential. For this reason, the plasma flow case can be assimilated to a plane wave case.
When the laser beams have different frequencies in the lab frame, the random phase shift between the interference gratings, situated at each crossing speckles, is an important factor of energy exchange inhibition. Indeed, the driven IAWs issued from each crossing speckles, can interfere destructively, thereby reducing the light scattering by the ion gratings. This effect is particularly efficient in weakly damped plasmas where the IAWs can travel through many speckles.
In strong Landau damped plasma, such as plastic CH, an inhibition of CBET persists, with values around 30 % compared to the plane wave limit. When the damping distance is comparable with the speckle transverse size, the ponderomotive force producing the moving grating in the plasma reference frame is averaged over the speckle, thereby reducing the amplitude of the driven IAW. This demonstrates that the difference between the plasma flow and the wavelength shift case is not only due to the phase-shift effect.

All the aforementioned phenomena were first found using academic simulations in which the laser beams were constituted of four Gaussian speckles. These findings were explained with a simplified model using a sinusoidal envelope for the beat wave ponderomotive force. These toy models allowed us to precisely control every parameter and to identify the phase shift effect as well as the IAW dynamics. Then, these results were confirmed in a more realistic case. The linear model has been improved considering the exact expression of the envelope of a beam having undergone a RPP. Likewise, PIC simulations were performed with the RPP field, known everywhere.

These results can partly explain why the experimental exchange is often over-estimated in the simulations in the indirect-drive approach, when using different laser frequencies. The speckles structure of the beam being inherently present, its effect is prior to any non-linear mechanism usually invoked as CBET saturation. Moreover, as the cross section between the beams/speckles becomes larger for crossing angles close to 0 or π, the plane wave approximation becomes even further away from reality. It is therefore even more important in these cases to account for the speckle structure and to use a RPP model.

Most perspectives of this work stem for the RPP modelisation. First, the presented 2D model can easily be extended in 3D. Then, as temporal smoothing involves plane waves, no particular difficulty is foreseen in including SSD in the model. These prospects are achievable in both a linear model and PIC simulations, and can also be enlarged in hydrodynamic simulations.

Appendix A

Simulations specifications

This appendix aims to summarize the simulations parameters such as the inputs and the details on how to plot the figures, so that the reader has a better understanding and has enough information to reproduce the results.

A.1 PIC simulations with CALDER

A.1.1 Parameters

We first recall the input parameters described in the Sections 5.2.1 and 6.2

Numerical parameters

- Box size: $L_x \times L_y = 8000 \times\ 3200\, c^2\, \omega_L^{-2}$
- Mesh size: $0.44\ \times 0.44\, c^2\, \omega_L^{-2}$
- Timestep: $0.3\, \omega_L^{-1}$
- Cells are filled by 20 macro-ions and 20 macro-electrons
- Boundary conditions: reflective for the plasma and absorbing for the fields for the wavelength shift case. Periodic for the plasma and absorbing for the fields for the plasma flow case.

- High mode current filtering
- 4th-order alternating interpolation scheme

Plasma parameters

- Homogeneous and non collisional plasma
- Electron density: $0.04\, n_c$
- Ion species: $A = 160$, $Z = 10$
- T_i: $1\,$keV
- T_e: $4\,$keV
- Plasma flow velocity at resonance (for the plasma flow case): $5.35 \times 10^{-4} c$
- Application of 3 filters to smooth the current deposited by the macro-particles

Laser parameters

- Four Gaussian beams intersect four other Gaussian beams
- Crossing angle: $20°$ (beam 0 : $\theta_0 = 10°$, beam 1 : $\theta_1 = -10°$)
- Polarization: linear (electric fields lying in the (x-y) simulation plane)
- The laser pulses propagate from the left to the right
- Temporal evolution: ramp of $1000\, \omega_L^{-1}$ followed by a plateau until the end of the simulation
- The focal spots of the eight speckles are located in the middle of the simulation box
- Intensity: $I = 8.8 \times 10^{13}\,$Wcm^{-2} ($a_0 = 0.008$)
- (equal) beam waists at $1/e$: $w = 70\, c\, \omega_L^{-1}$ ($11\,\mu$m for $\lambda = 1\,\mu$m) at FWHM
- Distance between speckles: $\Delta y = 150\, c\, \omega_L^{-1}$
- Frequency shift at resonance (for the wavelenght shift case): $\omega = k c_s = 1.81 \times 10^{-4}\, \omega_L$, the lower beams having the lowest frequency ($= 1 - 1.81 \times 10^{-4}$)

- Field of a speckle $\equiv$ field of a Gaussian beam at focal spot: $E = E_0\sqrt{\frac{w_0}{w(x)}}e^{-i\frac{1}{2}\arctan x/x_r}e^{\frac{ik_0y^2}{2R(x)}}e^{-\frac{y^2}{w(x)^2}}e^{i\phi}$ given in a θ-shifted plane with respect to y in the middle of the simulation box.

- Phase: (bottum up) $\phi = 0,\ 0.4,\ 4.5,\ 0.2$ for the upper beams ($y > 0$) and $1,\ 0.1,\ 0.9,\ 5$ for the lower ones ($y < 0$) for the phase shift case, all phase are equal to for the in phase case

A.1.2 Results and figures plotting details

- Intensity map (Fig. 5.3 and 6.6): The output of the B_z field is made each 4000 timestep, and is averaged over a laser period (20 timesteps). The intensity map is the plot of the averaged field B_z^2.

- Exchanged power vs time (Fig. 5.4 and 6.8): $\Delta P/P_0$ is the power per unit length of the four escaping red-shifted speckles (Gaussian beams) minus the power of the four blue-shifted speckles, normalized to the initial power per unit length. The power of the red-shifted / blue shifted beam has been obtained by integrating the Poynting vector (*i.e.* B_z^2) at x_{max} over the upper ($y > 0$) / lower ($y < 0$) half of the simulation box. The values of each output are plot, that is to say each 4000 timesteps.

- (y-t) density map (Fig. 5.5 (a) and (b)): The density perturbation for one timestep correspond to the averaged value of the density over x and over $200\,c\omega_L^{-1}$ and is plotted as a function of y. The averaging over x on a distance smaller than the crossing length allows a better resolution. The simulations output ar every 4000 timesteps.

- Envelope amplitude vs time (Fig. 5.5 (c)): To obtain the two curves, the value of n_e is found by reporting the values of n_e along the direction $y_0 + c_s t$.

- Electronic wave perturbation and normalized laser intensity vs y (Fig. 6.7): As for the (y-t) density map, the density perturbation is averaged over x to obtain a better resolution. The laser intensity is the value in the middle of the simulation.

A.2 PIC simulations with SMILEI

A.2.1 Parameters

We firt recall the input parameters described in the Section 6.3.1

- Box size: $L_x \times L_y = 2412 \times 1206\, c^2\, \omega_L^{-2}$
- Mesh size: $0.7 \times 0.7\, c^2\, \omega_L^{-2}$
- Timestep: $0.45\, \omega_L^{-1}$
- Cells are filled by 20 macro-ions of each species and 20 macro-electrons
- Boundary conditions: reflective for the plasma and absorbing for the fields for the wavelength shift case. x_{min} and x_{max} boundary conditions are reflective for the plasma and absorbing (Silver-Muller) for the fields, and y_{min} and y_{max} boundary conditions are periodic for both the plasma and the fields for the plasma flow case.
- No current filtering

Plasma parameters

- Homogeneous and non collisional plasma (+ one test simulation with a collisional plasma)
- Electron density: $0.04\, n_c$
- Ion species: Carbon (C) and plastic (CH) both fully ionized
- T_i: 1 keV
- T_e: 2 keV
- Plasma flow velocity at resonance (for the plasma flow case): $1.1176 \times 10^{-3} c$ for the Carbon (must be very precise because of the fine resonance peak) and $1.1113 \times 10^{-3} c$ for the CH.
- Application of 3 filters to smooth the current deposited by the macro-particles

Laser parameters

- Two RPP beams crossing each other
- Phase plate elements number: 6
- Crossing angle: $24°$ (beam 0 : $\theta_0 = 12°$, beam 1 : $_1 = -12°$)
- RPP field given as x_{min} boundary condition: $E_{tot} = E_0 + E_1$ where
  $E_{0,1} = \frac{E_l}{2}\sqrt{\frac{f}{f-x_{0,1}}}e^{\frac{iky_{0,1}^2}{2(f-x_{0,1})}}\sum_n e^{i\varphi_n}$
  $\times \left(\mathrm{erf}\left[e^{-\frac{i\pi}{4}}K(x_{0,1})\cdot(a_{n+1} - \frac{y_{0,1}f}{f-x_{0,1}})\right] - \mathrm{erf}\left[e^{-\frac{i\pi}{4}}K(x_{0,1})\cdot(a_n - \frac{y_{0,1}f}{f-x_{0,1}})\right]\right)$
  $x_{0,1}$ and $y_{0,1}$ being the coordinates of the beam shifted with an angle of $\theta_{0,1}$ in the simulation box referential. $a_n = nd$, d is the size of one phase plate element, $n \in [-N/2, N/2]$, $Nd = D$ is the size of the phase plate, $K(x)^2 = \frac{k}{2x} - \frac{k}{2f}$, f is the focal length.
- The laser pulses propagate from the left to the right
- Temporal evolution: ramp of $2000\,\omega_L^{-1}$ followed by a plateau until the end of the simulation
- Intensity: $I = 8.8 \times 10^{13}$ W cm^{-2} (a = 0.004) or $I = 2.2 \times 10^{13}$ W cm^{-2} (a = 0.002)
- The focal spots of the RPP beams are located in the middle of the simulation box
- f number: 8
- Beam waist: $w = 48\,\mu m$
- Frequency shift at resonance (for the wavelenght shift case): $\omega = kc_s = 4.535 \times 10^{-4}\,\omega_L$ the lower beam having the lowest frequency ($= 1 - 4.535 \times 10^{-4}$) for the CH and $\omega = kc_s = 4.79 \times 10^{-4}\,\omega_L$ for the C.

A.2.2 Results and figures plotting details

- Intensity map (Fig. 6.10): The output of the B_z field is made each 5000 timestep, and is averaged over a laser period (14 timesteps). The intensity map is the plot of the averaged field B_z^2.

- Exchanged power vs time (Fig. 6.9, 6.11, 6.12 and 6.14): $\Delta P/P_0$ is the power per unit length of the red-shifted beam minus the power of the blue-shifted beam, normalized to the initial power per unit length. The power of the red-shifted / blue shifted beam has been obtained by integrating the Poynting vector (*i.e.* B_z^2) at x_{max} over the upper ($y > 0$) / lower ($y < 0$) half of the simulation box. The values of each output are plot, that is to say each 5000 timesteps.

- Exchanged power vs deviation to resonance (Fig. 6.13): The value of $\Delta P/P_0$ is obtained as previously but only one point per species per value of deviation from the resonance is plotted, at asymptotic time ($t_{asymp} \simeq 2.3 \times 10^4$ for the CH and $t_{asymp} \simeq 1.3 \times 10^5$ for the Carbon.

Appendix B

Numerical heating

Simulation codes are built under a certain number of approximations affecting the accuracy of the phenomena numerically reproduced. In particular, our first simulations were affected by a strong numerical heating. As a matter of fact, most of PIC simulations are performed during a short physical time (ps) although the simulations here can last for hundreds of ps. Several strategies have been implemented in order to reduce the numerical heating. To make some tests with a small numerical cost, a first step was to compare the heating of the CBET simulation with the heating of a small window without laser. The black curves of fig. B.1 show that this reduced configuration reproduces well the numerical heating. All the following tests have been made in this reduced windows.Then, the size of the mesh has been reduced for all the simulations. According to fig. B.1, diminishing the size of the mesh strongly affects the numerical heating: the slope is divided by 2 for T_e and by 3 for T_i. Finally, successive filters have been applied to smooth the current deposited by the macro-particles [113]. N filters have been applied with N = 0, 1 or 3. The filter is binomial then compensatory with N the number of passes. Applying the N=3 current filter almost kills the heating. The configuration with the small meshes and N=3 have been used for all the CALDER simulations.

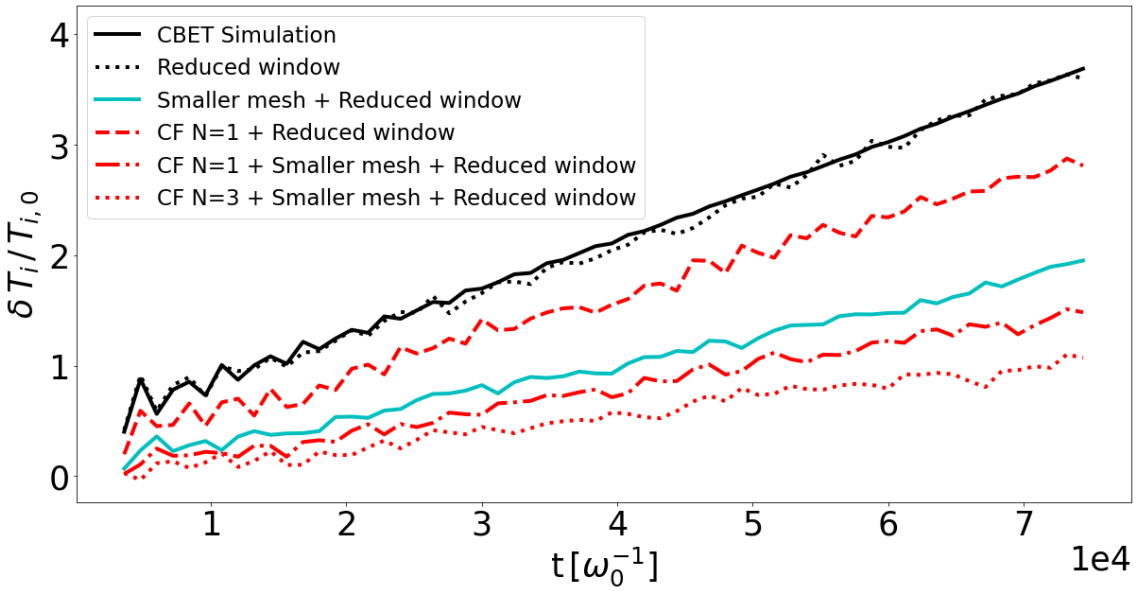

(a)

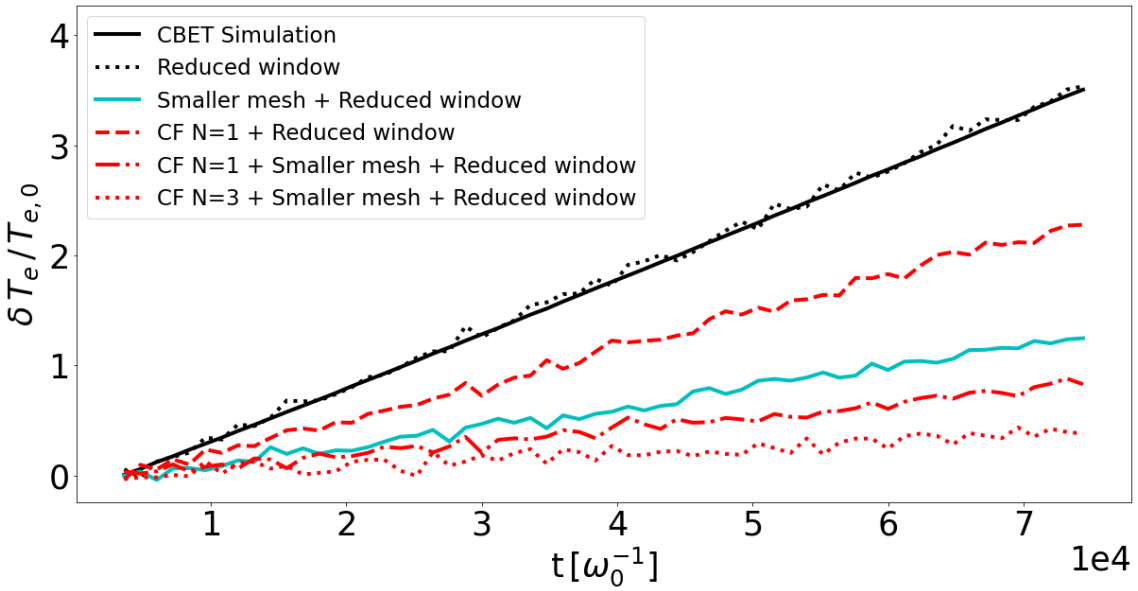

(b)

Figure B.1: Percentage of numerical heating as a function of time. (a) For the ions (b) For the electrons. The plain black lines are the first simulations of CBET without current filter, with the parameters of 5.2.1. The black dashed lines are simulations without laser, in a reduced window. All the other curves correspond to this reduced window. The cyan curve is with a smaller mesh without current filter. The dashed red curve is with a current filter without a smaller mesh. The dotted/dashed curve is with the smaller mesh and one current filters, the dotted curve with three current filter.

Appendix C

Résumé en français

Lors des expériences de fusion par confinement inertiel sur les grandes installations laser telles que le LMJ à Bordeaux ou le NIF aux États-Unis, les lasers sont amenés à se propager à travers des plasmas de grandes tailles (plusieurs millimètres). Un grand nombre d'instabilités dites de couplages d'ondes peuvent apparaître, et diffusent la lumière dans une direction différente de l'onde électromagnétique incidente. En particulier, les diffusions arrières Raman et Brillouin, ainsi que l'échange d'énergie entre faisceaux laser en résultent. Des techniques dites de lissage laser sont utilisées dans les grandes installations pour tenter de réduire ces phénomènes. Les faisceaux, une fois lissés, sont constitués de nombreux points chauds micrométriques nommés speckles. La Figure C.1 montre l'aspect d'un faisceau lissé.

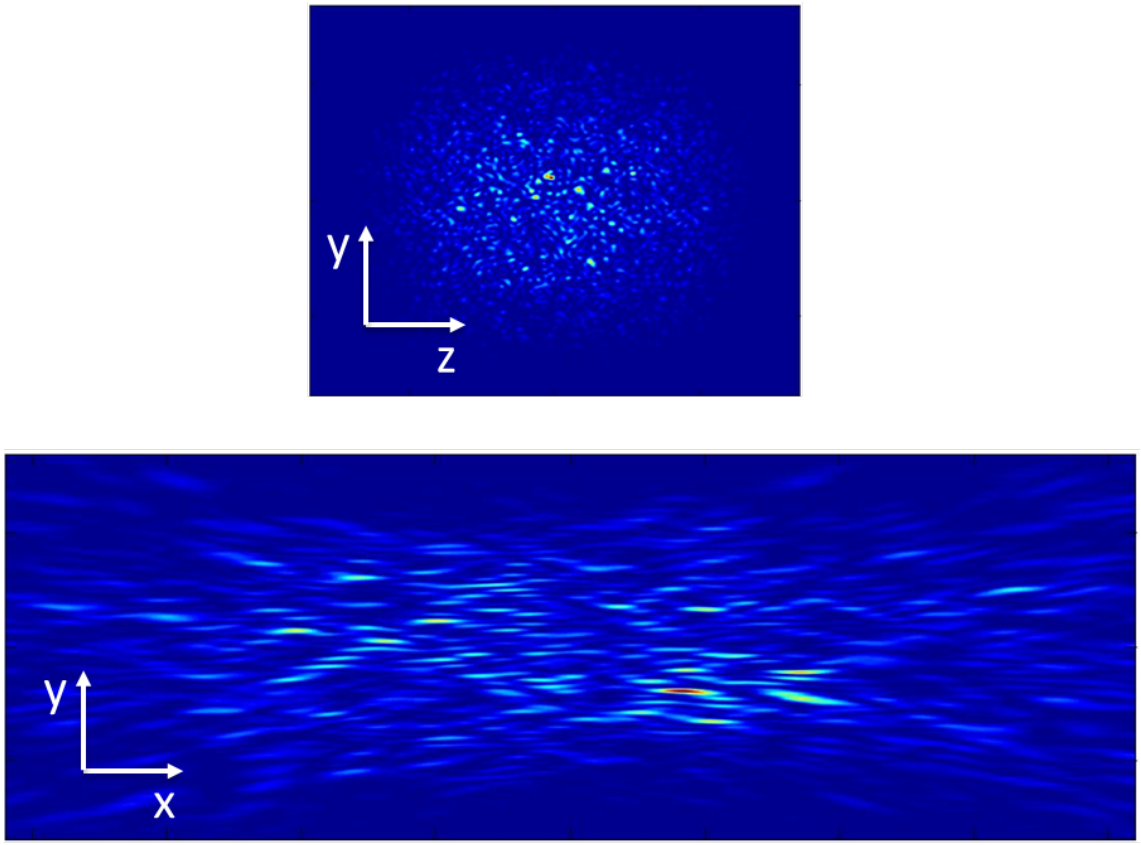

Figure C.1: Coupe transverse (haut) et longitudinale (bas) d'un faisceau laser lissé.

Lors de ces expériences, les faisceaux, focalisés autour d'une cible, vont être amenés à se croiser. La Figure C.2 montre deux exemples de zones où les lasers sont amenés à se croiser. En réalité, pour une expérience comprenant des centaines de faisceaux lasers, ces zones de croisement sont très nombreuses.

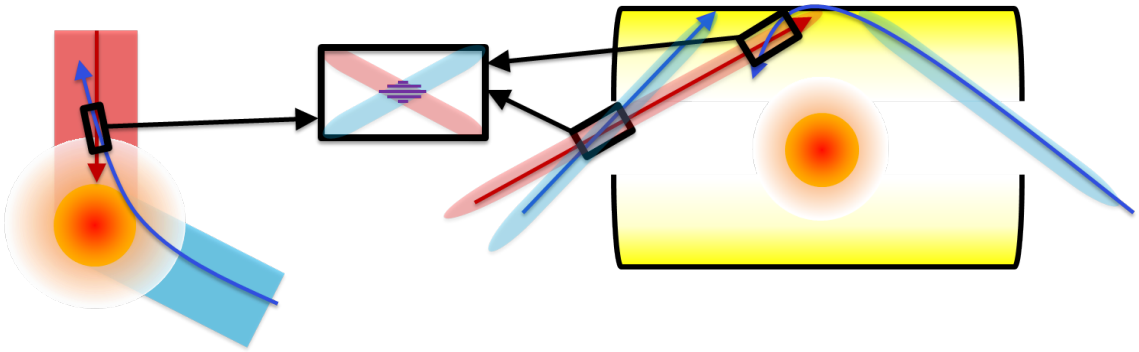

Figure C.2: Exemple de zone de croisement en configuration directe (gauche) et indirecte (droite)

Le couplage de deux ondes électromagnétiques cohérentes dans un milieu non-linéaire (le plasma), peut induire un échange d'énergie entre les faisceaux. Le croisement des lasers crée un réseau d'interférences (cf Fig. C.2), où la force pondéromotrice expulse les électrons. Les ions subissent la force de rappel électrostatique et suivent les éléctrons. Cela génère une modulation de densité, ou onde acoustique, qui diffracte les ondes électromagnétiques d'un faisceau vers l'autre, comme on peut le voir sur la Figure C.3.

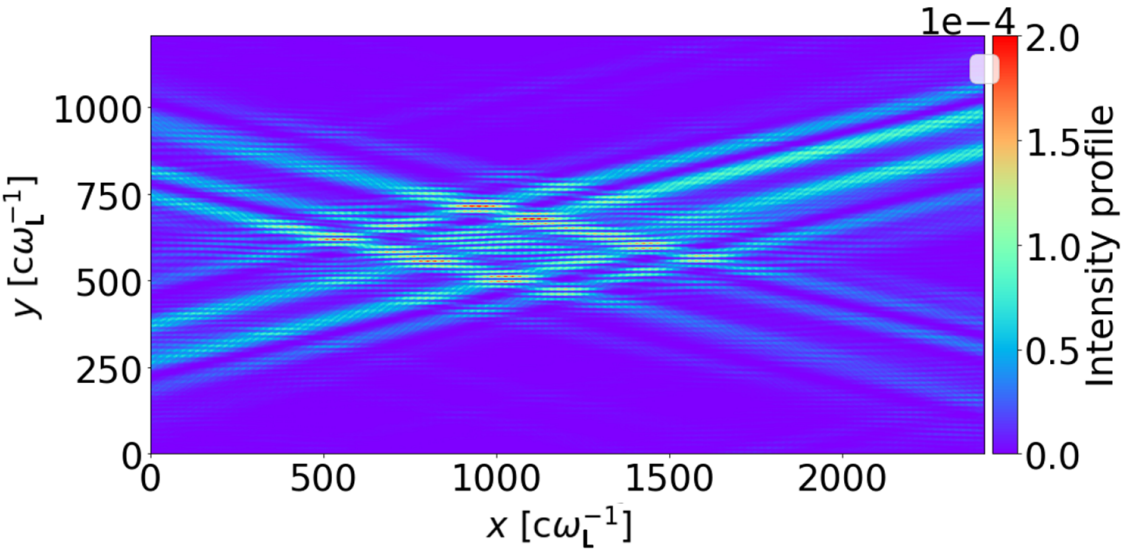

Figure C.3: Carte d'intensité de deux faisceaux laser lissés se croisant dans un plasma.

Cet échange, nommé Cross-beam Energy Transfer (CBET), a lieu si les lasers ont des fréquences différentes, ou si ces dernières sont égales mais que le plasma est en mouvement

dans la direction de l'onde acoustique. Nous avons montré que, bien que ces deux situations soient souvent considérées comme équivalentes dans les modèles hydrodynamiques, elles sont en réalité différentes. Ceci est dû au fait que l'échange est communément calculé en considérant les faisceaux laser comme des ondes planes, c'est-à-dire en négligeant le lissage laser.

Afin de démontrer cette non-équivalence, nous avons, dans un premier temps, étudié une situation académique, en considérant le croisement de deux faisceaux lasers constitués chacun de 4 speckles Gaussiens, comme nous pouvons le voir en Fig. C.4.

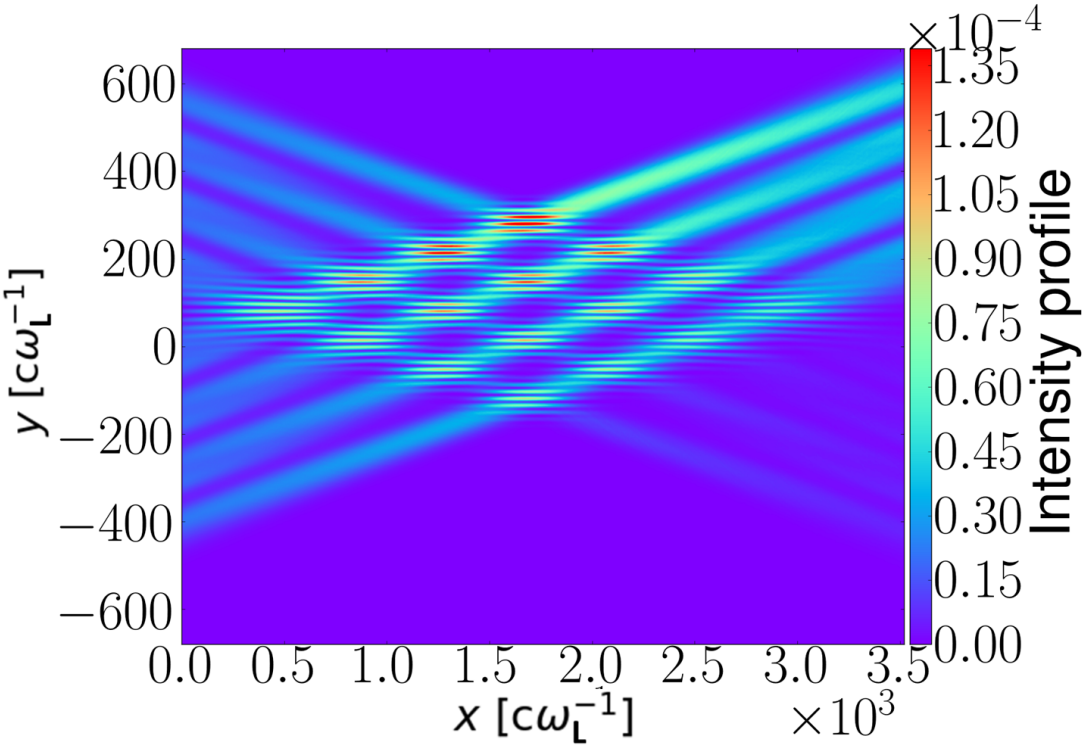

Figure C.4: Carte d'intensité de deux faisceaux laser constitués de quatre speckles Gaussiens se croisant dans un plasma.

Différentes simulations ont été effectuées grâce à un code cinétique "particle-in-cell", résolvant les équations de Vlasov et de Maxwell. Les simulations ont montré que lorsque l'échange d'énergie est induit par un plasma en mouvement, les modèles du type onde plane sont en mesure de prédire l'échange entre les faisceaux Gaussiens. Au contraire, lorsque l'échange est induit par des fréquences laser différentes, les modèles onde plane surestiment le transfert d'énergie. Ce modèle a également permit de distinguer deux configurations différentes pour le cas où les fréquences laser sont différentes. Dans le premier cas, les ondes acoustiques issues de différents

croisements de speckles sont en phase, et une interférence constructive résulte de leur interaction. Dans l'autre cas, les ondes sont déphasées résultant en une interférence destructive. Il a été montré que bien que l'échange soit plus important dans le cas en phase, l'échange demeure inférieur au cas flot de plasma. Le déphasage n'est donc pas la seule source de différence entre les deux situations. Ces résultats sont résumés en Fig. C.5. Ces résultats ont été obtenus en considérant un plasma faiblement amorti, où l'onde acoustique se propage et peut rencontrer plusieurs croisements de speckles avant d'être amortie.

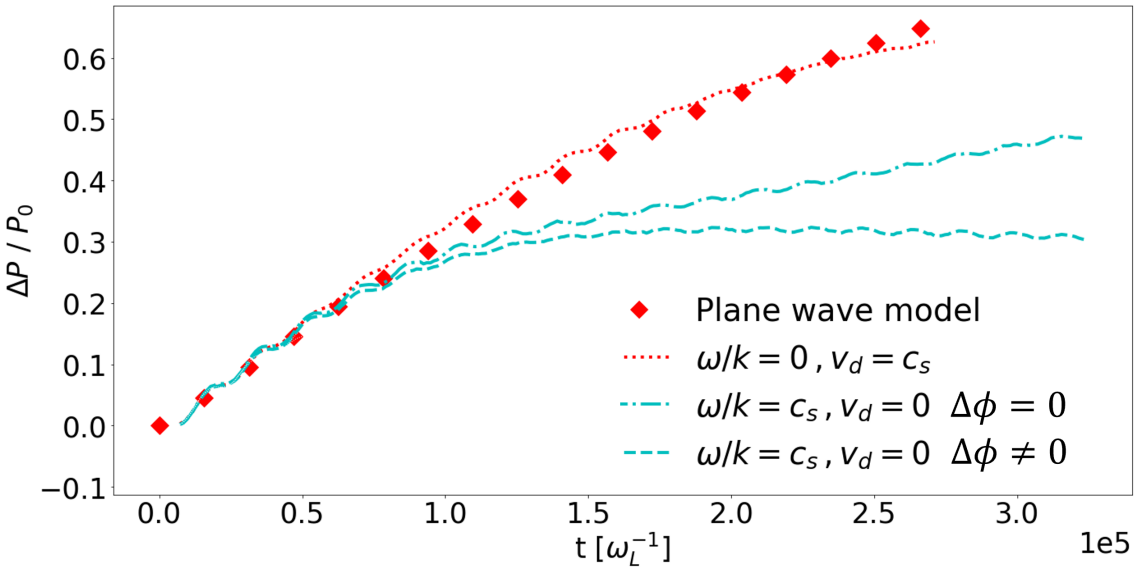

Figure C.5: Difference entre la puissance par unité de longueur d'un faisceau sortant par la moitié haute et de la moitié basse de la boite normalisé à la puissance initiale d'un faisceau, en fonction du temps.

Dans un second temps, une modélisation plus réaliste des faisceaux lissés à été adoptée. Pour cela, le champ d'un faisceau laser lissé à été calculé de façon exacte, permettant d'effectuer des simulations plus précises et de construire un modèle tenant compte de la structure réelle des speckles, telle qu'en Fig. C.3. Les résultats précédents ont été confirmés, même dans le cas d'un plasma fortement amorti. Nous avons également pu montrer que les conditions de résonance permettant au transfert d'énergie d'avoir lieu sont elles aussi affectées par le lissage laser. En particulier, la largeur de résonance du cas où les fréquences laser sont différentes est élargie par le lissage spatial, comme le montre la Figure C.6.

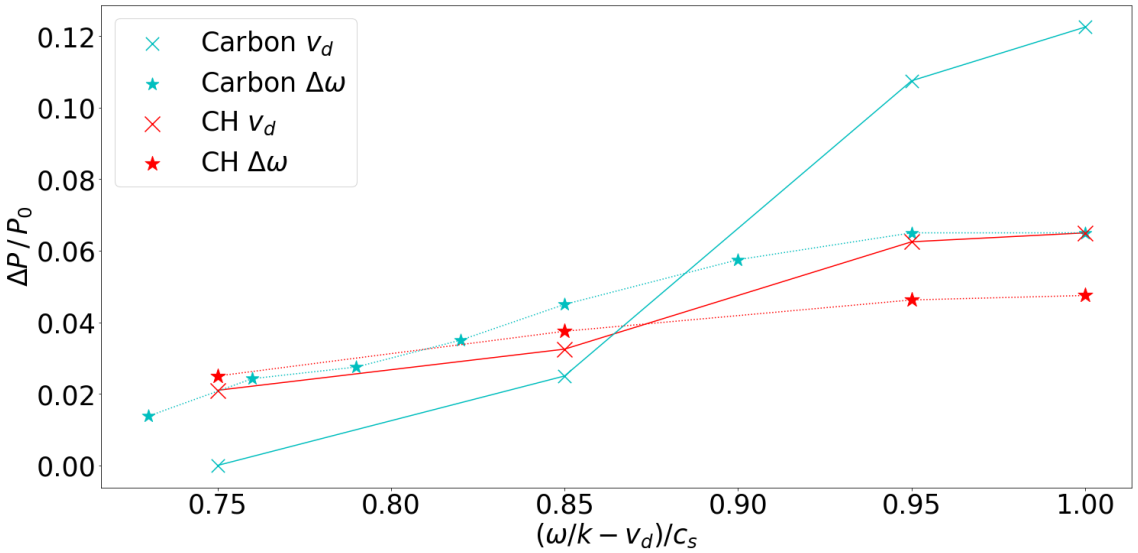

Figure C.6: Nuage de points représentant l'échange d'énergie entre deux faisceaux lissés en fonction de l'écart à la résonnance, pour un plasma de Carbone en cyan, de plastique (CH) en rouge, pour le cas avec un flot de plasma (croix reliées par un trait plein) et pour le cas avec décalage de fréquence (étoiles reliées par un trait pointillés).

References

[1] Milton Abramowitz, Irene A Stegun, and Robert H Romer. *Handbook of mathematical functions with formulas, graphs, and mathematical tables*. 1988.

[2] I M Begg and R A Cairns. "Enhanced reflection of laser light from an expanding plasma". In: *Journal of Physics D: Applied Physics* 9.16 (Nov. 1976), pp. 2341–2348. DOI: 10.1088/0022-3727/9/16/005. URL: https://doi.org/10.1088/0022-3727/9/16/005.

[3] V. I. Bespalov and V. I. Talanov. "Filamentary Structure of Light Beams in Nonlinear Liquids". In: *Soviet Journal of Experimental and Theoretical Physics Letters* 3 (June 1966), p. 307.

[4] Nicolas Bonod and Jérôme Neauport. "Diffraction gratings: from principles to applications in high-intensity lasers". In: *Adv. Opt. Photon.* 8.1 (Mar. 2016), pp. 156–199. DOI: 10.1364/AOP.8.000156. URL: http://opg.optica.org/aop/abstract.cfm?URI=aop-8-1-156.

[5] R.W. Boyd. *Nonlinear Optics*. Electronics & Electrical. Academic Press, 2003. ISBN: 9780121216825. URL: https://books.google.fr/books?id=30t9VmOmOGsC.

[6] A. Braun et al. “Self-channeling of high-peak-power femtosecond laser pulses in air”. In: *Opt. Lett.* 20.1 (Jan. 1995), pp. 73–75. DOI: 10.1364/OL.20.000073. URL: http://opg.optica.org/ol/abstract.cfm?URI=ol-20-1-73.

[7] C. B. Burckhardt. “Use of a Random Phase Mask for the Recording of Fourier Transform Holograms of Data Masks”. In: *Appl. Opt.* 9.3 (Mar. 1970), pp. 695–700. DOI: 10.1364/AO.9.000695. URL: http://opg.optica.org/ao/abstract.cfm?URI=ao-9-3-695.

[8] V. Yu. Bychenkov et al. “Kinetic theory of ion acoustic waves in a plasma with collisional electrons”. In: *Phys. Rev. E* 52.6 (Dec. 1995), pp. 6759–6776. DOI: 10.1103/PhysRevE.52.6759.

[9] V. Yu. Bychenkov et al. “Quasihydrodynamic description of ion acoustic waves in a collisional plasma”. In: *Physics of Plasmas* 1.8 (Aug. 1994), pp. 2419–2429. DOI: 10.1063/1.870570.

[10] A. Cain, G. Riazuelo, and J. Sajer. “Statistical spatial properties of speckle patterns generated by multiple laser beams”. In: *Phys. Plasmas* 18 (Aug. 2011), p. 082711. DOI: 10.1063/1.3626542.

[11] R. Y. Chiao, E. Garmire, and C. H. Townes. “Self-Trapping of Optical Beams”. In: *Phys. Rev. Lett.* 13 (15 Oct. 1964), pp. 479–482. DOI: 10.1103/PhysRevLett.13.479. URL: https://link.aps.org/doi/10.1103/PhysRevLett.13.479.

[12] C. E. Clayton et al. “Relativistic Plasma-Wave Excitation by Collinear Optical Mixing”. In: *Phys. Rev. Lett.* 54 (21 May 1985), pp. 2343–2346. DOI: 10.1103/PhysRevLett.54.2343. URL: https://link.aps.org/doi/10.1103/PhysRevLett.54.2343.

[13] B. I. Cohen et al. “Resonant stimulated Brillouin interaction of opposed laser beams in a drifting plasma”. In: *Physics of Plasmas* 5.9 (1998), pp. 3408–3415. DOI: 10.1063/1.873055. eprint: https://doi.org/10.1063/1.873055. URL: https://doi.org/10.1063/1.873055.

[14] Bruce I. Cohen, Allan N. Kaufman, and Kenneth M. Watson. “Beat Heating of a Plasma”. In: *Phys. Rev. Lett.* 29 (9 Aug. 1972), pp. 581–584. DOI: 10.1103/PhysRevLett.29.581. URL: https://link.aps.org/doi/10.1103/PhysRevLett.29.581.

[15] A. Colaïtis et al. “Modeling of the cross-beam energy transfer with realistic inertial-confinement-fusion beams in a large-scale hydrocode”. In: *Phys. Rev. E* 91.1, 013102 (Jan. 2015), p. 013102. DOI: 10.1103/PhysRevE.91.013102.

[16] A. Colaïtis et al. “Towards modeling of nonlinear laser-plasma interactions with hydrocodes: The thick-ray approach”. In: *Phys. Rev. E* 89.3, 033101 (Mar. 2014), p. 033101. DOI: 10.1103/PhysRevE.89.033101.

[17] A. Debayle et al. “A unified modeling of wave mixing processes with the ray tracing method”. In: *Physics of Plasmas* 26.9 (2019), p. 092705. DOI: 10.1063/1.5110247.

[18] A. Debayle et al. “Cross-beam energy transfer: On the accuracy of linear stationary models in the linear kinetic regime”. In: *Physics of Plasmas* 25.5 (May 2018), p. 052702. DOI: 10.1063/1.5026187.

[19] J. Derouillat et al. “Smilei : A collaborative, open-source, multi-purpose particle-in-cell code for plasma simulation”. In: *Computer Physics Communications* 222 (2018), pp. 351–373. ISSN: 0010-4655. DOI: https://doi.org/10.1016/j.cpc.2017.09.024. URL: https://www.sciencedirect.com/science/article/pii/S0010465517303314.

[20] Thierry Dewandre, James R. Albritton, and E. A. Williams. "Doppler shift of laser light reflected from expanding plasmas". In: *The Physics of Fluids* 24.3 (1981), pp. 528–536. DOI: 10.1063/1.863401.

[21] S. N. Dixit et al. "Kinoform phase plates for focal plane irradiance profile control". In: *Opt. Lett.* 19.6 (Mar. 1994), pp. 417–419. DOI: 10.1364/OL.19.000417. URL: https://opg.optica.org/ol/abstract.cfm?URI=ol-19-6-417.

[22] M. R. Edwards and Pierre Michel. "Plasma Transmission Gratings for Compression of High-Intensity Laser Pulses". In: *Phys. Rev. Applied* 18 (2 Aug. 2022), p. 024026. DOI: 10.1103/PhysRevApplied.18.024026.

[23] E. M. Epperlein. "Effect of electron collisions on ion-acoustic waves and heat flow". In: *Physics of Plasmas* 1.1 (Jan. 1994), pp. 109–115. DOI: 10.1063/1.870563.

[24] Kent Estabrook et al. "Estimates of Intensity, Wavelength, and Bandwidth Scaling of Brillouin Backscatter". In: *Phys. Rev. Lett.* 46 (11 Mar. 1981), pp. 724–727. DOI: 10.1103/PhysRevLett.46.724. URL: https://link.aps.org/doi/10.1103/PhysRevLett.46.724.

[25] R. Fazeli. "Efficient X-ray emission from laser-irradiated low-density lead target: a substitute for gold in hohlraum design". In: *Applied Physics B* 121.1 (Aug. 2015), pp. 95–105. DOI: 10.1103/PhysRevE.91.013102.

[26] R. K Follett et al. "Two-Plasmon Decay Mitigation in Direct-Drive Inertial-Confinement-Fusion Experiments Using Multilayer Targets". In: *Physical Review Letters* 116 (Apr. 2016), p. 155002. DOI: 10.1103/PhysRevLett.116.155002.

[27] R. K. Follett et al. “Ray-based modeling of cross-beam energy transfer at caustics”. In: *Phys. Rev. E* 98.4, 043202 (Oct. 2018), p. 043202. DOI: 10.1103/PhysRevE.98.043202.

[28] Burton D Fried and Samuel D Conte. *The plasma dispersion function: the Hilbert transform of the Gaussian*. Academic Press, 2015.

[29] Burton D. Fried, Roscoe B. White, and Thomas K. Samec. “Ion Acoustic Waves in a Multi-Ion Plasma”. In: *The Physics of Fluids* 14.11 (1971), pp. 2388–2392. DOI: 10.1063/1.1693346. eprint: https://aip.scitation.org/doi/pdf/10.1063/1.1693346. URL: https://aip.scitation.org/doi/abs/10.1063/1.1693346.

[30] D. H. Froula et al. “Increasing Hydrodynamic Efficiency by Reducing Cross-Beam Energy Transfer in Direct-Drive-Implosion Experiments”. In: *Phys. Rev. Lett.* 108 (12 Mar. 2012), p. 125003. DOI: 10.1103/PhysRevLett.108.125003. URL: https://link.aps.org/doi/10.1103/PhysRevLett.108.125003.

[31] C. Garban-Labaune et al. “Effect of Laser Wavelength and Pulse Duration on Laser-Light Absorption and Back Reflection”. In: *Phys. Rev. Lett.* 48 (15 Apr. 1982), pp. 1018–1021. DOI: 10.1103/PhysRevLett.48.1018. URL: https://link.aps.org/doi/10.1103/PhysRevLett.48.1018.

[32] J. Garnier. “Statistics of the hot spots of smoothed beams produced by random phase plates revisited”. In: *Physics of Plasmas* 6.5 (1999), pp. 1601–1610. DOI: 10.1063/1.873413.

[33] Siegfried H. Glenzer et al. “Symmetric Inertial Confinement Fusion Implosions at Ultra-High Laser Energies”. In: *Science* 327 (2010), pp. 1228–1231.

[34] V. N. Goncharov et al. “Improving the hot-spot pressure and demonstrating ignition hydrodynamic equivalence in cryogenic deuterium–tritium implosions on OMEGA”. In: *Physics of Plasmas* 21.5 (2014), p. 056315. DOI: 10.1063/1.4876618.

[35] A. M. Hansen et al. “Cross-Beam Energy Transfer Saturation by Ion Heating”. In: *Phys. Rev. Lett.* 126 (7 Feb. 2021), p. 075002. DOI: 10.1103/PhysRevLett.126.075002.

[36] TP Hughes. “A new method for the determination of plasma electron temperature and density from Thomson scattering of an optical maser beam”. In: *Nature* 194.4825 (1962), pp. 268–269.

[37] S. Huller et al. “Crossed beam energy transfer in the presence of laser speckle ponderomotive self-focusing and nonlinear sound waves”. In: *Physics Of Plasmas* 27.2 (Feb. 2020). DOI: 10.1063/1.5125759.

[38] A. Javan, W. R. Bennett, and D. R. Herriott. “Population Inversion and Continuous Optical Maser Oscillation in a Gas Discharge Containing a He-Ne Mixture”. In: *Phys. Rev. Lett.* 6 (3 Feb. 1961), pp. 106–110. DOI: 10.1103/PhysRevLett.6.106. URL: https://link.aps.org/doi/10.1103/PhysRevLett.6.106.

[39] O. S. Jones et al. “A high-resolution integrated model of the National Ignition Campaign cryogenic layered experiments”. In: *Physics of Plasmas* 19.5 (2012), p. 056315. DOI: 10.1063/1.4718595. eprint: https://doi.org/10.1063/1.4718595. URL: https://doi.org/10.1063/1.4718595.

[40] Y Kato and K Mima. “Random phase-shifting of laser-beam for absorption profile smoothing and instability suppression in laser-produced plasmas”. In: *APPLIED PHYSICS B-PHOTOPHYSICS AND LASER CHEMISTRY*.

Vol. 29. 3. SPRINGER VERLAG 175 FIFTH AVE, NEW YORK, NY 10010. 1982, pp. 186–187.

[41] Y. Kato et al. "Random Phasing of High-Power Lasers for Uniform Target Acceleration and Plasma-Instability Suppression". In: *Phys. Rev. Lett.* 53 (11 Sept. 1984), pp. 1057–1060. DOI: 10.1103/PhysRevLett.53.1057. URL: https://link.aps.org/doi/10.1103/PhysRevLett.53.1057.

[42] J. Katz et al. "A transmitted-beam diagnostic for the wavelength-tunable UV drive beam on OMEGA". In: *Review of Scientific Instruments* 92.3 (2021), p. 033526. DOI: 10.1063/5.0042877. eprint: https://doi.org/10.1063/5.0042877. URL: https://doi.org/10.1063/5.0042877.

[43] C J Keane. "National Ignition Facility User Guide". In: (Sept. 2014). DOI: 10.2172/1170357. URL: https://www.osti.gov/biblio/1170357.

[44] R. K. Kirkwood et al. "Observation of Energy Transfer between Frequency-Mismatched Laser Beams in a Large-Scale Plasma". In: *Phys. Rev. Lett.* 76 (12 Mar. 1996), pp. 2065–2068. DOI: 10.1103/PhysRevLett.76.2065.

[45] R. K. Kirkwood et al. "Observation of Saturation of Energy Transfer between Copropagating Beams in a Flowing Plasma". In: *Phys. Rev. Lett.* 89 (21 Nov. 2002), p. 215003. DOI: 10.1103/PhysRevLett.89.215003. URL: https://link.aps.org/doi/10.1103/PhysRevLett.89.215003.

[46] Nicholas A Krall and Alvin W Trivelpiece. "Principles of plasma physics". In: *American Journal of Physics* 41.12 (1973), pp. 1380–1381.

[47] A. L. Kritcher et al. "Energy transfer between lasers in low-gas-fill-density hohlraums". In: *Phys. Rev. E* 98 (5 Nov. 2018), p. 053206. DOI: 10.1103/PhysRevE.98.053206.

[48] Andrea Kritcher et al. “Design of inertial fusion implosions reaching the burning plasma regime”. In: *Nature Physics* 18 (Mar. 2022). DOI: 10.1038/s41567-021-01485-9.

[49] Norman M. Kroll, Amiram Ron, and Norman Rostoker. “Optical Mixing as a Plasma Density Probe”. In: *Phys. Rev. Lett.* 13 (3 July 1964), pp. 83–86. DOI: 10.1103/PhysRevLett.13.83. URL: https://link.aps.org/doi/10.1103/PhysRevLett.13.83.

[50] W.L. Kruer, K.G. Estabook, and K.H. Sinz. “Instability-generated laser reflection in plasmas”. In: *Nuclear Fusion* 13.6 (Dec. 1973), pp. 952–955. DOI: 10.1088/0029-5515/13/6/024. URL: https://doi.org/10.1088/0029-5515/13/6/024.

[51] William L. Kruer et al. “Energy transfer between crossing laser beams”. In: *Physics of Plasmas* 3.1 (1996), pp. 382–385. DOI: 10.1063/1.871863.

[52] Willis E. Lamb. “Theory of an Optical Maser”. In: *Phys. Rev.* 134 (6A June 1964), A1429–A1450. DOI: 10.1103/PhysRev.134.A1429. URL: https://link.aps.org/doi/10.1103/PhysRev.134.A1429.

[53] L. Lancia et al. “Experimental Evidence of Short Light Pulse Amplification Using Strong-Coupling Stimulated Brillouin Scattering in the Pump Depletion Regime”. In: *Phys. Rev. Lett.* 104 (2 Jan. 2010), p. 025001. DOI: 10.1103/PhysRevLett.104.025001. URL: https://link.aps.org/doi/10.1103/PhysRevLett.104.025001.

[54] Irving Langmuir. “Oscillations in ionized gases”. In: *Proceedings of the National Academy of Sciences* 14.8 (1928), pp. 627–637.

[55] Bernard Lapeyre, Étienne Pardoux, and Rémi Sentis. “Méthodes de Monte-Carlo pour les équations de transport et de diffusion”. In: (1998).

[56] E Lefebvre et al. “Electron and photon production from relativistic laser–plasma interactions”. In: *Nuclear Fusion* 43 (July 2003). DOI: 10.1088/0029-5515/43/7/317.

[57] G. Lehmann and K. H. Spatschek. “Nonlinear Brillouin amplification of finite-duration seeds in the strong coupling regime”. In: *Physics of Plasmas* 20.7 (2013), p. 073112. DOI: 10.1063/1.4816030. eprint: https://doi.org/10.1063/1.4816030. URL: https://doi.org/10.1063/1.4816030.

[58] R.H. Lehmberg. “Numerical study of phase conjugation in stimulated backscatter with pump depletion”. In: *Optics Communications* 43.5 (1982), pp. 369–374. ISSN: 0030-4018. DOI: https://doi.org/10.1016/0030-4018(82)90231-0. URL: https://www.sciencedirect.com/science/article/pii/0030401882902310.

[59] J. D. Lindl et al. “The physics basis for ignition using indirect-drive targets on the National Ignition Facility”. In: *Physics of Plasmas* 11 (Feb. 2004), pp. 339–491. DOI: 10.1063/1.1578638.

[60] Thorsten Loewenhoff. “Combined steady state and high cycle transient heat load simulation with the electron beam facility JUDITH 2”. PhD thesis. July 2012.

[61] D. J. Y. Marion et al. “Modeling crossed-beam energy transfer for inertial confinement fusion”. In: *Physics of Plasmas* 23.5 (May 2016), p. 052705. DOI: 10.1063/1.4948489.

[62] J A Marozas et al. “Continuous distributed phase-plate advances for high-energy laser systems”. In: *Journal of Physics: Conference Series* 717.1 (May 2016), p. 012107. DOI: 10.1088/1742-6596/717/1/012107. URL: https://dx.doi.org/10.1088/1742-6596/717/1/012107.

[63] C. E. Max, W. C. Mead, and J. J. Thomson. "Mechanisms of the plasma spatial filter for high-power lasers". In: *Applied Physics Letters* 29.12 (1976), pp. 783–785. DOI: 10.1063/1.88947. eprint: https://doi.org/10.1063/1.88947. URL: https://doi.org/10.1063/1.88947.

[64] A. V. Maximov et al. "Effects of plasma long-wavelength hydrodynamical fluctuations on stimulated Brillouin scattering". In: *Physics of Plasmas* 3.5 (1996), pp. 1689–1699. DOI: 10.1063/1.871679.

[65] C. J. McKinstrie et al. "Power exchange between crossed laser beams and the associated frequency cascade". In: *Phys. Rev. E* 55 (2 Feb. 1997), pp. 2044–2047. DOI: 10.1103/PhysRevE.55.2044. URL: https://link.aps.org/doi/10.1103/PhysRevE.55.2044.

[66] C. J. McKinstrie et al. "Two-dimensional analysis of the power transfer between crossed laser beams". In: *Physics of Plasmas* 3 (July 1996), pp. 2686–2692. DOI: 10.1063/1.871721.

[67] P Michel et al. "Tuning the Implosion Symmetry of ICF Targets via Controlled Crossed-Beam Energy Transfer". In: *Physical review letters* 102 (Feb. 2009), p. 025004. DOI: 10.1103/PhysRevLett.102.025004.

[68] P. Michel et al. "Dynamic Control of the Polarization of Intense Laser Beams via Optical Wave Mixing in Plasmas". In: *Phys. Rev. Lett.* 113.20 (Nov. 2014). ISSN: 0031-9007. DOI: 10.1103/PhysRevLett.113.205001.

[69] P. Michel et al. "Stochastic Ion Heating from Many Overlapping Laser Beams in Fusion Plasmas". In: *Phys. Rev. Lett.* 109 (19 Nov. 2012), p. 195004. DOI: 10.1103/PhysRevLett.109.195004.

[70] P. Michel et al. "Studies of the laser filament instability in a semicollisional plasma". In: *Physics of Plasmas* 10 (Sept. 2003), pp. 3545–3553. DOI: 10.1063/1.1598204.

[71] P. Michel et al. "Symmetry tuning via controlled crossed-beam energy transfer on the National Ignition Facility". In: *Physics of Plasmas* 17.5 (2010), p. 056305. DOI: 10.1063/1.3325733.

[72] Gaurav Mishra and Karabi Ghosh. "Investigation of various methods for wall loss reduction in Inertial Confinement Fusion hohlraums". In: *High Energy Density Physics* 33 (2019), p. 100714. ISSN: 1574-1818. DOI: 10.1016/j.hedp.2019.100714.

[73] Carlos Montes. "Reflection limitation by driven stimulated Brillouin rescattering and finite-bandwidth spectral interaction". In: *Phys. Rev. A* 31 (4 Apr. 1985), pp. 2366–2374. DOI: 10.1103/PhysRevA.31.2366. URL: https://link.aps.org/doi/10.1103/PhysRevA.31.2366.

[74] David Montgomery. "On the resonant excitation of plasma oscillations with laser beams". In: *Physica* 31.5 (1965), pp. 693–702. ISSN: 0031-8914. DOI: https://doi.org/10.1016/0031-8914(65)90007-8. URL: https://www.sciencedirect.com/science/article/pii/0031891465900078.

[75] Jérôme Néauport et al. "Design and optical characterization of a large continuous phase plate for Laser Integration Line and laser Megajoule facilities". In: *Appl. Opt.* 42.13 (May 2003), pp. 2377–2382. DOI: 10.1364/AO.42.002377. URL: https://opg.optica.org/ao/abstract.cfm?URI=ao-42-13-2377.

[76] C Neuville et al. "Inhibition of crossed-beam energy transfer induced by expansion-velocity fluctuations". In: *Plasma Physics and Controlled Fusion* 60.4 (Feb. 2018), p. 044006. DOI: 10.1088/1361-6587/aaab23.

[77] C. Neuville et al. “Spatial and Transient Effects during the Amplification of a Picosecond Pulse Beam by a Nanosecond Pump”. In: *Phys. Rev. Lett* 117.14, 145001 (Sept. 2016), p. 145001. DOI: 10.1103/PhysRevLett.117.145001.

[78] D.R. Nicholson. *Introduction to Plasma Theory*. Wiley, 1983. ISBN: 9780471090458. URL: https://books.google.fr/books?id=fyRRAAAAMAAJ.

[79] H. Nishimura et al. “Study of indirectly driven implosion by x-ray spectroscopic measurements”. In: *Physics of Plasmas* 2.6 (1995), pp. 2063–2074. DOI: 10.1063/1.871293.

[80] J. Nuckolls et al. “Laser Compression of Matter to Super-High Densities: Thermonuclear (CTR) Applications”. In: *Nature* 239 (Sept. 1972), pp. 139–142. DOI: 10.1038/239139a0.

[81] Thomas O’Neil. “Collisionless Damping of Nonlinear Plasma Oscillations”. In: *The Physics of Fluids* 8.12 (1965), pp. 2255–2262. DOI: 10.1063/1.1761193. eprint: https://aip.scitation.org/doi/pdf/10.1063/1.1761193. URL: https://aip.scitation.org/doi/abs/10.1063/1.1761193.

[82] John A. Oertel et al. “Gated x-ray detector for the National Ignition Facility”. In: *Review of Scientific Instruments* 77.10 (2006), 10E308. DOI: 10.1063/1.2227439. eprint: https://doi.org/10.1063/1.2227439. URL: https://doi.org/10.1063/1.2227439.

[83] T. J. Orzechowski et al. “The Rosseland Mean Opacity of a Mixture of Gold and Gadolinium at High Temperatures”. In: *Phys. Rev. Lett.* 77 (17 Oct. 1996), pp. 3545–3548. DOI: 10.1103/PhysRevLett.77.3545.

[84] A. Oudin et al. “Cross-beam energy transfer between spatially smoothed laser beams”. In: *Physics of Plasmas* 29.11 (2022), p. 112112. DOI: 10.1063/5.

0109511. eprint: https://doi.org/10.1063/5.0109511. URL: https://doi.org/10.1063/5.0109511.

[85] A. Oudin et al. "Reduction of Cross-Beam Energy Transfer by a Speckle Pattern". In: *Phys. Rev. Lett.* 127 (26 Dec. 2021), p. 265001. DOI: 10.1103/PhysRevLett.127.265001. URL: https://link.aps.org/doi/10.1103/PhysRevLett.127.265001.

[86] C. J. Pawley, H. E. Huey, and N. C. Luhmann. "Observation of the Growth and Saturation of Ion Waves Generated by Optical Mixing". In: *Phys. Rev. Lett.* 49 (12 Sept. 1982), pp. 877–880. DOI: 10.1103/PhysRevLett.49.877. URL: https://link.aps.org/doi/10.1103/PhysRevLett.49.877.

[87] NF Pilipetskii and AR Rustamov. "Observation of self-focusing of light in liquids". In: *JETP LETTERS-USSR* 2.2 (1965), pp. 55–+.

[88] P. M. Platzman, S. J. Buchsbaum, and N. Tzoar. "Light-Off-Light Scattering in a Plasma". In: *Phys. Rev. Lett.* 12 (21 May 1964), pp. 573–575. DOI: 10.1103/PhysRevLett.12.573. URL: https://link.aps.org/doi/10.1103/PhysRevLett.12.573.

[89] G. Raj and S. Hüller. "Impact of Laser Beam Speckle Structure on Crossed Beam Energy Transfer via Beam Deflections and Ponderomotive Self-Focusing". In: *Phys. Rev Lett.* 118.5, 055002 (Feb. 2017), p. 055002. DOI: 10.1103/PhysRevLett.118.055002.

[90] C. J. Randall, James R. Albritton, and J. J. Thomson. "Theory and simulation of stimulated Brillouin scatter excited by nonabsorbed light in laser fusion systems". In: *The Physics of Fluids* 24.8 (1981), pp. 1474–1484. DOI: 10.1063/1.863551. eprint: https://aip.scitation.org/doi/pdf/10.

1063/1.863551. URL: https://aip.scitation.org/doi/abs/10.1063/1.86355.

[91] CJ Randall. "Effect of ion collisionality on ion-acoustic waves". In: *The Physics of Fluids* 25.12 (1982), pp. 2231–2233.

[92] C. Riconda et al. "Spectral characteristics of ultra-short laser pulses in plasma amplifiers". In: *Physics of Plasmas* 20.8 (2013), p. 083115. DOI: 10.1063/1.4818893. eprint: https://doi.org/10.1063/1.4818893. URL: https://doi.org/10.1063/1.4818893.

[93] Harvey Rose and Sandip Ghosal. "Nonlinear theory of power transfer between multiple crossed laser beams in a flowing plasma". In: *Physics of Plasmas* 5 (May 1998), pp. 1461–1466. DOI: 10.1063/1.872804.

[94] Harvey A. Rose and D. F. DuBois. "Statistical properties of laser hot spots produced by a random phase plate". In: *Physics of Fluids B: Plasma Physics* 5.2 (1993), pp. 590–596. DOI: 10.1063/1.860545. eprint: https://doi.org/10.1063/1.860545. URL: https://doi.org/10.1063/1.860545.

[95] M. N. Rosenbluth and C. S. Liu. "Excitation of Plasma Waves by Two Laser Beams". In: *Phys. Rev. Lett.* 29 (11 Sept. 1972), pp. 701–705. DOI: 10.1103/PhysRevLett.29.701. URL: https://link.aps.org/doi/10.1103/PhysRevLett.29.701.

[96] A. L. Schawlow and C. H. Townes. "Infrared and Optical Masers". In: *Phys. Rev.* 112 (6 Dec. 1958), pp. 1940–1949. DOI: 10.1103/PhysRev.112.1940. URL: https://link.aps.org/doi/10.1103/PhysRev.112.1940.

[97] G SCHMIDT. "RESONANT EXCITATION OF ELECTROSTATIC MODES WITH ELECTROMAGNETIC WAVES". In: *PHYSICS OF FLUIDS* 16.10 (1973), pp. 1676–1679. ISSN: 1070-6631. DOI: 10.1063/1.1694195.

[98] A. G. Seaton et al. “Cross-beam energy transfer in direct-drive ICF. I. Nonlinear and kinetic effects”. In: *Physics of Plasmas* 29.4 (2022), p. 042706. DOI: 10.1063/5.0078800. eprint: https://doi.org/10.1063/5.0078800. URL: https://doi.org/10.1063/5.0078800.

[99] A. G. Seaton et al. “Cross-beam energy transfer in direct-drive ICF. I. Nonlinear and kinetic effects”. In: *Physics of Plasmas* 29.4 (2022), p. 042706. DOI: 10.1063/5.0078800. eprint: https://doi.org/10.1063/5.0078800. URL: https://doi.org/10.1063/5.0078800.

[100] W. Simmons et al. “A high energy spatial filter for removal of small scale beam instabilities in high power solid state lasers”. In: *IEEE Journal of Quantum Electronics* 11.9 (1975), pp. 852–852. DOI: 10.1109/JQE.1975.1068918.

[101] A. Sjölund and L. Stenflo. “PARAMETRIC COUPLING BETWEEN ION WAVES AND ELECTROMAGNETIC WAVES”. In: *Applied Physics Letters* 10.7 (1967), pp. 201–202. DOI: 10.1063/1.1754910. eprint: https://doi.org/10.1063/1.1754910. URL: https://doi.org/10.1063/1.1754910.

[102] S. Skupsky et al. “Improved laser-beam uniformity using the angular dispersion of frequency-modulated light”. In: *Journal of Applied Physics* 66.8 (1989), pp. 3456–3462. DOI: 10.1063/1.344101. eprint: https://doi.org/10.1063/1.344101. URL: https://doi.org/10.1063/1.344101.

[103] Igor V. Sokolov. “Alternating-order interpolation in a charge-conserving scheme for particle-in-cell simulations”. In: *Computer Physics Communications* 184.2 (2013), pp. 320–328. ISSN: 0010-4655. DOI: 10.1016/j.cpc.2012.09.0155.

[104] B. L. Stansfield, R. Nodwell, and J. Meyer. “Enhanced Scattering of Laser Light by Optical Mixing in a Plasma”. In: *Phys. Rev. Lett.* 26 (20 May 1971), pp. 1219–1221. DOI: 10.1103/PhysRevLett.26.1219.

[105] R. A. Stern and N. Tzoar. "Parametric Coupling Between Electron-Plasma and Ion-Acoustic Oscillations". In: *Physical Review Letters* 17.17 (Oct. 1966), pp. 903–905. DOI: 10.1103/PhysRevLett.17.903.

[106] D. J. Strozzi et al. "Interplay of Laser-Plasma Interactions and Inertial Fusion Hydrodynamics". In: *Phys. Rev. Lett* 118.2, 025002 (Jan. 2017), p. 025002. DOI: 10.1103/PhysRevLett.118.025002.

[107] D. J. Strozzi et al. "Ray-based calculations of backscatter in laser fusion targets". In: *Physics of Plasmas* 15.10, 102703 (Oct. 2008), p. 102703. DOI: 10.1063/1.2992522.

[108] Toshiki Tajima and John M Dawson. "Laser electron accelerator". In: *Physical Review Letters* 43.4 (1979), p. 267.

[109] Tomas Tolenis et al. "Next generation highly resistant mirrors featuring all-silica layers". In: *Scientific Reports* 7 (Sept. 2017). DOI: 10.1038/s41598-017-11275-0.

[110] Elen Tolstik. "Light Self-Trapping in Polymeric Media based on Polymethylmethacrylate with Distributed Phenanthrenequinone Molecules". In: (Aug. 2022).

[111] MD Tracy et al. "Eigenvalue solution for the ion-collisional effects on ion-acoustic and entropy waves". In: *Physics of Fluids B: Plasma Physics* 5.5 (1993), pp. 1430–1439.

[112] D. Turnbull et al. "High Power Dynamic Polarization Control Using Plasma Photonics". In: *Phys. Rev. Lett.* 116 (20 May 2016), p. 205001. DOI: 10.1103/PhysRevLett.116.205001.

[113] J. -L. Vay et al. “Numerical methods for instability mitigation in the modeling of laser wakefield accelerators in a Lorentz-boosted frame”. In: *Journal of Computational Physics* 230.15 (July 2011), pp. 5908–5929. DOI: 10.1016/j.jcp.2011.04.003.

[114] H. X. Vu, D. F. DuBois, and B. Bezzerides. “Kinetic inflation of stimulated Raman backscatter in regimes of high linear Landau damping”. In: *Physics of Plasmas* 9.5 (2002), pp. 1745–1763. DOI: 10.1063/1.1471235.

[115] K. B. Wharton et al. “Observation of Energy Transfer between Identical-Frequency Laser Beams in a Flowing Plasma”. In: *Phys. Rev. Lett.* 81 (11 Sept. 1998), pp. 2248–2251. DOI: 10.1103/PhysRevLett.81.2248.

[116] E. A. Williams et al. “Effects of ion trapping on crossed-laser-beam stimulated Brillouin scattering”. In: *Physics of Plasmas* 11.1 (2004), pp. 231–244. DOI: 10.1063/1.1630573. eprint: https://doi.org/10.1063/1.1630573. URL: https://doi.org/10.1063/1.1630573.

[117] E. A. Williams et al. “The frequency and damping of ion acoustic waves in hydrocarbon (CH) and two-ion-species plasmas”. In: *Physics of Plasmas* 2.1 (1995), pp. 129–138. DOI: 10.1063/1.871101. eprint: https://doi.org/10.1063/1.871101.

[118] L. Yin et al. “Saturation of cross-beam energy transfer for multispeckled laser beams involving both ion and electron dynamics”. In: *Physics of Plasmas* 26.8 (2019), p. 082708. DOI: 10.1063/1.5111334.

[119] Hang Zhao et al. “Progress in optical Thomson scattering diagnostics for ICF gas-filled hohlraums”. In: *Matter and Radiation at Extremes* 4.5 (2019), p. 055201. DOI: 10.1063/1.5090971.

[120] A. Zylstra et al. “Burning plasma achieved in inertial fusion”. In: *Nature* 601 (Jan. 2022), pp. 542–548. DOI: 10.1038/s41586-021-04281-w.

[121] A. B. Zylstra et al. “Record Energetics for an Inertial Fusion Implosion at NIF”. In: *Phys. Rev. Lett.* 126 (2 Jan. 2021), p. 025001. DOI: 10.1103/PhysRevLett.126.025001. URL: https://link.aps.org/doi/10.1103/PhysRevLett.126.025001.